UNIVERSITY OF ROCHESTER
LABORATORY FOR LASER ENERGETICS

Volume 66
January–March 1996
DOE/SF/19460-125

LLE Review

Quarterly Report

UR
LLE

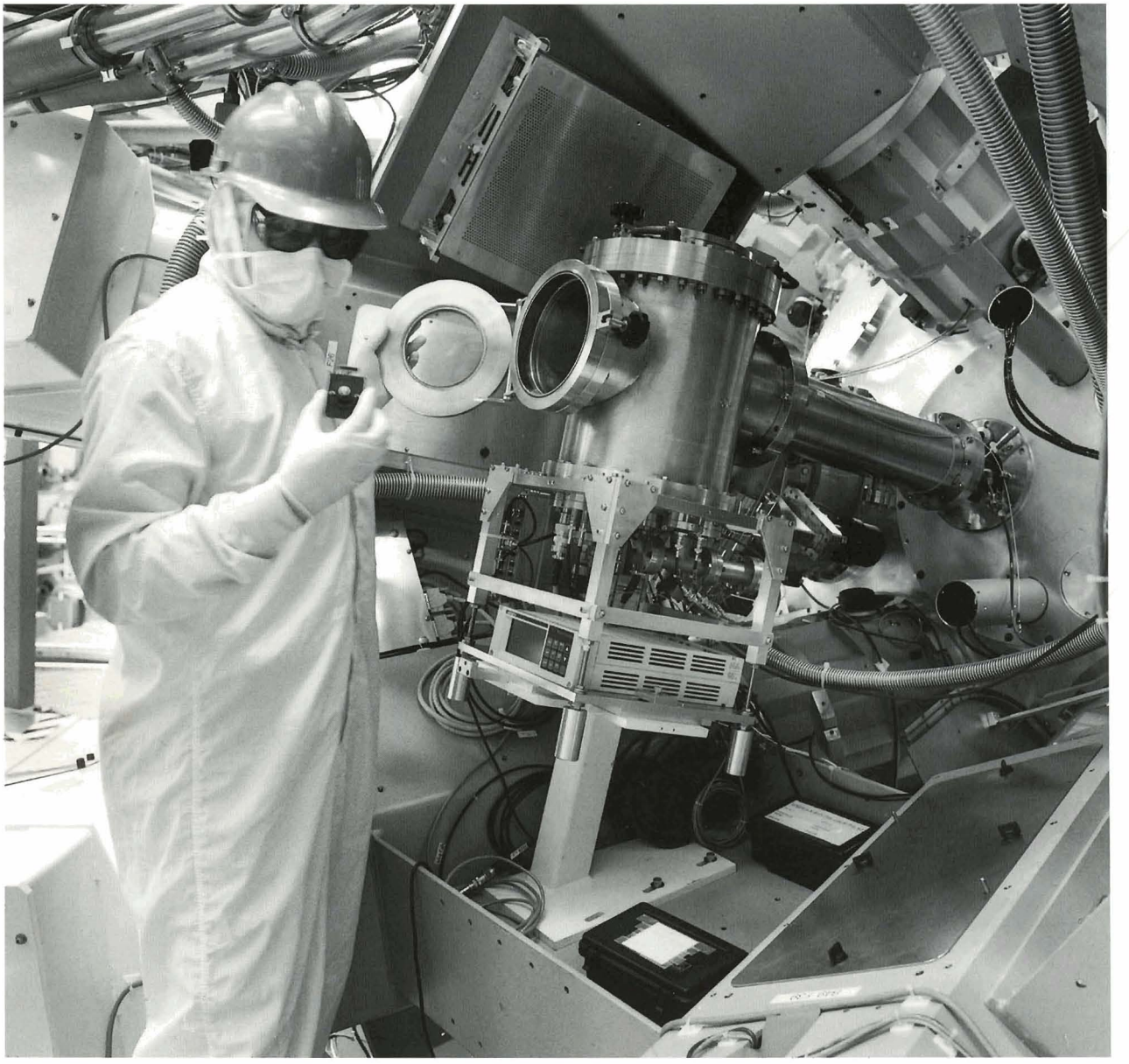

About the Cover:

Frederic Marshall, LLE scientist, prepares a film cartridge for the gated monochromatic x-ray microscope. This instrument, a joint development project of LLE and Los Alamos National Laboratory (LANL), can simultaneously space- , time- , and spectrally resolve x rays emitted by OMEGA targets.

The work described in this volume includes current research at the Laboratory for Laser Energetics, which is supported by New York State Energy Research and Development Authority, the University of Rochester, the U.S. Department of Energy Office of Inertial Confinement Fusion under Cooperative Agreement No. DE-FC03-92SF19460, and other agencies.

Printed in the United States of America
Available from
National Technical Information Services
U.S. Department of Commerce
5285 Port Royal Road
Springfield, VA 22161

Price codes: Printed Copy A04
Microfiche A01

For questions or comments, contact Thomas R. Boehly, *Editor*, Laboratory for Laser Energetics, 250 East River Road, Rochester, NY 14623-1299, (716) 275-0254.

UNIVERSITY OF ROCHESTER
LABORATORY FOR LASER ENERGETICS

Volume 66
January–March 1996
DOE/SF/19460-125

LLE Review

Quarterly Report

UR LLE

Contents

In Brief

This volume of the LLE Review, covering the period January–March 1996, contains three articles related to spherical implosions and their diagnosis, one article that provides an analysis of laser-plasma interactions, and three articles on advanced technologies developed at LLE.

Highlights of the research presented in this issue are

- Initial shell convergence measurements on 60-beam implosions using unsmoothed laser beams show a marked improvement over similar 24-beam experiments performed several years ago. These results augment the success of high-performance targets planned on OMEGA once uniformity enhancements are implemented.

- Scientists from LLE and LANL have worked together to develop a microscope that produces time-gated, monochromatic images with reasonably high resolution. Ideally suited for imaging ICF implosions, this device will find many applications on OMEGA experiments. One such experiment is discussed.

- Many ICF experiments use one- or two-dimensional x-ray imaging to infer the conditions of the imploded core. Central to this application is the Abel inversion, which enables the transformation of a line-of-sight measurement to the local emission or absorption features in the target. Several configurations are discussed for a canonical cryogenic experiment.

- When intense laser beams cross in the presence of a plasma, ion-acoustic waves can transfer energy between the beams. This problem, particularly critical for indirect drive, has been studied for several test cases. A two-dimensional analysis of beams with unequal frequency propagating through a homogeneous plasma is presented for both the transient and steady-state regimes.

- Optical replication is used for a variety of optical manufacturing applications, including the production of distributed phase plates for OMEGA. It is hoped that a photoresist with low surface energy will obviate the need for a release layer and greatly simplify the production of phase plates and other optical components. The first steps for development of such a resist are discussed.

- One of the primary criteria for judging a finishing technique is the surface quality it produces. This article correlates resultant surface microroughness to the mechanical properties of various glasses finished with deterministic microgrinding.

- Chiral nematic liquid crystal can be used in applications where the helical sense of the molecules produces the desired optical effect. This article discusses the vitrification of these crystals into cholesteric glasses as a way to preserve the mesogenic order, thereby producing robust components. Various methods to optimize optical performance of these components are also suggested.

Thomas R. Boehly
Editor

Initial Shell Convergence Measurements Using OMEGA's 60 Unsmoothed Beams

One metric commonly used to evaluate the performance of inertial confinement fusion (ICF) targets is the ratio of the measured neutron yield to that predicted by a one-dimensional hydrodynamic simulation. When plotted versus the calculated convergence ratio of the implosion, this ratio [referred to as the YOC (yield-over-clean)] provides an indication of the nonuniformity present in the implosion [when targets that experience Rayleigh-Taylor (RT) similar growth factors are compared]. The convergence ratio is defined as the ratio of the initial and the final radii of the fuel/pusher interface. A concern, however, is that early experimental results never produced discernible, limb-brightened, stagnated cores. An example of this is displayed in Fig. 66.1, where azimuthally averaged radial profiles of early OMEGA implosions (driven by 24 unsmoothed beams, circa 1986) are compared with results from our one-dimensional hydrodynamics code *LILAC*. [These profiles were produced from time-integrated images obtained with a Kirkpatrick-Baez (KB) microscope.] In four such implosion experiments, we found little agreement with the position and spatial extent of the stagnated shell as predicted by the simulations. All of the experimental results indicated a broad, center-peaked, and somewhat nebulous core, whereas the *LILAC* results predicted a well-defined stagnated shell. As a result, the YOC-convergence comparisons required the use of the calculated convergence ratios. Figure 66.2 shows a similar comparison for the 1986 data.

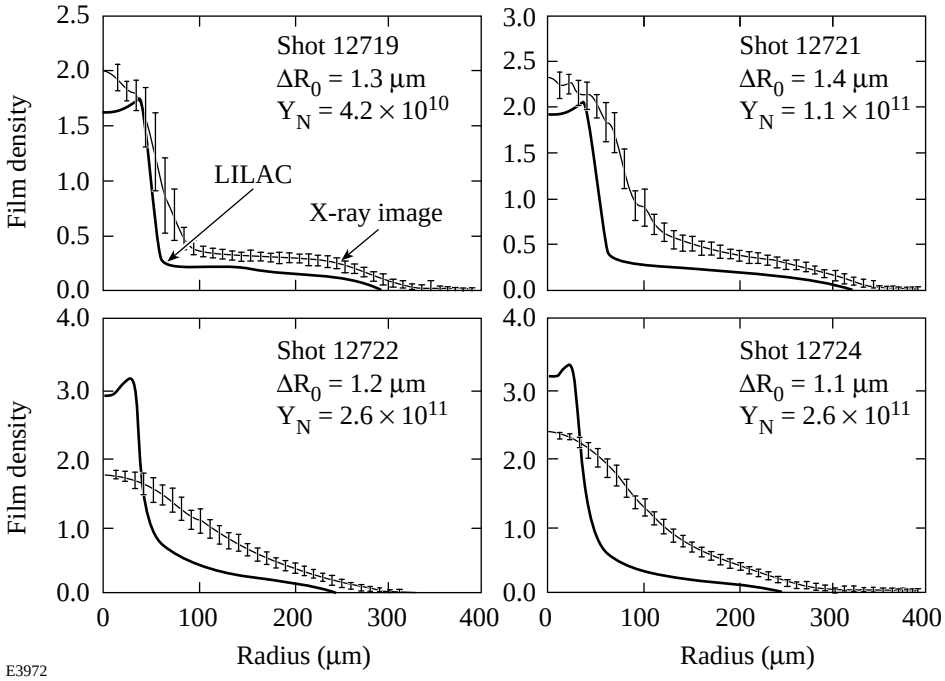

Figure 66.1
Azimuthally averaged radial profiles determined from time-integrated x-ray micrographs of early (circa 1986) target implosions. The *LILAC* simulations take into account the response of the microscopes and film. (These images were taken with KB microscope optics coated with nickel and hence were limited to $E \leq 4.5$ keV.)

Experiments using the 60 unsmoothed beams of the upgraded OMEGA laser system show a marked improvement in implosion symmetry as compared with similar, unsmoothed 24-beam experiments. Figure 66.3 shows four images of hard x-ray emission (>5 keV), viewed by a KB microscope, for high-yield targets taken on different 60-beam implosion experiments. The presence of a stagnated shell and/or a well-defined core is evident in each image. Particularly encouraging is the comparison of the azimuthally averaged radial intensity profiles of these images with the corresponding profiles predicted by *LILAC* (see Fig. 66.4). When compared to similar 24-beam results (from 1986), these data clearly indicate an

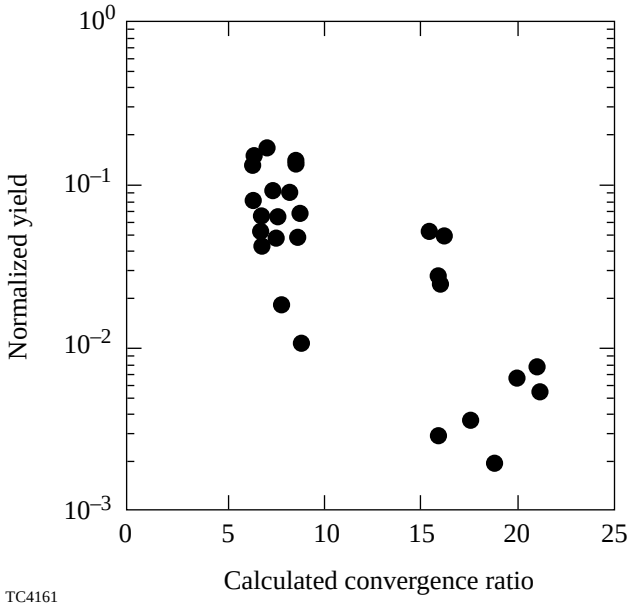

Figure 66.2
Normalized neutron yield (ratio of the experimentally measured neutron yield to the calculated neutron yield, commonly referred to as YOC (yield-over-clean)] versus the calculated convergence ratio (defined as the ratio of the initial to the final fuel/pusher radius). This data was taken in 1986.

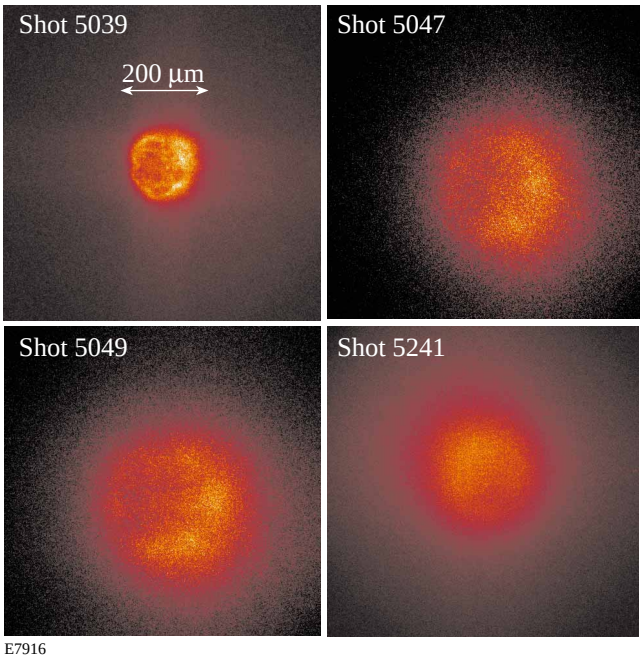

Figure 66.3
KB microscope images of high-yield implosions. These time-integrated images were taken with the latest Ir-coated optics and have an approximate sensitive energy band of 5 to 8 keV.)

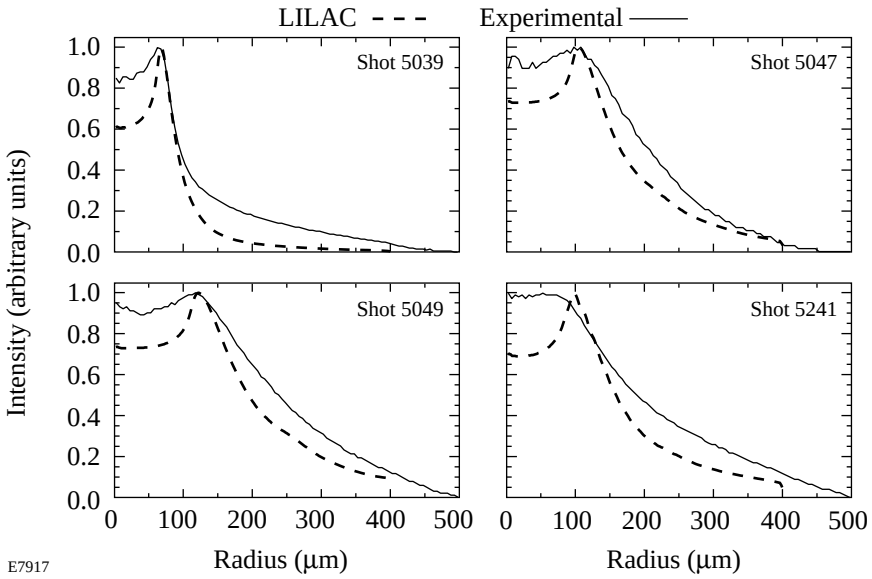

Figure 66.4
Azimuthally averaged radial intensity profiles determined from time-integrated x-ray micrographs of recent target implosions. The *LILAC* simulations take into account the response of the microscopes and film. The overall intensities have been normalized to the intensities at their peak.

improvement in the quality of the experimentally observed compressions due to 60-beam irradiation. While the exact position of the fuel/pusher interface remains clouded within the data (as a result of growing nonuniformities, mix layers, etc.), it may eventually be possible to measure the convergence ratio directly from the experiments.

The improved implosion performance is also demonstrated by the neutron yields as is evident from the YOC-convergence ratio comparison shown in Fig. 66.5. These data show that for implosions with similar convergence ratios, the 60-beam implosions perform significantly better than those driven by 24 beams. This improvement was accomplished with an increase in beam number and without irradiation uniformity schemes such as distributed phase plates (DPP's) or smoothing by spectral dispersion (SSD). Once these uniformity enhancements are implemented, the improvements in the implosion drive may allow experimentally observed convergence ratios to be used in our analysis.

ACKNOWLEDGMENT

This work was supported by the U.S. Department of Energy Office of Inertial Confinement Fusion under Cooperative Agreement No. DE-FC03-92SF19460, the University of Rochester, and the New York State Energy Research and Development Authority. The support of DOE does not constitute an endorsement by DOE of the views expressed in this article.

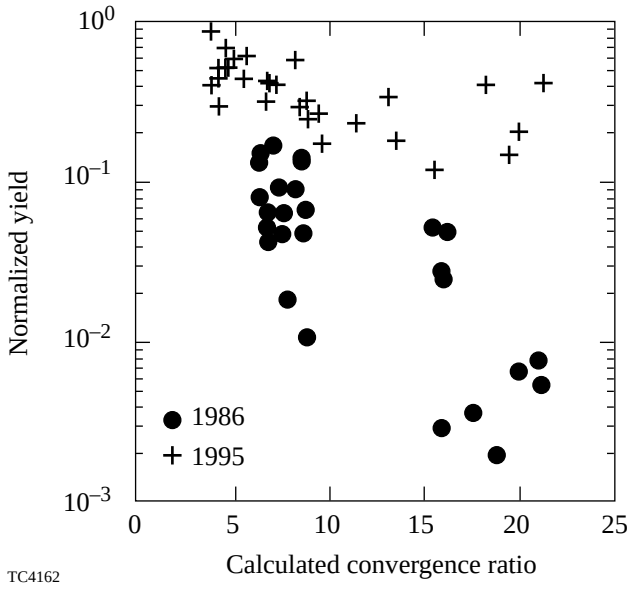

Figure 66.5
Comparison of YOC analyses for the yield data from 1986 to that for the yield measurements taken recently on OMEGA.

A Framed Monochromatic X-Ray Microscope for ICF

The Laser Fusion Experiments Groups from the Laboratory for Laser Energetics (LLE) and the Los Alamos National Laboratory (LANL) have jointly developed an instrument capable of simultaneously space-, time-, and spectrally resolving x-ray emission from inertial confinement fusion (ICF) targets. Uses of the instrument include framed imaging of line emission from fuel or shell dopants and monochromatic backlighting. The x-ray imaging is accomplished with a Kirkpatrick-Baez (KB)–type four-image microscope (developed at LLE). The microscope has a best spatial resolution of ~5 μm and a sensitive energy range of ~2 to 8 keV. Time-resolved x-ray images are obtained with a pair of custom framing cameras (developed at LANL), each of which records two of the four images in two independent 80-ps time intervals. In addition, the energy range of the images can be restricted to a narrow (monochromatic) spectral range (~10 to 100 eV) by the introduction of diffracting crystals. This technique has been demonstrated in LLE's x-ray laboratory with an *e*-beam-generated dc x-ray source, and at the LANL Trident laser facility with x rays from a laser-produced plasma. The microscope and gated monochromatic x-ray imaging (GMXI) module are undergoing initial testing on LLE's OMEGA laser fusion facility.

This instrument accomplishes monochromatic imaging by introducing diffracting crystals near the image plane of the microscope.[1] The arrangement is shown in Fig. 66.6. The microscope optic is a distance d from the source of x-ray emission (target). If a crystal is placed in front of the image plane at a mean angle of θ, the emission within a region Δx and at a wavelength λ will be diffracted, where $\Delta x = d \cdot \Delta\theta$ and $\Delta\theta$ is the rocking curve width of the diffracting crystal. The mean wavelength is given by the Bragg equation $n\lambda = 2d \sin\theta$, where n is the diffraction order and d is the crystal plane spacing. The combination of KB-optic distance (~200 mm) and mosaic crystal rocking-curve width (~0.2°) makes this technique applicable to laser-fusion plasmas (since in this case Δx ~ 700 μm). The range of energies in the diffracted image is $\Delta E = E \cot\theta \cdot \Delta\theta$. An additional consequence of using the diffracting crystal is a degradation in image quality. This is quantified by considering rays in the microscope near the image plane. The crystal acts as a reradiator, taking an input ray and diffracting it into a spread of angles $\Delta\theta$ that result in a spread of positions $\Delta x'$ at the image plane. Scaling this to the target plane ($\Delta x = \Delta x'/M$, where M is the magnification) and noting that $\Delta x' = \Delta z \cdot \Delta\theta$, where Δz is the separation between the crystal and the detector, gives an image smearing of $\Delta s = \Delta z \cdot \Delta\theta / M$. This quantity can be minimized for a given $\Delta\theta$ by working at large magnification and by working at small crystal-image plane separations (hence the choice of crystal location). An example of resultant smearing for $\Delta\theta \sim 0.2$, $\Delta z =$ 2 cm, and $M = 13.6$ (appropriate to the current design) is $\Delta s \sim$ 5 μm, which is of the order of the best resolution of the KB optics.[1] The arrangement of framing cameras and crystal monochromators that has been adopted for the GMXI is shown in Fig. 66.7.

In order to effectively use this technique to obtain gated monochromatic x-ray images of laser-fusion targets, the microscope, monochromator, and framing cameras have been

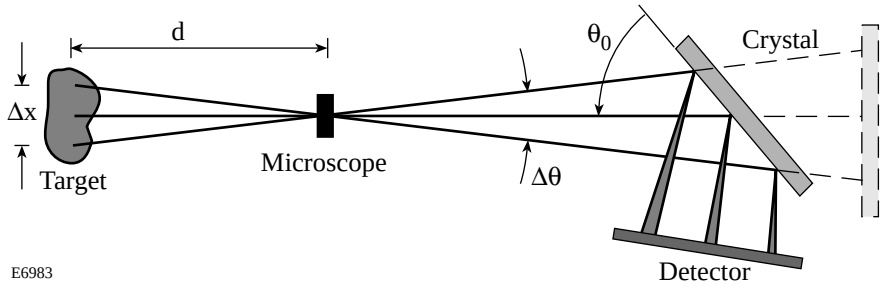

Figure 66.6
Schematic of the technique used to obtain monochromatic x-ray images with a KB microscope.

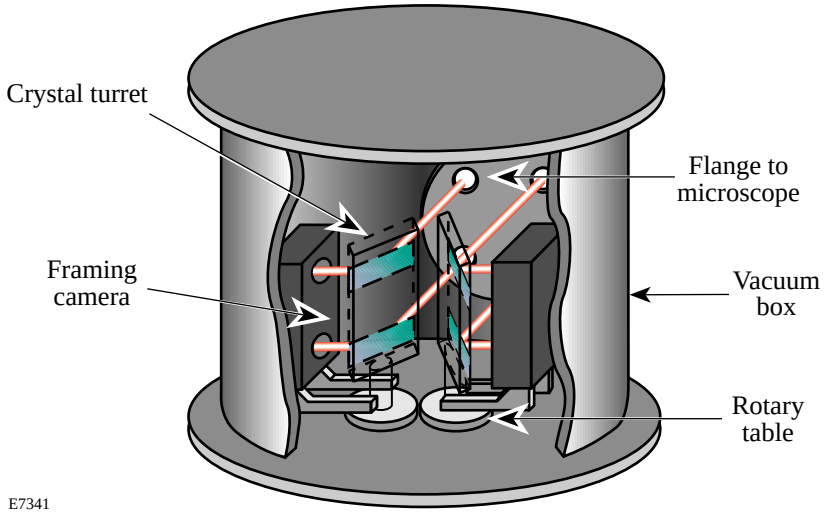

Figure 66.7
The GMXI module consists of two rotary stages, each of which positions a crystal turret-framing module pair. The crystal turrets, each containing two crystals, are positioned at the desired Bragg angle θ_B, while the framing modules are positioned at the diffracted image plane.

individually calibrated and then tested as an integrated system. Figure 66.8 shows the measured resolution of the microscope versus distance from best focus for an individual image. The resolution is seen to approach the ideal resolution calculated by ray tracing. The microscope reflectivity was measured also with a dc x-ray source using the method described in Dhez *et al.*[2] Both the Au-coated and Ir-coated optics have been characterized (Fig. 66.9). Both coatings were produced by ion-assisted deposition and final substrate roughness measured to be ≲4 to 5 Å rms.[3] Figure 66.9(a) shows that the reflectivity of the Au-coated mirrors is in close agreement to that calculated from tabulated values of the atomic scattering factors. The current Ir-coated mirrors show a falloff compared to ideal reflectivity at high energies [Fig. 66.9(b)] (likely due to an underdense coating).[4] Nevertheless, the current Ir-coated mirrors perform as well as the Au-coated mirrors.

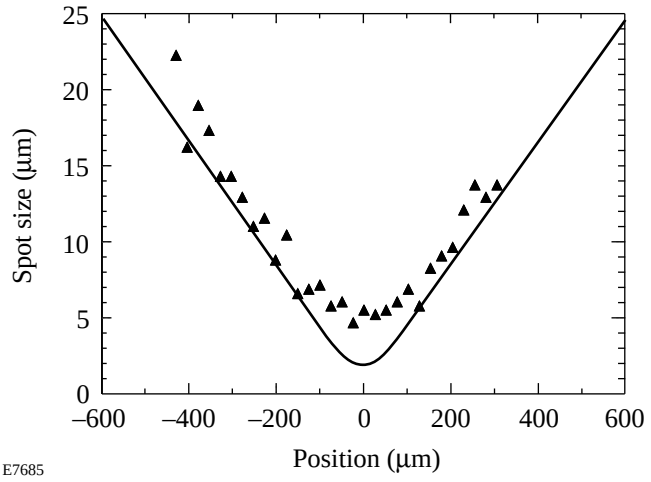

Figure 66.8
Results of resolution measurements of the KB microscope mirror assembly. The spot size (full width) versus position from best focus was determined from a backlit image of a Cu-mesh using a dc x-ray source. The solid line is the predicted spot size determined from ray tracing.[1]

Monochromatic imaging with a KB microscope was first demonstrated in the laboratory with a dc x-ray source. Figure 66.10 shows the spectrum of the *e*-beam-generated x-ray source (Ti target) as obtained with a Si(Li) detector. The source was backlighting a grid placed at the focal plane of the KB microscope. A LiF crystal (200 plane, $2d$ = 4.027 Å) was placed 2 cm before the image plane and set to the nominal Bragg angle θ_B for Ti Kα (2.75 Å = 4.51 keV, θ_B = 43.07°). The diffracted spectrum consisting of the single Ti Kα line is also shown in Fig. 66.10. The diffraction peak was then scanned about this nominal central angle in order to verify the accuracy of angular alignment. Once the angle of peak reflectivity was found, a film pack was placed in front of the Si(Li) detector at the image plane. Figure 66.11 shows the results of these experiments. Monochromatic images were taken of Ti Kα emission with a LiF crystal and with a highly oriented pyrolytic graphite (HOPG) crystal ($2d$ = 6.708 Å, θ_B = 24.20°). As expected, some image degradation resulted. Nevertheless, good quality images were obtained with both crystals.

In a separate set of measurements with the same x-ray source, the diffraction response of LiF and HOPG (rocking curves) was measured by impinging a narrow beam ($\Delta\theta$ < 0.01°) on the crystal. Figure 66.12 shows reflectivity curves for

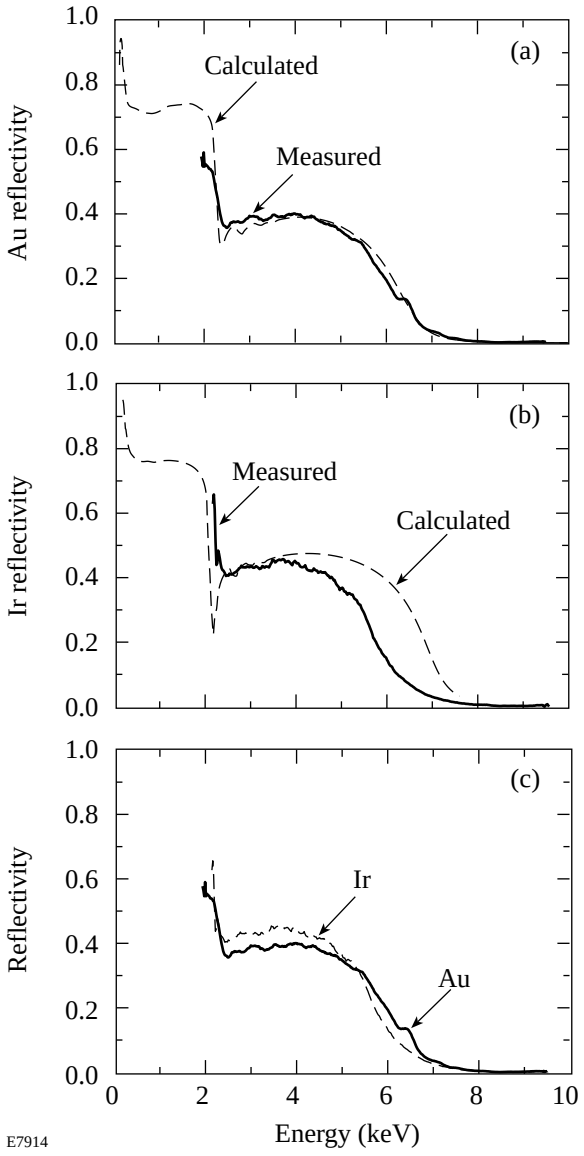

Figure 66.9
X-ray reflectivity measurements of Au- and Ir-coated KB microscope optics.

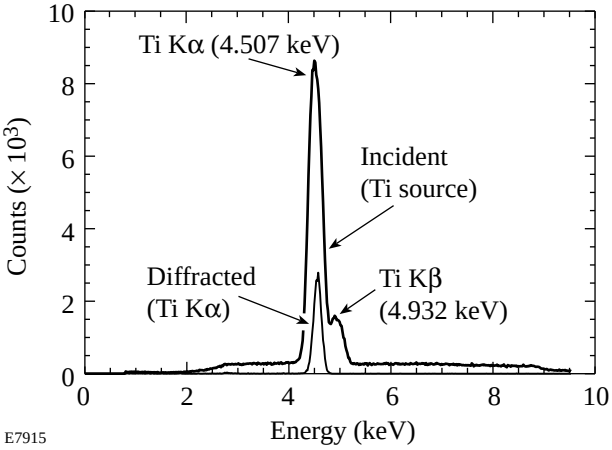

Figure 66.10
The *e*-beam-generated x-ray source and KB-microscope-imaged, diffracted x-ray spectra. Only the Ti Kα line is diffracted by the LiF crystal.

LiF and HOPG both at the Ti Kα line energy. The full-width at half-maximum (FWHM) and peak reflectivities R_p were found to be FWHM = 0.20°, R_p = 0.14 for LiF, and FWHM = 0.55°, R_p = 0.28 for HOPG. The narrower angular response of the LiF crystal yields a higher resultant resolution (~8 μm) but can be seen to limit the field of view (~700 μm) in the plane of crystal diffraction (horizontal axis). Conversely, the HOPG crystal yields a lower spatial resolution (~12 μm) but benefits from a larger field of view (~1400 μm). Both of these tests were performed at an image magnification of 9.3, and the resultant image smearing could be further reduced by operating at higher magnification.

Monochromatic imaging of a laser plasma with a KB microscope was first demonstrated at the LANL Trident laser facility. A Cu mesh was backlit by a Ti disk irradiated by ~150 J of 532-nm light in a 1.2-ns (FWHM) pulse. Figure 66.13 shows the results of these experiments—both broadband [Fig. 66.13(a)] and monochromatic [Fig. 66.13(b)] images were obtained. The monochromatic image is of the

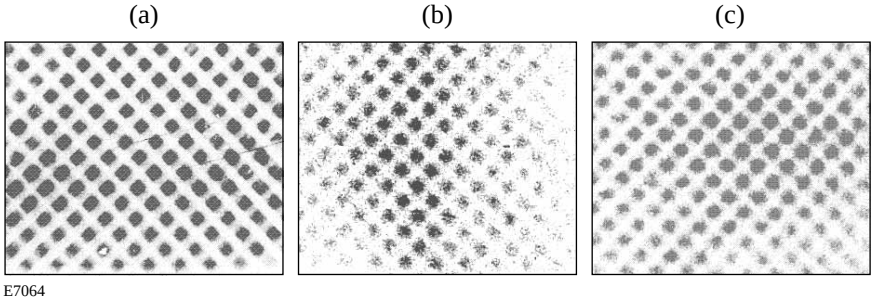

Figure 66.11
Broadband and monochromatic images of backlit grids obtained with a KB microscope and an *e*-beam-generated Ti x-ray source: (a) broadband and monochromatic images of Ti Kα emission taken with a (b) LiF crystal, and (c) HOPG crystal.

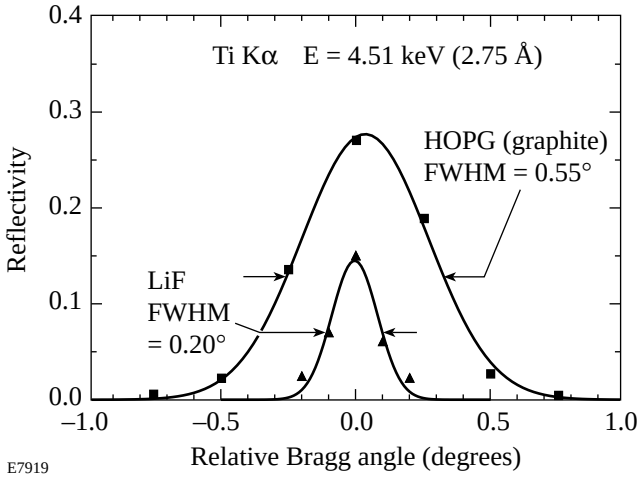

Figure 66.12
Rocking curves for HOPG and LiF at 4.51 keV = 2.75 Å.

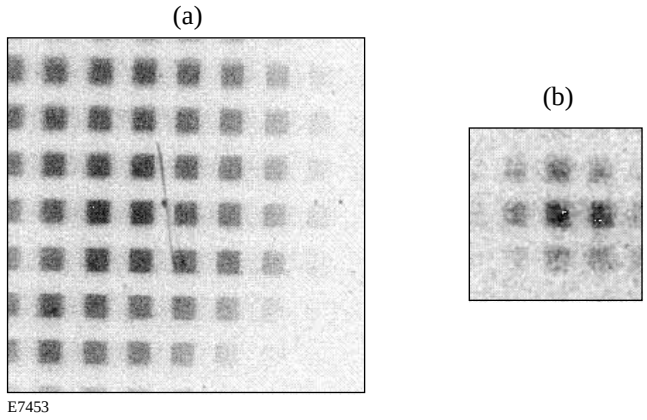

Figure 66.13
KB microscope images of 25-μm wire meshes backlit by Ti disks acquired at the LANL Trident laser facility: (a) broadband (2 to 7 keV), (b) monochromatic [4.75 keV (2.61 Å)].

Ti He-like Ly α line taken with a LiF crystal (2.610 Å = 4.750 keV, $\theta_B = 40.41°$). (In this experiment the magnification was 12.9 and the crystal-image plane separation was 2 cm.) Good resolution was obtained (~10 μm) despite some misalignment of the KB microscope from its optimum focusing position.

Framed images are obtained with a pair of custom modules (developed at LANL), consisting of a pair of 25-mm-diam microchannel plates (MCP's) with proximity-focused fiber-optic faceplates coated with P11 phosphor (Fig. 66.14). Light from the phosphor is recorded by Kodak TMAX film loaded into film packs that press the film against the fiber-optic faceplate. Details of the electronics are described by Oertel *et al.*[5] The current modules have a sensitive frame time of ~80 ps, and the frames on each module are separated by 350 ps (53-mm spatial separation). Each module can be independently gated, providing for flexibility in the type of measurements obtained.

The monochromators consist of a combined crystal turret and detector turret. A geared mechanism drives the detector turret at twice the angle of the crystal turret. A pair of stepper-motor-driven rotary stages drive the turret assemblies. Each turret assembly can be set at a separate angle, allowing two wavelengths to be imaged if desired. The rotary stage angles were calibrated at the Ti Kα energy with both LiF and HOPG crystals by placing a proportional counter at the position of the framing modules on the detector turret. The positions were referenced to the rotary-stage position encoders to an accuracy of 0.01°. The current rotary-stage assemblies can be set to diffraction angles of up to $\theta_B \sim 65°$. The requirement that the diffracted image be away from the direct line of site places a practical lower limit of $\theta_B \sim 15°$. The resulting wavelength range that can be accessed by the GMXI is 1.74 to 6.08 Å (2.04 to 7.12 keV) for HOPG and 1.04 to 3.65 Å (3.40 to

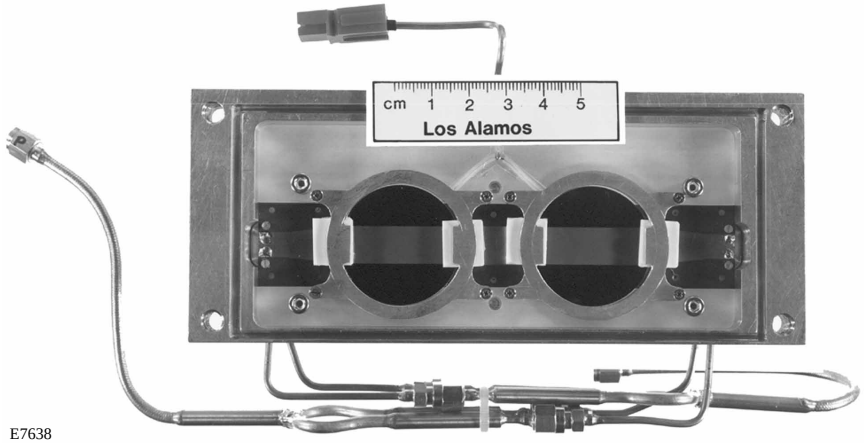

Figure 66.14
The LANL framing camera modules that are used in the GMXI.

11.92 keV) for LiF. [The practical upper limit is further restricted by the mirror reflectivity to ~7 keV (1.8 Å).] These two crystal types are seen to be appropriate to the energy range of the microscope (~2 to 8 keV). The energy band of the diffracted images depends on the crystal angle and type. The LiF crystal provides a narrow band that varies from ~15 eV at 3.4 keV to ~50 eV at 7 keV. The HOPG crystals yield a band of ~10 eV at 2 keV to ~250 eV at 7 keV. Elements whose principal emission lines fall in this range include Si, P, S, Cl, Ar, K, Ca, Sc, Ti, V, Cr, Mn, and Fe.

Figure 66.15 shows a schematic of the KB microscope and GMXI attachment as deployed on OMEGA. A pedestal supports the GMXI assembly. Fine adjustment of the KB microscope pointing is accomplished by raising or lowering the adjustable support legs and by right or left adjusting screws. A referenced pointing adjustment system is built into the microscope and consists of a flexible weldment re-entrant into the OMEGA target chamber, combined with a pair of micrometers that measure the flight tube position. Initial alignment is accomplished by placing a pointer on the end of the microscope's optic blast-shield cover. The pointer is aligned to the target chamber center (TCC) by positioning the GMXI assembly and by a fine adjustment on the optic distance. Film packs containing Kodak DEF were placed at the image plane with the crystal turret removed. After the first image was obtained, final alignment was accomplished by adjusting the GMXI module using the micrometer readings as a reference.

First results of the GMXI were obtained on OMEGA target experiments investigating burnthrough and mix. (Details of this type of experiment are given in Ref. 6.) The targets consisted of DD-filled CH shells with overcoated layers of chlorinated and unchlorinated parylene. Figure 66.16 shows the resultant time-integrated images obtained with an adjoining KB microscope on shot 6483. The broadband time-integrated image shows shell emission plus a bright core, which may contain chlorine ion line emission. Figure 66.17 shows the GMXI results. Framed images were obtained with one module set to look at broadband emission (no crystal monochromator) [Figs. 66.17(a) and 66.17(b)], while a time-integrated monochromatic image was obtained by placing a DEF film pack on the detector turret with an HOPG crystal set to diffract Cl-He–like Ly α emission (4.44 Å = 2.79 keV, θ_B = 41.44°) [Fig. 66.17(c)]. The framed images reveal a target shell early in the implosion [Fig. 66.17(a)] and 350 ps later [Fig. 66.17(b)], at a time near peak compression. The image of the target core in Fig. 66.17(b) is nearly saturated, obscuring fine details of the emission. Conversely, the narrow energy band of the monochromatic image [Fig. 66.17(c)] has further limited the flux to

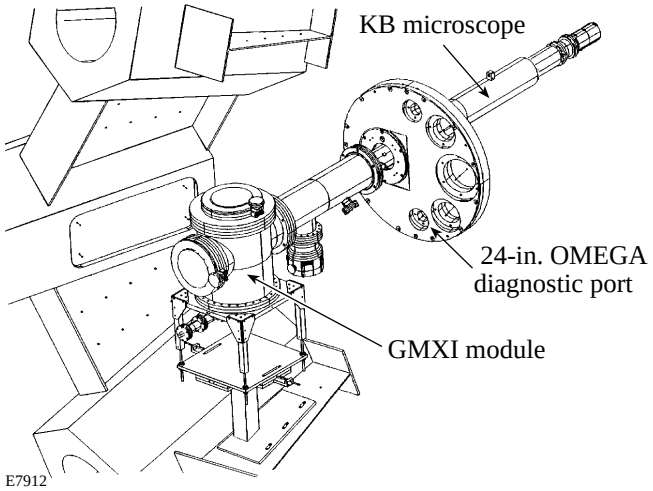

Figure 66.15
Perspective view of the gated monochromatic x-ray microscope (GMXI) as it is deployed on OMEGA.

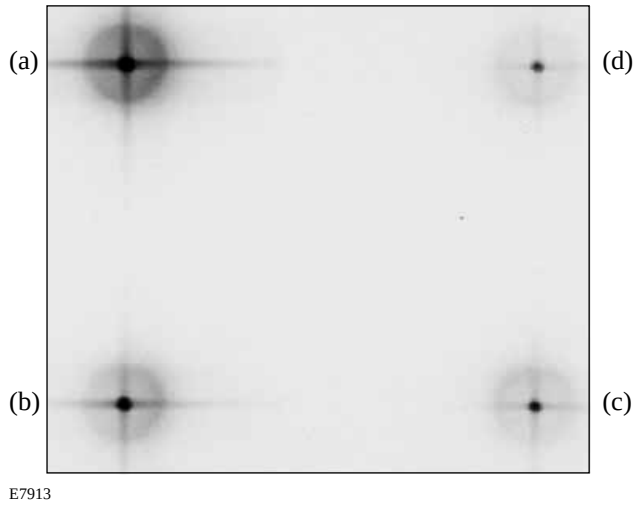

Figure 66.16
Four images obtained with a nearly duplicate KB microscope on OMEGA shot 6483. This microscope viewed the target plane from a nearby direction (~30° away). The four different images are filtered to give a range of exposures. The effective energy bands are (a) 4 to 8 keV, (b) 4.5 to 8 keV, (c) 5 to 8 keV, and (d) 5.5 to 8 keV.

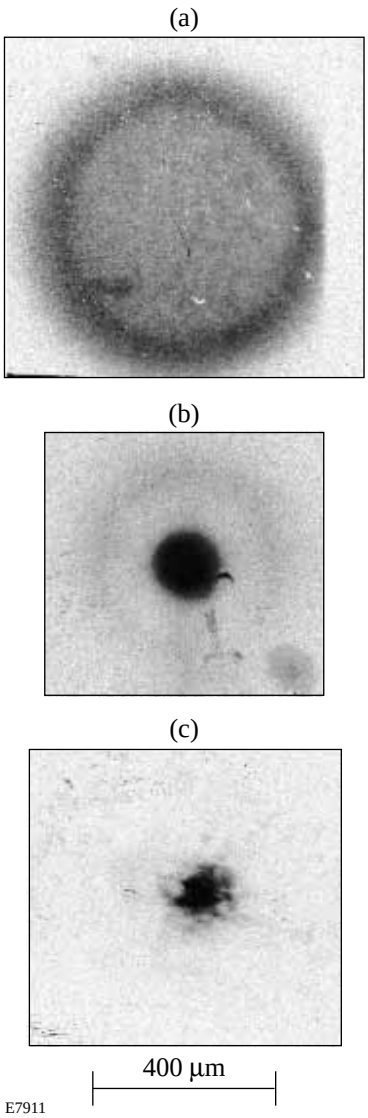

Figure 66.17
Images obtained with the GMXI of an imploding target on OMEGA shot 6483. Framed images were obtained with one module set for broadband imaging (a,b), while a time-integrated monochromatic image of 4.45-Å Cl emission was obtained with an HOPG crystal and a film pack (c). All images have the same scale (indicated by the 400-μm bar).

a level where an unsaturated image was obtained. The calculated energy band of the image ($\Delta E = E \cot\theta \cdot \Delta\theta$) is ~30 eV. The strength of the emission, its size, and location make it unquestionably Cl (He-α). The presence and amount of Cl emission in the core can serve as a diagnostic of mixing.[7]

In conclusion, we have deployed a new diagnostic on the OMEGA target chamber. It is capable of simultaneously space-, time-, and spectrally resolving x-ray emission from laser targets. The project is a collaborative effort between the University of Rochester's Laboratory for Laser Energetics and the Los Alamos National Laboratory. This imaging system will be important in diagnosing shell and core size, density, and mixing in ICF experiments conducted on the OMEGA laser system.

ACKNOWLEDGMENT

The authors acknowledge the support of the staffs at LLE and LANL, and the operations staffs at the LANL Trident laser facility and the LLE OMEGA laser facility. This work was supported by the U.S. Department of Energy Office of Inertial Confinement Fusion under Cooperative Agreement No. DE-FC03-92SF19460, the University of Rochester, and the New York State Energy Research and Development Authority. The support of DOE does not constitute an endorsement by DOE of the views expressed in this article.

REFERENCES

1. F. J. Marshall and Q. Su, Rev. Sci. Instrum. **66**, 725 (1995).
2. P. Dhez, H. Duval, and J. C. MacLaurent, J. X-Ray Sci. Technol. **3**, 176 (1992).
3. D. Smith, LLE (private communication).
4. R. F. Elsner, S. L. O'Dell, and M. C. Weisskopf, J. X-Ray Sci. Technol. **3**, 35 (1991).
5. J. A. Oertel, T. Archuleta, L. Clark, S. Evans, A. Hauer, C. G. Peterson, T. Sedillo, C. Thorn, R. G. Watt, and F. J. Marshall, in *Ultrahigh- and High-Speed Photography, Videography, and Photonics '95,* edited by D. R. Snyder and G. A. Kyrala (SPIE, Bellingham, WA, 1995), Vol. 2549, p. 82.
6. Laboratory for Laser Energetics LLE Review **64**, NITS document No. DOE/SF/19460-99, 1995 (unpublished), p. 160.
7. B. Yaakobi, F. J. Marshall, Q. Su, and R. Epstein, J. X-Ray Sci. Technol. **5**, 73 (1995).

Abel Inversion of Emission and Backlighting Images

The Abel inversion is used to calculate local plasma quantities (in three dimensions) from line-of-sight measurements. Two examples relevant to laser-driven implosion experiments are the imaging of x-ray radiation where (a) the Abel inversion of emission images yields the local emission, and (b) the Abel inversion of backlit images yields the local density. As explained below, the imaging in the first case can be either two-dimensional or one-dimensional, but in the second case it must be two-dimensional. For x-ray emission, the Abel inversion procedure can be complicated by self-absorption within the emitting volume (in addition to attenuation by the surrounding shell). However, in the case of backlighting images, the problem is simpler because absorption occurs mostly in the colder parts of the compressed target, where emission can be negligibly small. In the case of imploding cryogenic targets, the situation is further simplified because (a) the compressed core consists of only hydrogenic ions, and (b) the absorbing layer is spatially separate from a central emitting hot spot. We therefore choose cryogenic implosions to demonstrate the utility of the Abel-inversion procedure applied to both two-dimensional and one-dimensional x-ray images. We use target profiles calculated by *LILAC* to simulate experimental images by applying a simplified radiation transport model, then analyze them through the Abel inversion and compare the results to the original target parameters.

Monochromatic images are required for the analysis presented here because of the wavelength dependence of the employed parameters (opacity and continuum emission). Additionally, in the case of backlighting, monochromatic images help discriminate the backlighting image against the target self-emission.[1,2] Two-dimensional monochromatic images can be achieved with an x-ray microscope fitted with a diffracting crystal between the optics and the image plane—a method recently developed at LLE by F. J. Marshall. Spatial resolution in the 8- to 12-μm range has been experimentally demonstrated.[3] One-dimensional polychromatic imaging can be obtained with a crystal spectrograph equipped with a resolving slit. We will assume that a spatial resolution of 10-μm FWHM can be achieved in either case.

The intensity emitted by the target is a line integral of the local emission and can therefore be Abel-inverted. In the case of backlighting, it is the opacity, rather than the measured intensity, that can be Abel-inverted. In two-dimensional imaging of a backlit target, each image point yields the opacity along the corresponding line of sight, and the opacity image can thus be Abel-inverted to yield the local density. However, when using a slit for one-dimensional imaging of a backlit target, the unique opacity of individual rays is lost. On the other hand, when measuring target self-emission, either a one-dimensional or a two-dimensional image can be Abel-inverted to yield the local emission. In fact, the two-dimensional Abel-inversion procedure described in the next section transforms the image to a one-dimensional image as would be seen by a slit. In this case the advantage of starting with a two-dimensional image is the ability to judge the symmetry and uniformity, whereas the advantage of using a spectrograph-slit combination is the ability to record a polychromatic image over a wide spectral range.

Abel Inversion

In the past, the problem of Abel inversion was studied mainly for a cylindrical geometry, where the data form a one-dimensional array perpendicular to the axis. For a spherical geometry, where the data form a two-dimensional array, the situation is different and merits some consideration. Figure 66.18 shows the geometry of the problem. In the case of a cylindrical source with its axis along the z axis, the observation is along the x direction and the measurements form a one-dimensional array along the y axis. The local parameter in terms of its line-of-sight integral is given by[4]

$$\varepsilon(R) = -(1/\pi)\int_{R}^{R_0} \left\{ \left[dF(y)/dy \right] \Big/ \left[y^2 - R^2 \right]^{1/2} \right\} dy, \qquad (1)$$

where R_0 is the radius of the cylinder, $\varepsilon(R)$ is the local quantity, and $F(y)$ is the measured integral of the same quantity along the line of sight. In spherical geometry, two-dimensional imaging forms an array in the y-z plane. Normally, only the results for

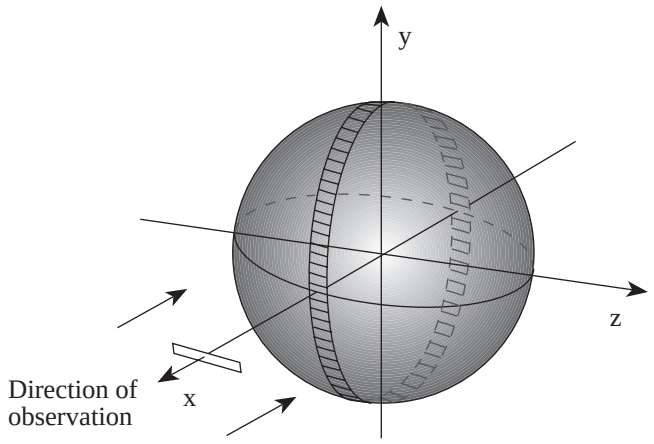

Figure 66.18
Geometry of the Abel inversion for backlighting a spherical source. Either two-dimensional monochromatic imaging (microscope-crystal combination) or one-dimensional polychromatic imaging (crystal-slit combination) can be used. To Abel-invert a two-dimensional image, the cylindrical solution can be applied to the coin-shaped element shown in the figure. Instead, the image can be integrated along the *z* axis and the solution for a spherical source viewed through a slit can be used.

$y = 0$ (or $z = 0$) are used, to which the cylindrical solution is applied.[5] To use the cylindrical solution while taking advantage of the entire two-dimensional data, we could average over the azimuthal angle (around the *x* axis), thereby converting the data into a one-dimensional array, and then use the cylindrical solution. Instead, we can integrate the data along, say, the *z* dimension. The solution of the Abel problem for the resulting one-dimensional array is the same as that for the case of imaging a sphere through a slit (in the *z* direction), namely[6]

$$\varepsilon(R) = (1/2\pi R)\left[dF(y)/dy\right]_{y=R}. \qquad (2)$$

The solution given by Eq. (2) is simpler than that given by Eq. (1) since it avoids the singularity at the lower bound of the integral (except at $R = 0$). In the case of imaged target emission, the numerical procedure described here is equivalent to using a one-dimensional imaging device, namely, an x-ray spectrograph with a slit for spatial resolution.

The Analyzed Test Case

A particular test case of a cryogenic target is studied using *LILAC* profiles and a radiation transport model (described in an earlier publication)[1] to simulate the two-dimensional backlighting image (including self-emission). The chosen pulse shape is typical of those to be used in high-performance implosions: its total duration is 9 ns; it rises slowly, then more rapidly, until reaching a plateau of 23 TW from 8 to 9 ns, then drops to zero. The total pulse energy is 30 kJ. The target is a 1060-μm-diam, 7.4-μm-thick CH shell containing a 90-μm-thick, cryogenic DT layer. Figure 66.19 shows the *LILAC* predictions for the temperature and density profiles at peak compression of this target (the electron and ion temperatures are nearly the same). Note the central hot spot surrounded by a cold and dense peripheral fuel region. By this time of the compression, the polymer shell and part of the fuel have been ablated away.

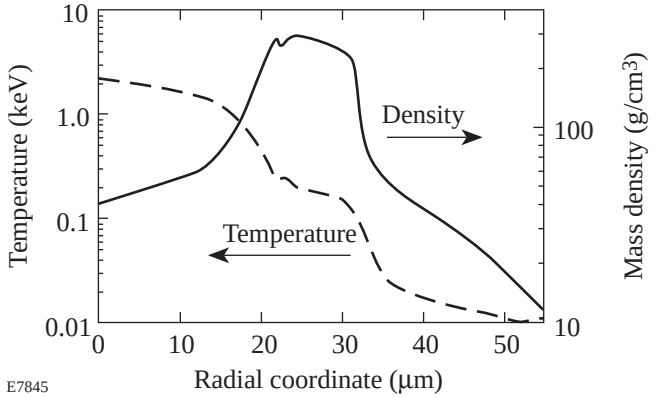

Figure 66.19
LILAC-computed temperature and density profiles of the cryogenic test implosion at peak compression.

Figure 66.20 shows a lineout through a two-dimensional image produced by backlighting and self-emission, at peak compression of the test target. The image is calculated assuming monochromatic detection of the $1s2p$–$1s^2$ line from a titanium backlighter ($\lambda = 2.62$ Å), using a diffracting crystal with a 4-eV bandpass. The curves are normalized to a spectral intensity of 7.0×10^{20} keV/(keV ns cm^2 Ω). This is the estimated intensity from a titanium backlighting target irradiated at 1.4×10^{15} W/cm^2 by a single OMEGA beam. The image in Fig. 66.20 can be divided into two sections: for radial distances greater than ~25 μm, the image is almost exclusively due to the backlighter; for radial distances less than ~25 μm, the image is almost exclusively due to self-emission. We treat Fig. 66.20 as a simulated experimental result and apply the same procedure as would be applied to an experimentally obtained image.

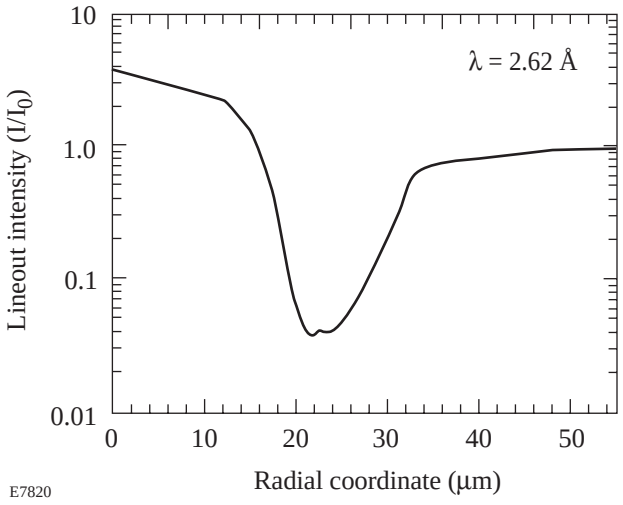

Figure 66.20
Lineout through the two-dimensional image due to backlighting and self-emission at peak compression of an imploded CH shell with cryogenic fuel. The image is calculated assuming monochromatic detection of the $1s2p$-$1s^2$ line of a titanium backlighter target ($\lambda = 2.62$ Å). The curves are normalized to a spectral intensity of 7.0×10^{20} keV/(keV ns cm^2 Ω).

Backlighting Image Analysis

The intensity $I(r)$ of the outer part of the image ($r > 25$ μm), where self-emission is negligible, directly yields the opacity along the line of sight, $\tau(r)$. Note that r stands for the radial coordinate in the two-dimensional image, as opposed to R, the radial coordinate in the three-dimensional target. The opacity is given by the relation $\tau(r) = \ln\left[I_0 / I(r)\right]$, where I_0 is the incident intensity of the backlighter. I_0 can be found from the intensity at larger radii where the backlighting radiation is essentially unattenuated, or from a separate laser shot where only the backlighter is irradiated. In a deuterium-tritium mixture, the absorption of x rays is due to inverse bremsstrahlung, and the opacity is given by[7]

$$\tau(r) = 2.334 \times 10^{-4}\left(\lambda^3 / T_c^{1/2}\right)\int_{x_2}^{x_1} \rho^2(r)\, dx, \qquad (3)$$

where λ is the wavelength in Å, T_c is the temperature in keV, ρ is the density in g/cm^3, and the integral is along the line of sight in the x direction: $x_1 = \left(R_0^2 - z^2 - y^2\right)^{1/2}$, $x_2 = -x_1$. By choosing a value for T_c, the electron temperature in the cold, absorbing fuel, Eq. (3) yields a two-dimensional array of the quantity ρ^2. We then integrate the array along the z axis and Abel-invert the results using Eq. (2). Figure 66.21 shows the density profiles obtained for three assumed temperatures of the absorbing region, compared to the original *LILAC* density profile used to obtain the image. As expected, the points for T_c = 0.2 keV agree with the *LILAC* curve in the region where the temperature is actually around 0.2 keV, and likewise for the other temperatures. Higher assumed temperatures result in higher densities because of the temperature and density dependencies in Eq. (3).

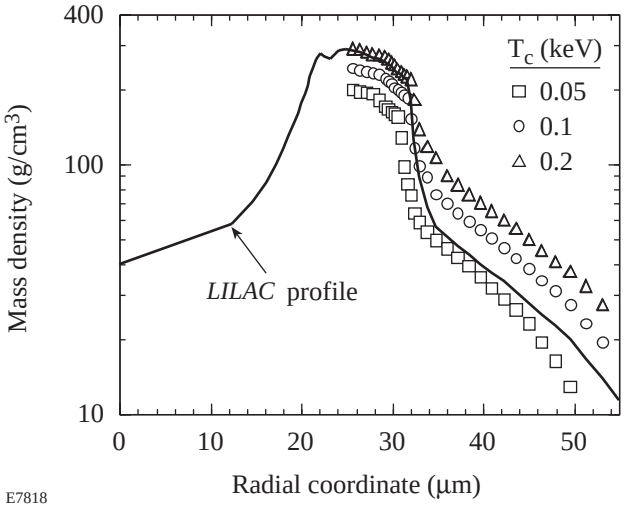

Figure 66.21
Abel-inverting the backlighting image of a cryogenic target (Fig. 66.20) yields the density distribution within the cold part of the compressed fuel for various assumed temperatures of the cold shell. The results are compared with the original *LILAC* density distribution (from Fig. 66.19) used in the simulation of the image.

Next, we convolve the image of Fig. 66.20 with the response function of the imaging device, which is assumed to be a Gaussian curve with FWHM of 10 μm. The Abel inversion was repeated, producing the results shown in Fig. 66.22. This analysis underestimates the peak density because the instrumental broadening reduces the depth of absorption in the backlighting image. Nevertheless, if the temperature is indeed between ~50 to 200 eV, the density profile in the cold region can be determined with an uncertainty of about a factor of 1.5. The effect of noise in the data will be discussed later.

The density determination can be extended to radii smaller than 25 μm if the self-emission component is subtracted from the image of Fig. 66.20. Since it is assumed that the backlighter emission is spectrally narrow, a slight wavelength detuning on the detector will create an image consisting of mostly the self-emission at a nearby wavelength, where the backlighter emission

is significantly reduced. In the case of 2-D imaging with a microscope-crystal combination,[3] this detuning can be achieved with an auxiliary crystal slightly off the Bragg angle.

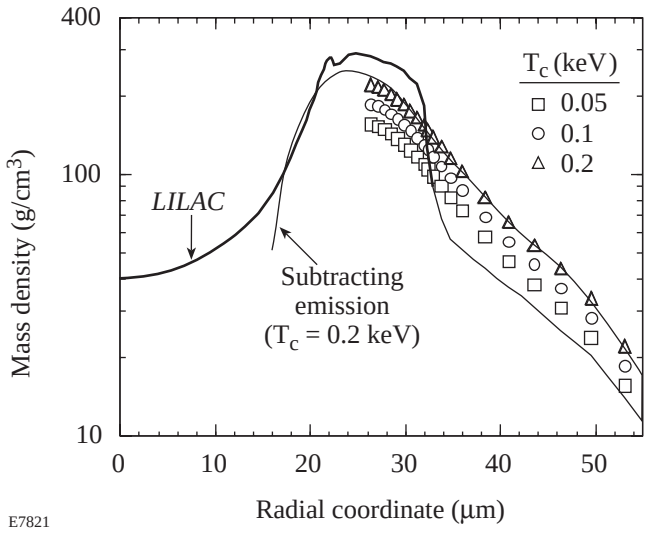

Figure 66.22
Same as Fig. 66.21, when the image of Fig. 66.20 is first convolved with an instrumental resolution curve of 10-μm FWHM and then Abel inverted. The thin curve, explained below, was obtained by Abel-inverting the image of Fig. 66.20, from which the self-emission contribution was first subtracted (the case $T = 0.2$ keV was assumed).

Using the radiation transport model,[1] the target emission image, at the backlighter wavelength (2.62 Å), was calculated and subtracted from the total image in Fig. 66.20, after each was convolved with a Gaussian instrumental profile of 10-μm FWHM. Finally, the Abel procedure was applied to the net backlighting image for the case of $T_c = 0.2$ keV. The result is shown by the thin curve in Fig. 66.22. Similar curves were obtained for other temperatures. It should be noted that most of the absorption occurs in the cold peripheral region, and it is the temperature of that region that is relevant. This is true even for the rays that traverse the target center. The thin curve in Fig. 66.22 does not extend all the way to the target center because of large errors in the Abel procedure at small radii. For an actual experiment, the procedure for extending the density curve would not be practical unless the relative emission intensity is lower than in the case shown in Fig. 66.20. This is because of the errors incurred in the subtraction of two comparable quantities (the total image and the self-emission component). A lower relative intensity of the target emission can arise from ineffective target compression or higher backlighting intensity.

Self-Emission Image Analysis

Information on the temperature in the central hot-spot region can be obtained from an Abel inversion of the emission profiles. To that end, images at a wide range of wavelengths are necessary. Such images can be readily obtained with a crystal spectrometer equipped with a spatially resolving slit. As explained earlier, one-dimensional slit images are suitable for the Abel inversion of self-emission. However, two-dimensional images are necessary in order to judge the symmetry and uniformity, and the usefulness of the one-dimensional data.

Figure 66.23 shows the model-simulated lineouts of continuum radiation images at various photon energies. The images contain the effect of radiation transport through the target layers. The effect of the cold, annular fuel region is evident by the severe attenuation of radiation below ~5 keV.

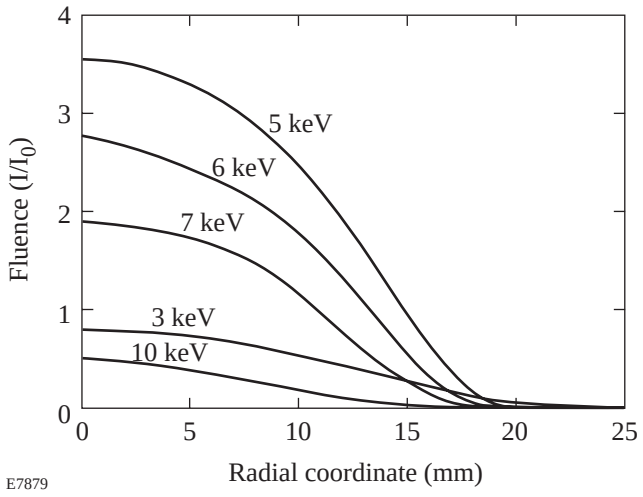

Figure 66.23
Spatial profiles of the emission continuum calculated by the model.[1] The radial coordinate is in the plane of the image (i.e., it is the distance of the line-of-sight from one going through the center of the target). The curves represent the emergent spectra; i.e., they include the attenuation by the cold shell. The normalization intensity I_0, as in Fig. 66.20, equals 7.0×10^{20} keV/(keV ns cm^2 Ω).

We first study the information contained in space-integrated spectra. Figure 66.24 shows a comparison between the time-integrated and space-integrated continuum spectrum calculated by *LILAC* and the peak-compression spectrum calculated by spatially integrating the curves in Fig. 66.23. The comparison serves to show consistency between the two calculations. The difference at the softer end of the spectrum is due to emission before peak compression, from the outer target

layers. Note that since the emission of the compressed core lasts for about 1 ns, the two curves at high energies are comparable. The comparison also shows that the peak temperature of the hot spot can be determined by a time-integrating spectrograph if a sufficiently high-energy part of the spectrum is used to measure the slope. Since the temperatures T_h deduced in Fig. 66.24 are close to the peak temperature in the test implosion (see Fig. 66.19), we conclude that the peak core temperature can be experimentally determined from a spectrograph that integrates the emission in both time and space.

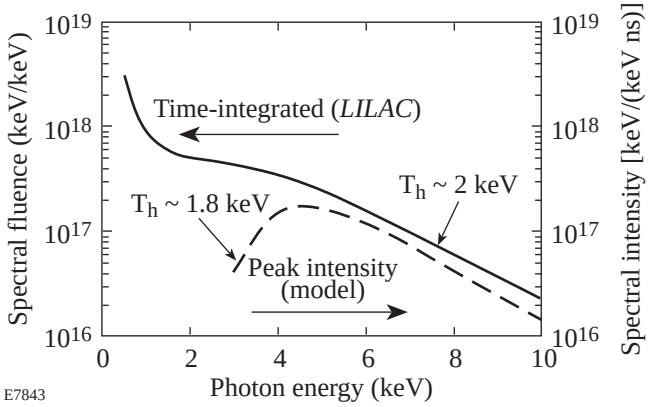

Figure 66.24
Computed continuum spectrum calculated by *LILAC* (time integrated) and by the model described here (at peak compression). Both are integrated over the volume of the target. The curves represent the emergent spectra; i.e., they include the attenuation by the cold shell. The slopes yield the hot-spot temperature T_h.

The ability to measure the core temperature using the high-energy end of the spectrum, where shell attenuation is small, has been recognized previously.[8] However, since the backlighting image provides a measure of the shell attenuation, we can correct for it and extend the usefulness of the continuum to lower photon energies, where the intensity is higher, thus yielding a better signal-to-noise ratio. Figure 66.25 shows the results of such a procedure. For various choices of the shell temperature, the corresponding density profile from Fig. 66.22 was used to calculate the opacity τ_0 along the radial direction, and the lower curve of Fig. 66.25 was then multiplied by $\exp(\tau_0)$. As expected, the resulting curve is a single exponential with the same slope as that of the high-energy part of the emergent spectrum. It is not surprising that the various choices of cold-region temperatures result in the same curve: the points on this curve were obtained from the density profiles of Fig. 66.22 and the corresponding temperatures, all of which were derived from the same backlighting image, thus the same opacity. In simple terms, the opacity correction can be approximately derived directly from the backlighting image, without knowing the density or the temperature.

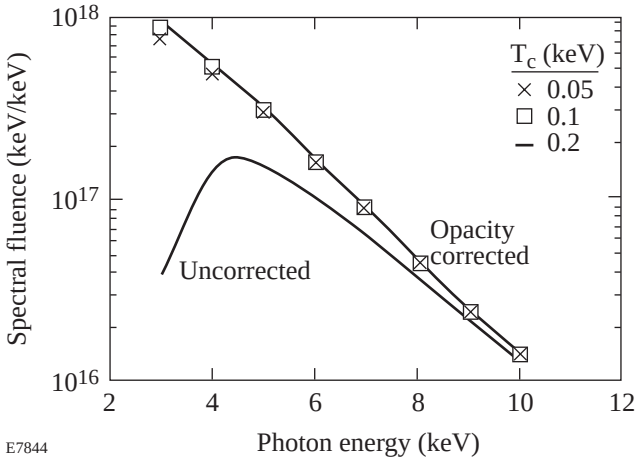

Figure 66.25
Lower curve: model-computed continuum at peak compression (from Fig. 66.24); upper curve and points: the spectrum corrected for absorption by the cold-fuel shell. The results assumed that cold-shell temperatures essentially coincide.

In addition to determining the peak temperature, the spatial temperature profile within the hot spot can be studied as well. To perform this analysis, we begin by simulating another experimental observation. The spectrum at different locations within the hot spot can be calculated from the emergent profiles, such as in Fig. 66.23. Such profiles must be integrated to simulate one-dimensional slit images, then convolved with an instrumental resolution curve (again assumed to be a Gaussian of 10-μm FWHM) and then corrected for the attenuation by the cold shell. We then apply the Abel inversion according to Eq. (2). Two points need to be addressed: (a) This procedure is valid only if the opacity within the hot spot itself is negligible, and (b) the radial opacity τ_0 must be replaced with an opacity calculated (from Eq. 3) separately along each line of sight. Using the profiles in Fig. 66.19 we calculate the opacity of the hot region to be ~0.03 and thus negligible; this is expected because of both the low density and high temperature of this region.

Figure 66.26 shows the resulting spectra at several locations within the hot spot. The unit of local emission (or emissivity) ε_0 is related to the unit of emergent intensity I_0 of Figs. 66.20 and 66.23, i.e., $\varepsilon_0 = 7.0 \times 10^{20}$ keV/(keV ns cm^3 Ω). As expected, the curves each correspond to a well-defined temperature. Finally, the inferred temperature profile

is shown in Fig. 66.27, compared with the *LILAC*-calculated profile from Fig. 66.19. The general agreement between the two curves is expected and provides a check of consistency in the calculations. However, the deviation at the periphery of the hot spot shows the effect of finite spatial resolution. The slit transfers intensity to the lower-intensity parts of the image; since this intensity has a more-pronounced effect on the hardest and weakest parts of the spectrum, the result is a rise in the apparent temperature.

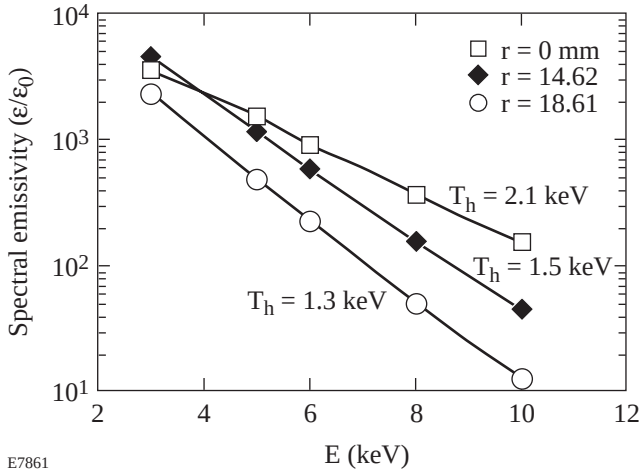

Figure 66.26
Continuum spectra of the emission at various core locations. The emergent profiles of Fig. 66.23 have been integrated to simulate one-dimensional slit images, then convolved with an instrumental resolution curve (assumed to be a Gaussian of 10-μm FWHM), and Abel-inverted according to Eq. (2). The absorption by the cold fuel shell has been accounted for (before Abel-inverting). The emissivity unit is $\varepsilon_0 = 7.0 \times 10^{20}$ keV/(keV ns cm^3 Ω).

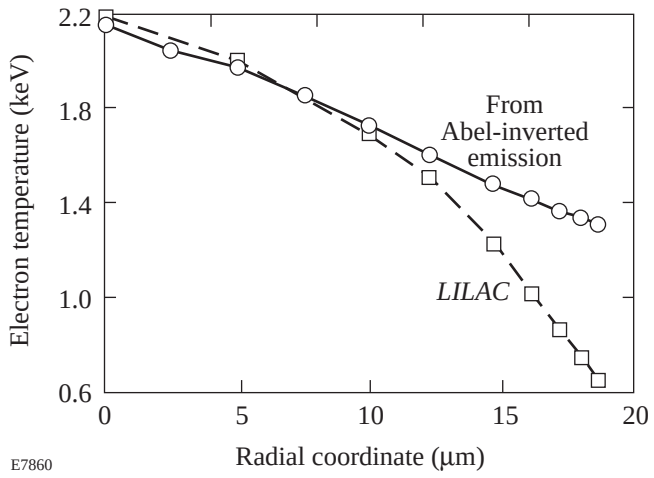

Figure 66.27
Temperature profile in the hot spot, from Fig. 66.26, compared with the *LILAC*-calculated profile at peak compression.

Effect of Noise in the Data

The foregoing analysis has effectively assumed that the data subjected to the Abel inversion is devoid of noise. Starting with the image in Fig. 66.20, we will now study how noise in the measured data affects the inverted results. After convolution with an instrumental broadening curve of 10-μm FWHM, random noise (±25%) is added to the signal and the Abel procedure (assuming T_c = 0.2 keV) is repeated many times. Because the Abel inversion involves a derivative over space [(see Eq. (2)], the data normally has to be smoothed. We apply a 5-point smoothing procedure to the intensity profiles before Abel inverting. This is a mild smoothing since the smoothing range extends over only ~10% of the total range of the image. Figure 66.28 shows several examples of the resulting mass-density profile, compared to the profile with no noise. The error in the mass density increases with the radial coordinate: it is ~15% at $r = 25$ μm and increases to >50% for $r > 45$ μm. This increase is related to the dependence of the opacity τ on the image intensity I. Since $\tau = \ln(I_0/I)$, the relative error in the opacity is related to the relative error in the measured intensity according to $(\Delta\tau/\tau)/(\Delta I/I) = [\ln(I_0/I)]^{0.5}$. Thus, the error in the opacity (and hence in the mass density) increases sharply at large radii, where the opacity is small. However, the error in the mass density is still for the most part smaller than the error due to the uncertainty in the value of T_c. Thus, the latter will determine the total error, especially if the noise in the experimental data is kept below ±25%.

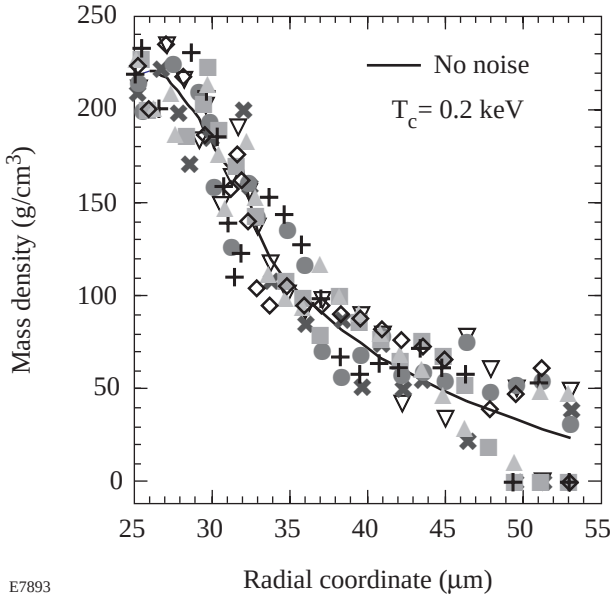

Figure 66.28
Effect of ±25% random noise in the backlighting image on the mass-density profile obtained from Abel inversion. Instrumental resolution of 10-μm FWHM was included.

The same procedure was applied to the emission profiles of Fig. 66.23: after converting these profiles to slit images and accounting for instrumental broadening, a ±25% random noise was added to the points. Then the effect of attenuation by the cold shell was accounted for, and finally the Abel inversion was applied to yield the local spectral emission. Figure 66.29 shows a sample of random noise runs. The error in the local emission increases with the radius up to ±15% for $r = 0$ because, when the profile does not increase toward the center, the Abel inversion essentially involves the subtraction of two almost identical quantities. The resulting temperature at $r = 0$ varies in the range of 2.0 to 2.3 keV, and the variation is even smaller for larger radii. Thus, a ±25% noise in the experimental image results in a relatively small error in the temperature, especially for larger radii, where, conversely, instrumental resolution strongly affects the results (see Fig. 66.27).

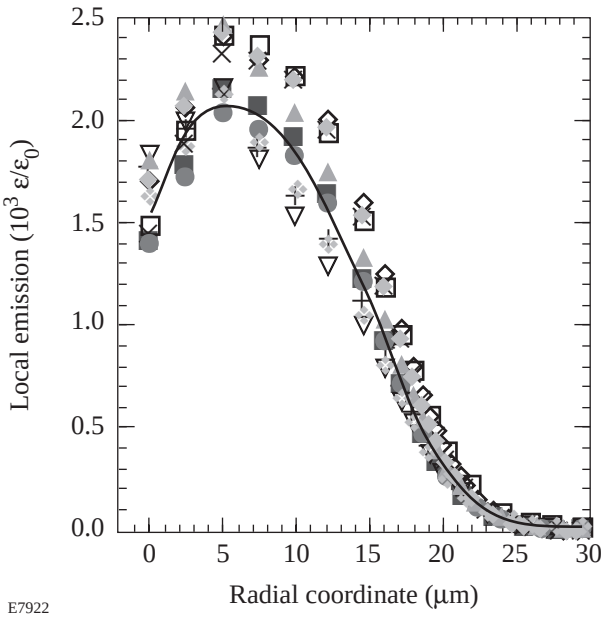

Figure 66.29
Effect of ±25% random noise in the self-emission image on the local emission profile obtained from Abel inversion. Instrumental resolution (of a slit) of 10-μm FWHM was included. The resulting errors in the temperature profile are less than ±10%.

Conclusion

The Abel inversion can greatly enhance the usefulness of either emission or backlit images of imploded targets. The measurement of only the emission from a cryogenic target is of limited value. The deduction of the hot-spot temperature is compromised by not knowing the attenuation through the cold shell. To overcome this difficulty, the spectrum has to be measured at sufficiently high photon energies, where the intensity is low. Likewise, imaging the emission can yield the hot-spot size, but without information on the existence of a cold annular region, the very existence of a hot spot is uncertain. On the other hand, two-dimensional monochromatic backlighting imaging supplemented by one-dimensional polychromatic imaging can yield significant additional information: the former can yield the density distribution within the cold, dense shell, and the latter can yield the temperature distribution within the hot spot. To achieve this, a spatial resolution of ~10 μm in both instruments is required.

ACKNOWLEDGMENT

This work was supported by the U.S. Department of Energy Office of Inertial Confinement Fusion under Cooperative Agreement No. DE-FC03-92SF19460, the University of Rochester, and the New York State Energy Research and Development Authority. The support of DOE does not constitute an endorsement by DOE of the views expressed in this article.

REFERENCES

1. Laboratory for Laser Energetics LLE Review **58**, NTIS document No. DOE/SF/19460-17, 1994 (unpublished), p. 57.
2. B. Yaakobi, F. J. Marshall, Q. Su, and R. Epstein, J. X-Ray Sci. Technol. **5**, 73 (1995).
3. F. J. Marshall and Q. Su, Rev. Sci. Instrum. **66**, 725 (1995); Laboratory for Laser Energetics LLE Review 66, NTIS document No. DOE/SF/19460-125, 1996 (unpublished), p. 60 (this issue).
4. K. Bockasten, J. Opt. Soc. Am. **51**, 943 (1961).
5. N. A. Magnitskii and S. A. Magnitskii, Sov. J. Quantum Electron. **7**, 441 (1977).
6. C. M. Vest and D. G. Steel, Opt. Lett. **3**, 54 (1978).
7. B. Yaakobi, R. Epstein, and F. J. Marshall, Phys. Rev. A **44**, 8429 (1991).
8. F. J. Marshall, J. A. Delettrez, R. Epstein, and B. Yaakobi, Phys. Rev. E **49**, 4381 (1994).

Two-Dimensional Analysis of the Power Transfer between Crossed Laser Beams

The indirect-drive approach to inertial confinement fusion[1] involves laser beams that cross as they enter the hohlraum. Ion-acoustic waves in the plasma at the overlap region can transfer power between the beams. Since this could adversely affect the implosion symmetry, it is important to understand the mechanisms that make such a transfer possible. In this context, two studies have been made of the interaction of crossed laser beams mediated by an ion-acoustic wave. Kruer *et al.*[2] performed a one-dimensional analysis of the steady-state power transfer, emphasizing the effects of different beam frequencies and the inhomogeneity of the plasma. Eliseev *et al.*[3] performed two-dimensional simulations of the interaction of equal-frequency beams in a homogeneous plasma. In addition to observing a time-dependent power transfer between the beams, they observed several secondary processes and supplemented their numerical simulations with one-dimensional analyses of certain processes. Here, we present a two-dimensional analysis of the power transfer between beams of unequal frequency in a homogeneous plasma, for both the transient and steady-state regimes.

Governing Equations

Laser beams that cross interact via ion-acoustic waves in the irradiated plasma. The interaction geometry is shown in Fig. 66.30 and is governed by Maxwell's wave equation[4]

$$\left(\partial_{tt}^2 + \omega_e^2 - c^2\nabla^2\right)A_h = -\omega_e^2 n_l A_h \tag{1}$$

for the electromagnetic potential together with the ion-acoustic (sound) wave equation[4]

$$\left(\partial_{tt} + 2\nu_s\partial_t - c_s^2\nabla^2\right)n_l = \tfrac{1}{2}c_s^2\nabla^2\left\langle A_h^2\right\rangle. \tag{2}$$

The electromagnetic potential $A_h = \left(v_h/c_s\right)\left(m_e/m_i\right)^{1/2}$ is the quiver velocity of electrons oscillating in the high-frequency electric field divided by a characteristic speed that is of the order of the electron thermal speed, n_l is the low-frequency electron-density fluctuation associated with the ion-acoustic wave divided by the background electron density, and the $\langle\ \rangle$ signify that only the low-frequency response to the ponderomotive force was retained.

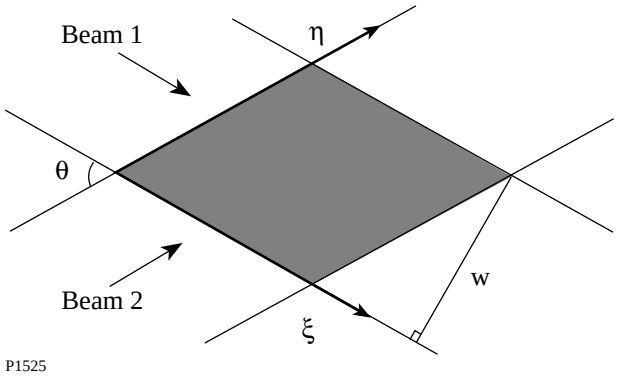

Figure 66.30
Geometry of the interaction of crossed laser beams. The beam widths are equal and denoted by w, and the beam intersection angle is denoted by θ. The characteristic coordinates ξ and η measure distance in the propagation directions of beams 1 and 2, respectively.

By substituting the Ansaetze

$$\begin{aligned} A_h(\xi,\eta,t) \;=\; & A_1(\xi,\eta,t)\,\exp\left[i\left(k_1\xi - \omega_1 t\right)\right] \\ & +\; A_2(\xi,\eta,t)\,\exp\left[i\left(k_2\eta - \omega_2 t\right)\right] + c.c. \end{aligned} \tag{3}$$

and

$$n_l(\xi,\eta,t) = n(\xi,\eta,t)\exp\left[i\left(k_1\xi - k_2\eta\right)\right] + c.c. \tag{4}$$

into Eqs. (1) and (2), and making the slowly varying envelope approximation, one can show that

$$\begin{aligned} \partial_\xi A_1 &= -i\left(\omega_e^2/2\omega_1\nu_1\right)nA_2\exp\left(i\omega t\right), \\ \partial_\eta A_2 &= -i\left(\omega_e^2/2\omega_2\nu_2\right)n^* A_1\exp\left(-i\omega t\right), \end{aligned} \tag{5}$$

and

$$\left(\partial_{tt} + 2\nu_s\partial_t + \omega_s^2\right)n = -\omega_s^2 A_1 A_2^* \exp\left(-i\omega t\right), \qquad (6)$$

where ν_1 is the group velocity of the higher-frequency beam; ν_2 is the group velocity of the lower-frequency beam; $\omega = \omega_1 - \omega_2$ is the difference between the beam frequencies; $\mathbf{k}_s = \mathbf{k}_1 - \mathbf{k}_2$ is the ion-acoustic wave vector; and $\omega_s = c_s k_s$ is the ion-acoustic frequency. The characteristic variables ξ and η measure distance in the propagation directions of beams 1 and 2, respectively. The time derivatives were omitted from Eqs. (5) because the time taken for the laser beams to cross the interaction region is much shorter than the time taken for the ion-acoustic wave to respond to the ponderomotive force.

Steady-State Analysis

In steady state, the beams interact according to

$$\partial_\xi A_1 = \left(i\alpha - \beta\right)\left|A_2\right|^2 A_1,$$
$$\partial_\eta A_2 = \left(i\alpha + \beta\right)\left|A_1\right|^2 A_2, \qquad (7)$$

where the nonlinear coefficients

$$\alpha = \frac{\omega_e^2\omega_s^2\left(\omega_s^2 - \omega^2\right)}{2\omega_2\nu_2\left[\left(\omega_s^2 - \omega^2\right)^2 + 4\nu_s^2\omega^2\right]},$$
$$\beta = \frac{\omega_e^2\omega_s^2\nu_s\omega}{\omega_2\nu_2\left[\left(\omega_s^2 - \omega^2\right)^2 + 4\nu_s^2\omega^2\right]}. \qquad (8)$$

Since $\left|\omega\right| << \omega_1$, the differences between ω_1 and ω_2 and ν_1 and ν_2 were neglected in the first of Eqs. (7).[5] In the Lorentzian approximation

$$\alpha \approx \frac{-\omega_e^2\omega_s\delta}{4\omega_2\nu_2\left(\delta^2 + \nu_s^2\right)}, \qquad \beta \approx \frac{\omega_e^2\omega_s\nu_s}{4\omega_2\nu_2\left(\delta^2 + \nu_s^2\right)}, \qquad (9)$$

where the frequency-detuning parameter $\delta = \omega - \omega_s$. The coefficients α and β characterize the real and imaginary parts, respectively, of the ion-acoustic response to the ponderomotive force [see Eq. (6)]. They are plotted as functions of δ in Fig. 66.31, for the case in which $\nu_s/\omega_s = 0.1$. Both coefficients are normalized to $\omega_e^2\omega_s^2/4\omega_2\omega_s\nu_2\nu_s$, which, apart from a factor of $\left|A_1\right|^2$, is the spatial growth rate of stimulated Brillouin scattering (SBS) in the strong-damping limit. Although the Lorentzian approximation for α becomes less accurate as the magnitude of the frequency-detuning parameter increases, the Lorentzian approximation for β is accurate for arbitrary frequency detuning. For values of ν_s/ω_s larger than 0.1, there are significant discrepancies between the approximate and exact expressions for both coefficients.

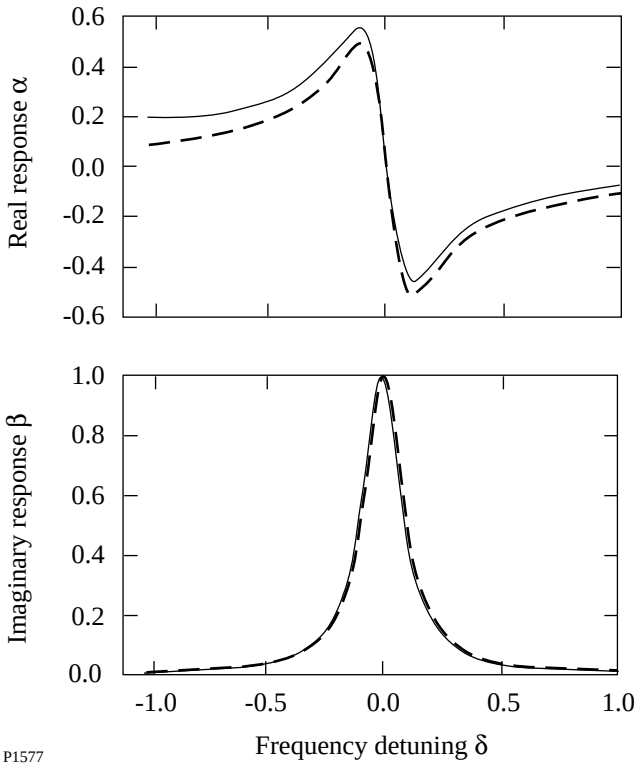

Figure 66.31
Nonlinear coefficients α and β [Eqs. (7)], normalized to the resonant gain coefficient, plotted as functions of the frequency detuning parameter δ/ω_s for the case in which $\nu_s/\omega_s = 0.1$. The coefficients α and β characterize the real and imaginary parts, respectively, of the ion-acoustic response to the ponderomotive force. The solid lines represent the exact coefficients [Eqs. (8)] and the dashed lines represent the approximate coefficients [Eqs. (9)].

Equations (7) are solved subject to the boundary conditions

$$A_1\left(0,\eta\right) = A_0, \qquad A_2\left(\xi,0\right) = \rho A_0, \qquad (10)$$

where ρ is the ratio of the amplitudes of the incident beams. By changing variables according to

$$B_1 = A_1 \exp\left(-i\alpha\int_0^{\xi}|A_2|^2 d\xi'\right),$$
$$B_2 = A_2 \exp\left(-i\alpha\int_0^{\eta}|A_1|^2 d\eta'\right), \tag{11}$$

one can reduce Eqs. (7) to

$$\partial_\xi B_1 = -\beta|B_2|^2 B_1, \qquad \partial_\eta B_2 = \beta|B_1|^2 B_2. \tag{12}$$

It is convenient to define the normalized intensities

$$I_1 = |B_1|^2/|A_0|^2 \text{ and } I_2 = |B_2|^2/|A_0|^2,$$

the normalized distances

$$x = 2\beta|A_0|^2\xi \text{ and } y = 2\beta|A_0|^2\eta,$$

and the normalized beam width

$$l = 2\beta|A_0|^2 w/\sin\theta,$$

where w is the physical beam width and θ is the beam intersection angle (see Fig. 66.30). In terms of these dimensionless variables, Eqs. (12) become

$$\partial_x I_1 = -I_2 I_1, \quad \partial_y I_2 = I_1 I_2 \tag{13}$$

and the boundary conditions [Eqs. (10)] become

$$I_1(0,y) = 1, \quad I_2(x,0) = r, \tag{14}$$

where $r = |\rho|^2$ is the ratio of the beams' intensities.

Despite the fact that Eqs. (13) are nonlinear and describe beam propagation in two directions, there is a way to solve them analytically.[6,7] It is convenient to define

$$P_1(x,y) = \int_0^y I_1(x,y')dy',$$
$$P_2(x,y) = \int_0^x I_2(x',y)\,dx'. \tag{15}$$

Physically, $P_1(x,l)$ is the power in the cross section of beam 1 that is a distance x from the entrance to the interaction region, and $P_2(l,y)$ is the power in the cross section of beam 2 that is a distance y from the entrance to the interaction region. By combining Eqs. (13), one can show that

$$\partial_x P_1 = r\left[1-\exp(P_1)\right], \tag{16}$$

from which it follows that

$$P_1(x,y) = -\log\left\{1-\exp(-rx)\left[1-\exp(-y)\right]\right\}. \tag{17}$$

It then follows from Eq. (17), and the relations $I_1 = \partial_y P_1$ and $I_2 = r\exp(P_1)$, that

$$I_1(x,y) = \frac{\exp(-y)}{\exp(rx)-1+\exp(-y)},$$
$$I_2(x,y) = \frac{r\,\exp(rx)}{\exp(rx)-1+\exp(-y)}. \tag{18}$$

By combining Eqs. (13), one can also show that

$$P_2(x,y) = \log\left\{1+\exp(y)\left[\exp(rx)-1\right]\right\}. \tag{19}$$

Equation (19) and the relations $I_2 = \partial_x P_2$ and $I_1 = \exp(-P_2)$ are consistent with solutions (18).

The beam-intensity profiles are displayed in Fig. 66.32, for the case in which $l = 3$ and $r = 0.01$. Notice that the intensity of beam 1 is nearly constant and the intensity of beam 2 is nearly independent of x. When $rl << 1$, as it is for Fig. 66.32, Eqs. (18) reduce to $I_1 \approx 1$ and $I_2 \approx r\exp(y)$ in agreement with the linearized versions of Eqs. (13).

The beam-intensity profiles are also displayed in Fig. 66.33, for the case in which $l = 3$ and $r = 0.1$. Notice that the intensity profiles are highly two-dimensional. Beam 1 is depleted as it propagates in the x direction, and beam 2 is amplified as it propagates in the y direction. Consequently, the depletion of beam 1 along the characteristic $y = l$ is more rapid than its depletion along the characteristic $y = 0$, and the amplification of beam 2 along the characteristic $x = 0$ is more rapid than its amplification along the characteristic $x = l$.

It follows from Eqs. (17) and (19) that

$$P_2(x,y) - P_2(x,0) = P_1(0,y) - P_1(x,y); \qquad (20)$$

the power gained by beam 2 must equal the power lost by beam 1. The power transfer $P_2(l,l) - P_2(l,0)$ is denoted by $T(l)$ and is given by

$$T(l) = \log\left\{\exp(-rl) + \exp(l)\left[1 - \exp(-rl)\right]\right\}. \qquad (21)$$

Since the normalized incident power is l, the fractional power transfer is $T(l)/l$. This fractional power transfer is plotted as a function of l in Fig. 66.34. It is not difficult to show that $T(l)/l \approx r\left[\exp(l) - 1\right]$ for $rl << 1$ and $l \sim 1$, and $T(l)/l \approx 1$ for $l >> 1$.

Despite the complexity of the beam evolution, which is two-dimensional and nonlinear, the power transfer is characterized by two dimensionless parameters. The first, r, is simply the ratio of the incident beam intensities. The second, l, depends on several dimensional parameters that characterize the beams

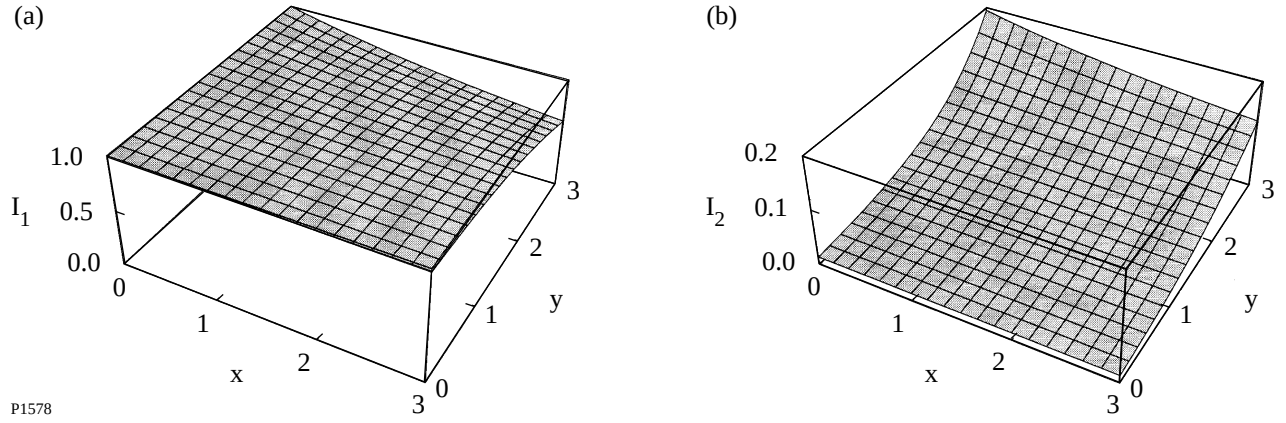

Figure 66.32
Beam-intensity profiles [Eqs. (18)] for the case in which the normalized beamwidth $l = 3$ and the ratio of the incident beam intensities $r = 0.01$. Notice that the intensity of beam 1 is nearly constant and the intensity of beam 2 is nearly independent of x, as linear theory predicts.

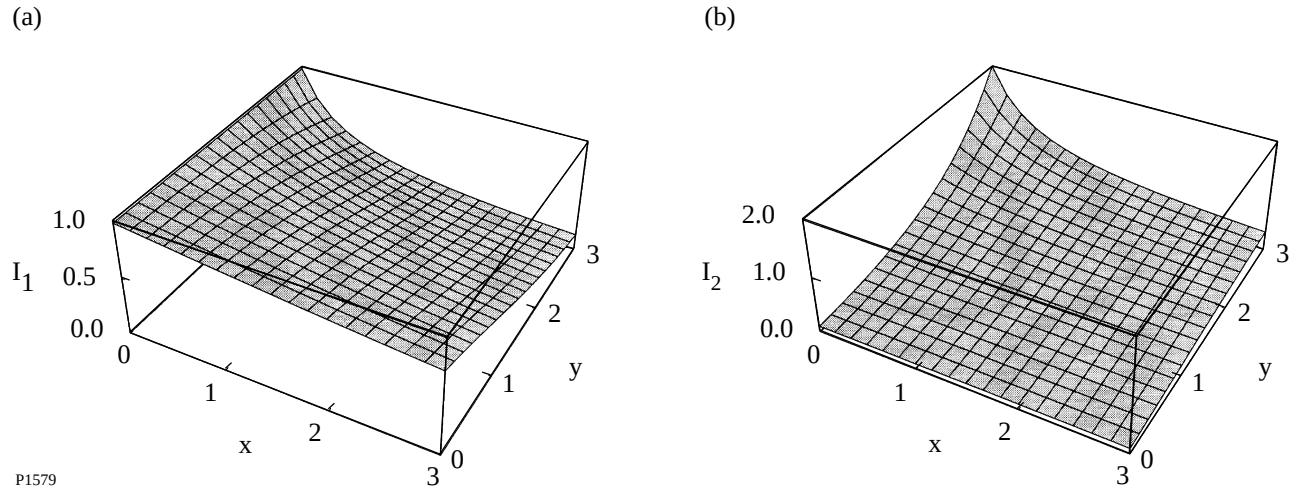

Figure 66.33
Beam-intensity profiles [Eqs. (18)] for the case in which the normalized beamwidth $l = 3$ and the ratio of the incident beam intensities $r = 0.1$. Notice that the intensity profiles are highly two-dimensional.

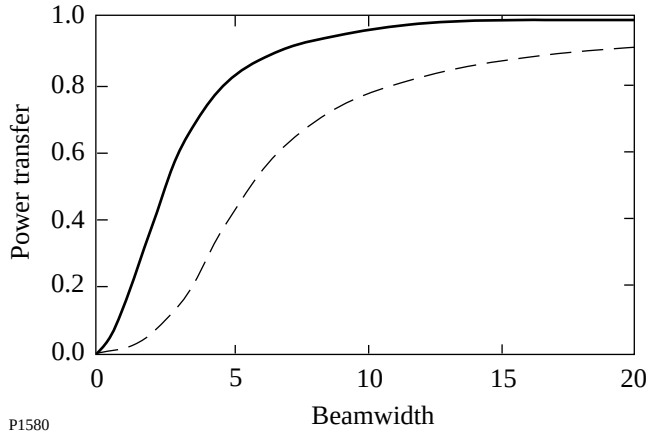

Figure 66.34
Fractional power transfer from beam 1 to beam 2 [Eq. (21)] plotted as a function of the normalized beamwidth l for two values of r, the ratio of the incident beam intensities. The dashed line corresponds to $r = 0.01$, and the solid line corresponds to $r = 0.1$.

and the plasma. As a numerical example, suppose that the electron density $n_e = 10^{20}$ cm^{-3}, the electron temperature $T_e =$ 1 keV, the ion temperature $T_i = 0.5$ keV, the laser wavelength $\lambda_0 = 0.35$ μm, the laser intensity $I_0 = 10^{15}$ Wcm^{-2} and the beamwidth $w = 1$ mm. For these parameters $l \approx 2.7$. One can infer the value of l for other parameters by using the fact that, with the electron-to-ion temperature ratio fixed, l is proportional to $n_e\lambda_0 I_0 w$ and is inversely proportional to T_e.

Since Eq. (21) is valid for $0 < \theta < \pi$, the angular dependence of l is also of interest. When $\delta = 0$, $\beta|A_0|^2$ is the spatial growth rate of SBS. For an ion-acoustic wave subject to Landau damping, this growth rate is independent of θ.[8,9] In this case, l is inversely proportional to $\sin\theta$: the power transfer is larger for beams that are nearly parallel or antiparallel because they overlap for a longer distance. The importance of $\delta \neq 0$ is measured relative to ω_s and v_s, both of which are proportional to $\sin(\theta/2)$. Thus, the power transfer is more sensitive to detuning when the beams are nearly parallel and less sensitive when the beams are nearly antiparallel.

When $\delta \neq 0$, the interaction of beams 1 and 2 causes their phases to be shifted by ϕ_1 and ϕ_2, respectively. It follows from Eqs. (11) and (15) that

$$\phi_1(y) = \alpha P_2(l,y)/2\beta I_0, \quad \phi_2(x) = \alpha P_1(x,l)/2\beta I_0. \quad (22)$$

The normalized phase shifts $P_2(l,y)$ and $P_1(x,l)$ are plotted as functions of position in Fig. 66.35. An observer traveling with

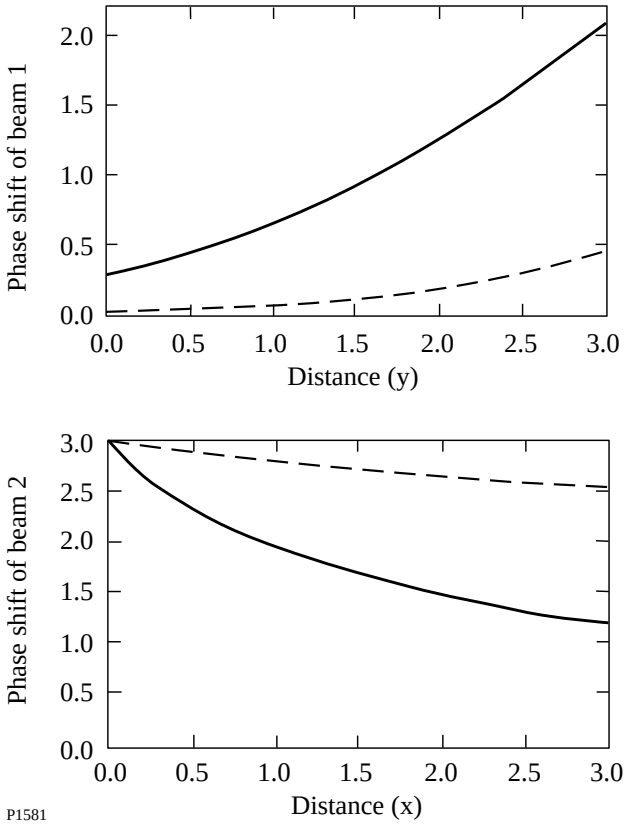

Figure 66.35
Normalized phase shifts [Eqs. (22)] plotted as functions of position for the case in which the normalized beamwidth $l = 3$ and for two values of r, the ratio of the incident beam intensities. The dashed lines correspond to $r = 0.01$, and the solid lines correspond to $r = 0.1$. The spatial inhomogeneity of these phase shifts causes the beams to be deflected.

either beam would measure a larger normalized phase shift on the left side of the beam.

For beams of moderate width ($l \sim 1$), the variation of phase with distance is approximately linear and the beam deflection angles θ_1 and θ_2 are easily estimated. It follows from the laws of geometrical optics that

$$\theta_1 \approx [\phi_1(l) - \phi_1(0)]/k_1 w, \quad \theta_2 \approx [\phi_2(0) - \phi_2(l)]/k_2 w. \quad (23)$$

By combining Eqs. (22) and (23), and neglecting the difference between k_1 and k_2, one can show that

$$\theta_1 \approx \theta_2 \approx (\alpha/k_2 \sin\theta)[T(l)/l]. \quad (24)$$

Both beams are deflected in the same angular direction: anticlockwise when $\delta < 0$ and clockwise when $\delta > 0$. Because the fractional power transfer depends on l and, hence, on β, the beam deflection angle [Eq. (24)] depends on both α and β. It is evident from Fig. 66.31 that the magnitude of the beam deflection angle is largest when $|\delta| \sim v_s$. When $\delta = 0$ or $\delta = -\omega_s$, the beams are not deflected.

For wide beams ($l >> 1$) the phase of beam 1 still varies approximately linearly with distance and the first of Eqs. (24) is still valid. Unfortunately, the variation with distance of the phase of beam 2 is highly nonlinear, and it is difficult to estimate the beam deflection angle and focusing distance. In this case, however, the power transfer from beam 1 to beam 2 is complete: the irradiation symmetry is destroyed and the issues of beam deflection and focusing are irrelevant.

The beam deflection angle is larger for beams that are nearly parallel or antiparallel because the nonlinear phase shifts that deflect the beams are proportional to the power transfer. For the same reason, the beam deflection angle is more sensitive to detuning when the beams are nearly parallel and less sensitive to detuning when the beams are nearly antiparallel.

Transient Analysis

Equations (18) and (21) describe completely the steady-state power transfer between beams 1 and 2. However, it is important to know how long the beam interaction takes to reach steady state. If this saturation time is comparable to the duration of the interaction, the transient power transfer must also be determined.

The case in which $\delta = -\omega_s$ has been studied theoretically and experimentally.[10,11] In steady state, beam 2 is unamplified. However, the response of the ion-acoustic wave to a steady ponderomotive force includes a resonant transient that is required to satisfy the initial conditions. This resonant response produces a frequency-downshifted component of beam 2. In turn, the frequency-downshifted component of beam 2 gives rise to a component of the ponderomotive force that drives the ion-acoustic wave resonantly. Because of this feedback mechanism, the transient (SBS) grows considerably and lasts for a time that is long compared to the damping time of the ion-acoustic wave.

We consider here the complimentary case in which $|\delta| << \omega_s$, and the linearized equations can be simplified and solved exactly. It is advantageous to work in terms of the ion-acoustic amplitude

$$N(\xi,\eta,t) = n(\xi,\eta,t)\exp(i\omega t), \tag{25}$$

which satisfies the simplified equation

$$(\partial_t + v_s - i\delta)N = -i(\omega_s A_0/2)A_2^*. \tag{26}$$

Subject to the normalized boundary and initial conditions

$$A_2(0,\eta,t) = 1, \quad A_2(\xi,\eta,0) = 1, \tag{27}$$

which differ from the physical conditions by a factor of ρA_0, and the initial condition

$$N(\xi,\eta,0) = 0, \tag{28}$$

the solution of Eq. (26) and the second of Eqs. (5) is

$$\begin{aligned} A_2(\eta,t) &= 1 + \gamma\int_0^t (\eta/v_2 t)^{1/2} I_1\left[2\gamma(\eta t'/v_2)^{1/2}\right] \\ &\quad \times \exp\left[-(v_s - i\delta)t'\right]dt', \\ N(\eta,t) &= -i(\omega_s A_0/2)\int_0^t I_0\left[2\gamma(\eta t'/v_2)^{1/2}\right] \\ &\quad \times \exp\left[-(v_s - i\delta)t'\right]dt', \end{aligned} \tag{29}$$

where

$$\gamma = \left(\omega_e^2\omega_s^2|A_0|^2/4\omega_2\omega_s\right)^{1/2} \tag{30}$$

is the temporal growth rate of SBS in an infinite plasma and I_m denotes a modified Bessel function of the first kind, of order m (rather than a beam intensity). It is evident from this solution that the linear evolution of beam 2 is one-dimensional. As $t \to \infty$,

$$\begin{aligned} A_2(\eta,t) &\to \exp\left[\gamma^2\eta/v_2(v_s - i\delta)\right], \\ N(\eta,t) &\to -\left[i\omega_s A_0/2(v_s - i\delta)\right]\exp\left[\gamma^2\eta/v_2(v_s - i\delta)\right], \end{aligned} \tag{31}$$

in agreement with the linearized versions of Eqs. (13).

The normalized intensity of beam 2 is plotted as a function of $v_s t$ in Fig. 66.36 for the case in which the spatial growth parameter $\gamma^2\eta/v_2 v_s = 3$ and for three values of δ. The oscil-

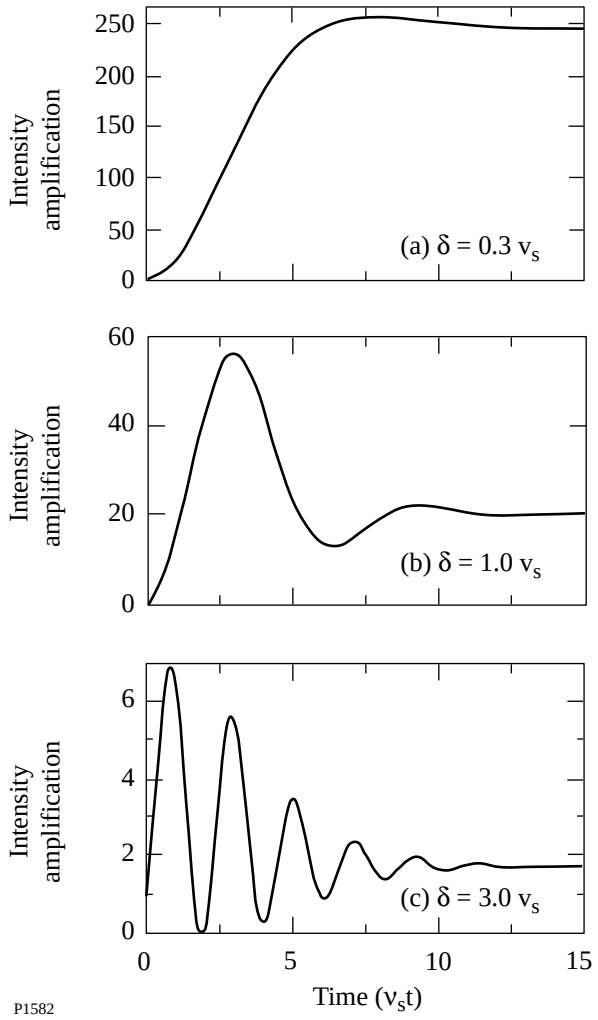

Figure 66.36
Intensity amplification of beam 2 [which follows from the first of Eqs. (29)] plotted as a function of $v_s t$ for the case in which the spatial growth parameter $\gamma^2\eta/v_2 v_s = 3$. (a) $\delta = 0.3\ v_s$; (b) $\delta = 1.0\ v_s$; (c) $\delta = 3.0\ v_s$.

lations in beam intensity are due to the beating of the driven response and the resonant transient. As the magnitude of δ increases, the maximal transient intensity decreases less than the steady-state intensity, so the transient becomes more important. For the case in which $\delta = 0$, the linear saturation time is[8,9]

$$t_s \approx 2\gamma^2\eta/v_2 v_s^2 . \qquad (32)$$

When $\delta \neq 0$, some oscillations persist for a longer time, but the beam intensity is of the order of the steady-state intensity at this time: the saturation time does not depend sensitively on δ and is well approximated by Eq. (32).

For a fixed value of η, the saturation time is inversely proportional to $\sin(\theta/2)$.[8,9] However, in the present context, the maximal value of η is $w/\sin\theta$ and the saturation time is inversely proportional to $\sin\theta\sin(\theta/2)$. Thus, the saturation time is longer for beams that are nearly parallel or antiparallel, and the increase in saturation time is larger for beams that are nearly parallel.

It is evident from Figs. 66.32 and 66.33 that two-dimensional evolution signifies the convective depletion of beam 1, which is a nonlinear effect. When the beams are only moderately wide or the ratio of the incident beam intensities is small, the steady-state interaction of the beams is approximately one-dimensional and is consistent with the linearized Eqs. (31). For these cases we expect the transient evolution of the beams to be well described by Eqs. (29). However, when the beams are wide or the incident intensities are comparable, the depletion of beam 1 is significant and the nonlinear Eqs. (5) and (26) must be used to determine the transient evolution of the beams.

Numerical Simulations

Equations (5) and (26) were solved numerically, and the total power passing through the exit boundary of each beam was determined as a function of time. The power amplification of beam 2 is plotted as a function of $v_s t$ in Fig. 66.37 for the case in which $\gamma^2\eta/v_2 v_s = 3$ and for three values of δ. The dashed line corresponds to $r = 0.01$, for which the maximal amplification is 101, and the solid line corresponds to $r = 0.1$, for which the maximal amplification is 11. Although plotting the power amplification rather than the absolute power transfer disguises the fact that $T(l)/l \leq 1$, it facilitates a comparison of the analytical and numerical results. In particular, the deviation of the two numerical curves from one another signals the onset of nonlinearity.

By comparing Figs. 66.36 and 66.37 one notes that when $r = 0.01$, the predictions of linear theory are quantitatively correct for $\delta = 3.0\ v_s$ and qualitatively correct for $\delta = 1.0\ v_s$ and $\delta = 0.3\ v_s$. When $r = 0.1$, the predictions of linear theory are qualitatively correct for $\delta = 3.0\ v_s$ and incorrect for $\delta = 1.0\ v_s$ and $\delta = 0.3\ v_s$. The numerical results show that the onset of nonlinearity is more rapid, and its effect on the transient and steady-state power amplification is more dramatic when the incident intensity of beam 2 is high or the normalized beam width is large [see the second of Eqs. (8) and (9), and Fig. 66.31].

When nonlinearity is important, the interaction saturates more quickly than linear theory predicts. The extent to which

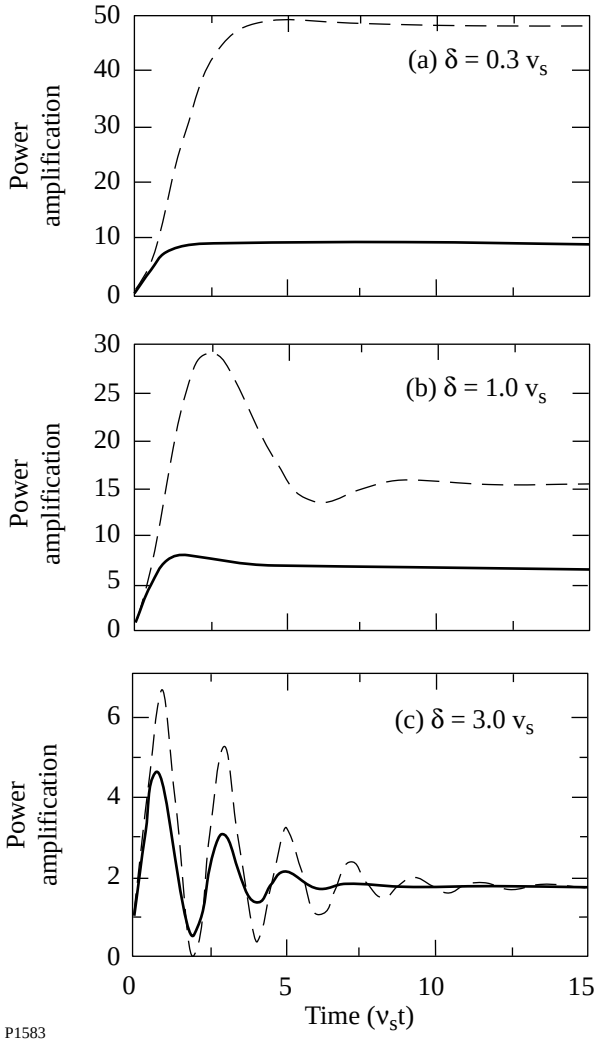

Figure 66.37
Power amplification of beam 2 plotted as a function of $v_s t$ for the case in which the spatial growth parameter $\gamma^2\eta/v_2 v_s = 3$. The power amplification was determined numerically for two values of r, the ratio of the incident beam powers. The dashed line corresponds to $r = 0.01$, for which the maximal amplification is 101, and the solid line corresponds to $r = 0.1$, for which the maximal amplification is 11. (a) $\delta = 0.3\ v_s$; (b) $\delta = 1.0\ v_s$; (c) $\delta = 3.0\ v_s$.

beam 1 is depleted changes in the time taken for the beams to cross the interaction region. In the model Eqs. (5) and (26) this transit time is instantaneous. Thus, the depletion of beam 1 allows both beam intensities to adjust to their steady-state profiles on a time scale that is short compared to the damping time scale inherent in linear theory.

Nonlinearity becomes important when $2\gamma(\eta t/v_2)^{1/2}$, the argument of the amplifying terms in Eqs. (29), reaches a critical value that is inversely dependent on r. It follows from this condition that the nonlinear saturation time is inversely proportional to $\gamma^2\eta$. For fixed η, the nonlinear saturation time is inversely proportional to $\sin(\theta/2)$, as is the linear saturation time [Eq. (32)]. However, in the present context the maximal value of η is $w/\sin\theta$ and the nonlinear saturation time is proportional to $\cos(\theta/2)$.

Summary

The power transfer between crossed laser beams made possible by an ion-acoustic wave was studied in detail. Despite the complexity of the beam evolution, which is two-dimensional and nonlinear, a simple formula was derived for the steady-state power transfer. This power transfer depends on two dimensionless parameters: the ratio of the incident beam intensities and the normalized beamwidth. The normalized beamwidth is proportional to the physical beamwidth and the intensity of the higher-frequency beam, and is inversely dependent on the detuning of the laser difference frequency from the ion-acoustic frequency. Numerical simulations showed that the transient power transfer is larger than the steady-state power transfer and usually oscillates in time. The convective depletion of the higher-frequency beam saturates the power transfer more quickly than the damping of the ion-acoustic wave. The deflection of each beam by the other was also studied briefly.

The analysis of this article is based on the standard model[2] in which the beams are assumed to be monochromatic and their interaction is assumed to be in steady state. This simplified model allows one to understand the basic physics of the power transfer from the higher-frequency beam to the lower-frequency beam. A more realistic model[1] would allow the beams to have many frequency components. The analysis of such a model, in both the transient and steady-state regimes, will be the subject of future work.

ACKNOWLEDGMENT

This work was supported by the National Science Foundation under Contract No. PHY-9057093, the U.S. Department of Energy (DOE) under Contract No. W-7405-ENG-36, the U.S. Department of Energy Office of Inertial Confinement Fusion under Cooperative Agreement No. DE-FC03-92SF19460, the University of Rochester, and the New York State Energy Research and Development Authority. The support of DOE does not constitute an endorsement by DOE of the views expressed in this article.

REFERENCES

1. J. D. Lindl, Phys. Plasmas **2**, 3933 (1995).
2. W. L. Kruer *et al.*, Phys. Plasmas **3**, 382 (1996).

3. V. V. Eliseev, W. Rozmus, V. T. Tikhonchuk, and C. E. Capjack, "Interaction of Crossed Laser Beams with Plasmas," to be published in Physics of Plasmas.

4. W. L. Kruer, *The Physics of Laser Plasma Interactions,* Frontiers in Physics, Vol. 73 (Addison-Wesley, Redwood City, CA, 1988), Chaps. 7 and 8.

5. The normalized action flux amplitudes A_1 and $\left(\omega_2 \nu_2 / \omega_1 \nu_1\right)^{1/2} A_2$ satisfy Eqs. (7) exactly.

6. M. Maier, W. Kaiser, and J. A. Giordmaine, Phys. Rev. **177**, 580 (1969).

7. T. Speziale, Phys. Fluids **27**, 2583 (1984).

8. C. J. McKinstrie, R. Betti, R. E. Giacone, T. Kolber, and J. S. Li, Phys. Rev. E **50**, 2182 (1994).

9. R. E. Giacone, C. J. McKinstrie, and R. Betti, Phys. Plasmas **2**, 4596 (1995).

10. J. S. Li, C. J. McKinstrie, C. Joshi, and K. Marsh, Bull. Am. Phys. Soc. **39**, 1584 (1994).

11. K. Marsh, C. Joshi, and C. McKinstrie, Bull. Am. Phys. Soc. **39**, 1585 (1994).

Low-Surface-Energy Photoresist as a Medium for Optical Replication

Replication of precision surfaces is an inexpensive fabrication method for both small- and large-diameter optical devices. It is useful for producing a wide variety of surface features in polymers for applications ranging from binary or multiple-step diffraction elements and grating structures, to asphere correction layers, lenslet arrays, waveguiding structures, and more.

In these applications, a master surface relief is created by exposing photoresist through a suitably designed grayscale-intensity mask. Development of the resist produces a profiled surface according to the mask transmittance and exposure. Components can be replicated from this master by contact molding; this requires a release layer to insure the master and replicant can be separated without damage to either. Typically, this release layer is an evaporated metal-glucose-metal sandwich structure that allows separation without loss in modulation-function fidelity.[1] Ideally, the on-demand separation between the surfaces occurs at the glucose layer, and by reevaporating the glucose and a single metal layer, the master is ready for repeated use. This is akin to polymer injection molding, where the metal mold ("master") is also reused for thousands of injection operations before wear requires replacement. In *practice*, however, the metal-glucose-metal release layer disintegrates unevenly or adheres to the master. To save the master for reuse, the release-layer residues must be entirely removed and then redeposited. The former requires chemical etching, which tends to wear the photoresist master, significantly reducing its useful life. In some cases, the production of new-exposure masters or several masters at once can be inexpensive; however, for optical elements of large diameter, such as required by inertial-confinement-fusion lasers, this can require many, costly-to-prepare, precision-polished master substrates. The development of sixty, 30-cm-diam distributed phase plates for OMEGA necessitated the search for a simplified approach to a *deterministic* master-replicant release operation in optical replication. Since surface energy determines the adhesion of contacting surfaces, the solution lies in the development of a photoresist that has a low surface energy, thereby obviating the need for a release layer.

In this article, we describe a first step toward developing, by environmentally benign methods,[2] a resist that has a low surface energy and maintains the desired photosensitivity. In its first implementation, the combination of photoresist and on-demand, mechanical release action in a single medium is realized as a *guest-host* version. Since this technique is compatible with current technology, it has the potential for widespread acceptance.

Siloxanes and fluorinated alkanes (and more recently fluorinated siloxanes[3]) have been used as low-surface-energy materials.[4] *Functionalizing* a poly(styrene), i.e., novolac-like, block with a siloxane block to form a diblock resist for reactive ion etching has also been reported recently.[5] In Ref. 5, it is also mentioned that such block grafting could be used to fabricate controlled-surface-energy polymers; however, no data are given in support of this assertion. *Doping* of a siloxane or perfluoroalkane into commercial photoresist to lower the surface energy entails two key issues: (1) Is the dopant miscible in the novolac/solvent matrix in quantities necessary to accomplish significant surface-energy reduction, and (2) can the normal resist development process still transfer the mask modulation function in the presence of the dopant? Here we address these two issues and report results for siloxane. The perfluoroalkane systems are currently plagued by poor planarity of surfaces and pore formation during solvent removal. These problems appear to be solvable.

Novolac resin, the major constituent of traditional photoresists, is a highly hydroxylated oligomer that dissolves well in 1,2-propanediol monomethylether acetate, as does the typical photoactive resist constituent diazonaphthaquinone (DNQ). The generally narrow solvent range in which most siloxanes must be processed can be extended to include the novolac/solvent system by adding hydroxyl functionalities to the siloxane. Poly(phenyl, propyl)silsesquioxane is a commercially available, inexpensive siloxane polyol that yields the best miscibility within the Shipley novolac resist families 1400 and S1800 without precipitation up to 40-wt% doping.[6] The

actual precipitation limit for this mixture was not determined. It was merely ascertained that for up to 40-wt% doping, no fluid phase separation occurs for temperatures up to the resist bake temperature (most resists are baked before exposure to UV light). Also, no solid copolymer phase separation was seen under visible-light microscopy after stripping the solvent. The silsesquioxane was used as received, after thin-layer chromatography detected no measurable, low-polarity, UV-detectable or stainable impurities. The molecular-weight dispersity of the silsesquioxane was not measured. Upon completion of dissolution of the silsesquioxane in the commercial resist (Shipley S1800), the mixture was filtered under protective lights through a 0.5-μm pore membrane for particulate (dust) removal.

When irradiated, the DNQ/novolac crosslinking mechanism involves the phenolic O-H sites in novolac.[7] We surmise that the silsesquioxane O-H sites are equally eligible for ketocarbene attachment reactions, especially since the propyl spacer reduces the silane influence. For this reason, the term *copolymer* or *polymer blend* seems justified for the mixture reaction product.

The effect of siloxane concentration on the polymer surface energy was determined by static contact-angle measurements using 18-MΩ water as reference fluid. Samples containing different silsesquioxane concentration were spin coated on fused-silica substrates, air dried for solvent removal, irradiated (without mask) under a Hg lamp (365-nm output), and developed by standard methods. Under microscope observation,[8] water droplets were placed on the sample surfaces, using a Hamilton microdispenser. Within 5 to 10 s after placing the drop on a respective surface, the image of the droplet was captured, and the contact angle at the surface was measured. In Fig. 66.38 the measured contact angles are plotted against weight-percent concentration of polysilsesquioxane. Errors in both angle measurement and concentration are smaller than the data points indicated. As Fig. 66.38 shows, there is a range of concentrations where the copolymer surface energy can be minimized, i.e., the contact angle reaches a peak. This concentration interval is well below the 40-wt% dopant concentration previously mentioned.

To test the surface-relief-generation capability of the copolymer, a 10-cm-diam sample, with 10-wt% concentration of poly-silsesquioxide, was irradiated under an Ar-laser interference (holographic) grating (364 nm) and developed in the same manner as an undoped resist (i.e., in an aquesous alkaline developer—Shipley MF-312 CD-27). The sinusoidal irradiation and the developer parameters were chosen so that the grating aspect ratio was within the resolution of atomic force microscopy (AFM) with a 70° probe-tip angle. For a 700-nm groove spacing, a 150-nm groove depth was chosen. The tradeoff in grating efficiency intrinsic to shallow gratings was of no concern here. The grating carries all spatial frequency features commensurate with the design goal. On thinner, 38-mm-diam, borosilicate-glass substrates, witness films were spin cast for flat-field illumination and subsequent refractive-index measurements using waveguide refractometry.[9] Doping the hydroxylated silsesquioxane into the photoresist at 10 wt% lowered the 632-nm refractive index from 1.60(8) to 1.59(4). Both average numbers carry ~2% errors.

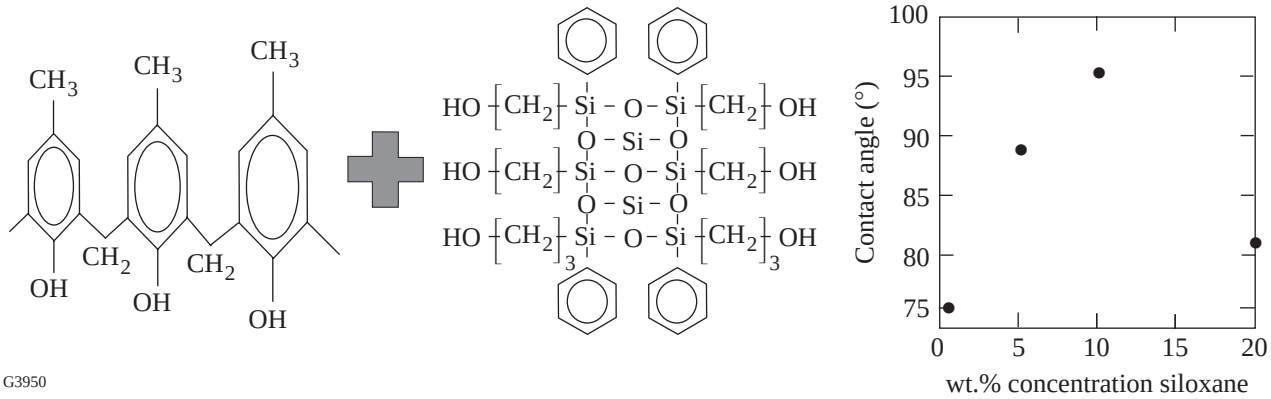

Figure 66.38
Contact angle for 18-MΩ water on photoresist/silsesquioxane blends as a function of silsesquioxane concentration

The results for this grating development are shown in the AFM map in Fig. 66.39(a). A 10-μm × 10-μm raw-data scan output[10] depicts, in a head-on view, the grating structure whose profile is shown as a lineout oriented orthogonally to the grating grooves [Fig. 66.39(b)]. In this instance, the lineout orientation is inclined by ~15° to the scan direction. To accommodate the large sample size, a stand-alone AFM model was used in contact mode.[11] Modification of the sample (due to material drag) during scanning in this mode (a phenomenon frequently encountered with soft, organic thin films[12]) was avoided by minimizing the force used and by reducing the scan speed. The sinusoidal groove depths derived from Fig. 66.39(b) are in reasonable agreement with those obtained from grating transmission efficiency measurements using several-millimeter-diameter optical-probe beams at 543 nm and 1054 nm. The grating efficiency was modeled using an electromagnetic code called SIGMA.[13]

To determine whether microphase separation occurs upon photoinitiated crosslinking, and to identify a possible cause for the weakly irregular grating edges depicted in Fig. 66.39(a), several flat-field samples were also mapped by AFM. This series comprised three samples: one in which the initiator dye and DNQ were removed[14] such that no photopolymerization could take place; one that was irradiated but not developed further; and one that was fully developed. As shown in Fig. 66.40(a), the 10-wt% mixture of initiator-free, DNQ-free photoresist with silsesquioxane yields pinhole-free, smooth films after spin coating and air drying. The irradiated film

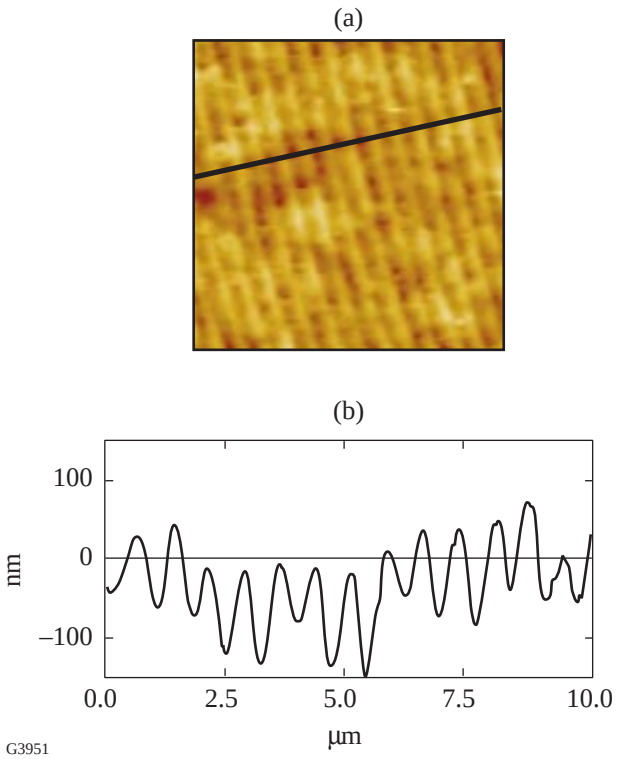

Figure 66.39
(a) Atomic-force microscopy map of 10-μm × 10-μm grating area. The straight line across the image indicates the orientation of the lineout depicted in Fig. 66.39(b). Short horizontal features are indicative of soft material being dragged by the probe tip into grating grooves. (b) Orthogonal lineout through grating structure depicted in Fig. 66.39(a).

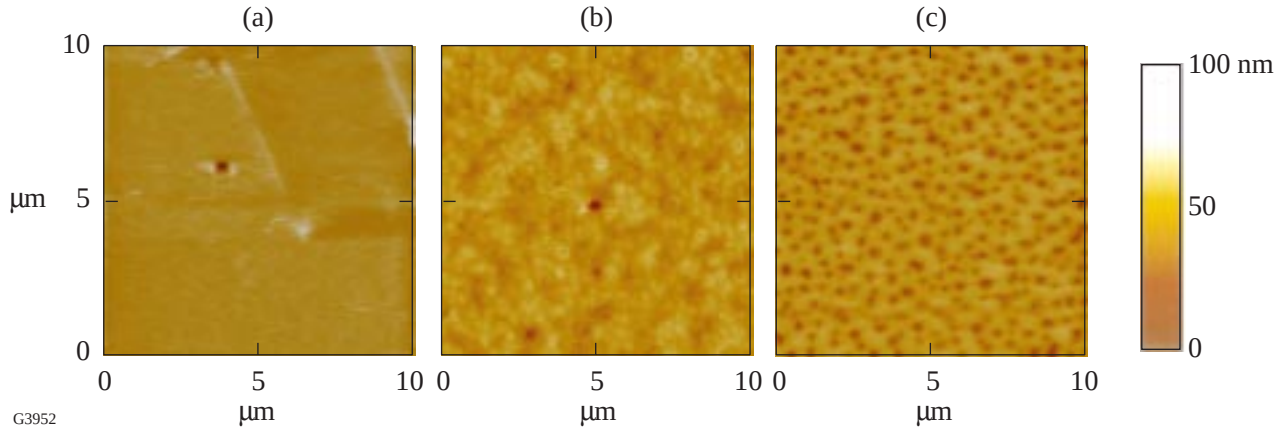

Figure 66.40
(a) AFM scan of unactivated blend of photoresist and 10-wt% silsesquioxane. Except for one pinhole, the surface is smooth (3.1 nm rms). (b) 10-μm × 10-μm AFM scan of irradiated blend of composition as in Fig. 66.40(a). Submicron-sized clusters have formed, leading to a roughened surface (5.2 nm rms). (c) Development of the blend in aqueous-alkaline developer removes the near-surface clusters, leaving a slightly porous surface behind (7.0 nm rms).

[Fig. 66.40(b)] shows slight clustering, with clusters protruding up to 20 nm above the film top-surface average. Upon development [Fig. 66.40(c)], these clusters appear to be preferentially attacked, leaving 20- to 30-nm-deep voids. Since AFM does not offer universal speciation capability, it was impossible to determine from these images the stoichiometry of these clusters, and no strict inference about their formation mechanism could be made.

In summary, a silsesquioxane/photoresist mixture has potential as a combined resist/release medium with low surface energy for simplified optical replication. The guest-host mixture can be developed using normal aqueous-alkali resist developer and established procedures. The tendency of such a mixture to form, upon irradiation, phase-segregating clusters that are preferentially removed by the developer is an application impediment for fine-line-transfer replication. It explains the grating-edge roughness observed in Fig. 66.38. After these first trials, neither the mechanism for the cluster formation nor the optimum exposure conditions for suppressing this cluster formation are known. As a typical feature of guest-host systems, this phenomenon can be avoided entirely by resorting to *functionalized*-siloxane-polyol additions.

ACKNOWLEDGMENT

We thank Brian Taylor for assistance in contact-angle measurements, Lawrence Iwan for image-analysis support, and the Center for Optical Manufacturing (COM), a DoD Center of Excellence by the U.S. Army Materiel Command, for use of the atomic force microscope. This work was supported by the U.S. Department of Energy Office of Inertial Confinement Fusion under Cooperative Agreement No. DE-FC03-92SF19460, the University of Rochester, and the New York State Energy Research and Development Authority. The support of DOE does not constitute an endorsement by DOE of the views expressed in this article.

REFERENCES

1. H. M. Weissman, Opt. Eng. **15**, 435 (1976).
2. D. Satas, ed. *Handbook of Pressure Sensitive Adhesives*, 2nd ed. (Van Nostrand Reinhold, New York, 1989), Chap. 23, pp. 585–600.
3. E. Beyou *et al.*, Tetrahedron Lett. **36**, 1843 (1995).
4. There is a rich Patent Literature covering this area. Two recent examples are P. B. Willis, P. M. McElroy, and G. H. Hickey, U. S. Patent No. 5,266,222 (30 November 1993); and S. B. Lin, U. S. Patent No. 5,436,303 (25 July 1995).
5. A. H. Gabor *et al.*, Chem. Mater. **6**, 927 (1994).
6. SST-3PP1, Molecular Weight: ~1600, GELEST, Inc., Tullytown, PA 19007-6308. A similar compound from another source has been reported as a dry-etch photoresist additive by D. R. McKean, N. J. Clecak, and A. F. Renaldo, J. Vac. Sci. Technol. B **9**, 3413 (1991) .
7. N. P. Hacker, in *Processes in Photoreactive Polymers*, edited by V. V. Krongauz and A. D. Trifunac (Chapman and Hall, New York, 1995), p. 368.
8. D. Li and A. W. Neumann, J. Colloid Interface Sci. **148**, 190 (1992).
9. Metricon Model 2010 Prism Coupler Refractive-Index Measurement System.
10. No software filters were applied to this image for processing or feature enhancement purposes.
11. NanoScope III, Model SA-AFM-1 StandAlone AFM (Digital Instruments, Inc., Santa Barbara, CA).
12. F. Biscarini *et al.*, Phys. Rev. B, Condens. Matter **52**, 14,868 (1995).
13. Supplied by L. Li, University of Arizona, Tucson, AZ (1992).
14. Received from Shipley, Inc.

Surface Microroughness of Optical Glasses under Deterministic Microgrinding

The Center for Optics Manufacturing (COM) at the University of Rochester has made significant advances in the fabrication of precision optical components using deterministic microgrinding with rigid, computer-controlled machining centers and high-speed tool spindles. In deterministic microgrinding, the infeed rate of the microgrinding tool across the optical workpiece is optimized and controlled. This leads to precise knowledge of the amount of removed material when microgrinding optical glasses. This method has been applied to manufacturing convex and concave spherical surfaces with radii 5 mm to ∞ (i.e., planar), and work diameters from 10 to 150 mm have successfully been formed.[1–5] Aspherical surfaces have also been manufactured. After less than 5 min of deterministic microgrinding, the resulting specular surfaces have typical rms microroughness of less than 20 nm, 1 μm of subsurface damage, and a surface figure better than 1/2 wave peak to valley.[6] Typical infeed rates are 6 to 10 μm/min with 2- to 4-μm bound-abrasive diamond tools.

An overview of the mechanics and materials used in deterministic microgrinding has been presented previously at the structure/component level, involving length scales from 1 m to 1 mm, and at the process/materials level (1 mm to 1 nm).[7] The various chemomechanical interactions between abrasives and the glass surface can be categorized in terms of various length scales describing the response of the material to chemomechanical inputs.[8]

The bound-abrasive tools used in this work consist of single-crystal or polycrystal diamonds embedded in a bronze-type ring, typically 50 mm in diameter. The hardness of the tool is controlled using various amounts of binder material and by varying the processing conditions. Typically, several tools with decreasing abrasive sizes are used to create the desired surface profile and finish. Each tool is used to remove the damaged layer resulting from the previous tool and to further reduce the surface microroughness. The size of the diamond abrasives vary from about 100 μm down to 2 to 4 μm. Typical tool rotation rates for deterministic microgrinding of optical glasses range from 5,000 to 30,000 rpm, while the work rotation rates are from 50 to 300 rpm. Aqueous coolants are used to facilitate the mechanical and chemical actions of the bound-abrasive tools. The tool microstructure and performance have been discussed by Khodakov and Glukhov,[9] and the tool mechanical properties and microstructure, primarily porosity, have been investigated by Funkenbusch and coworkers at the University of Rochester.[10,11]

It is well known that microgrinding may entail either ductile or brittle material-removal mechanisms.[12–14] Either mode may become dominant depending upon mechanical factors, such as depth of cut,[15] or chemomechanical factors, such as coolant chemistry,[16,17] or abrasive size.[16–18] The brittle-to-ductile transition occurs under loose-abrasive microgrinding conditions of planar surfaces,[16,17] bound-abrasive microgrinding in plunge mode on planar surfaces[15,18] or aspheres,[14] and in single-point diamond turning of planar surfaces.[19]

At sufficiently low depths of cut, material removal occurs by plastic scratching. This mode is known as ductile or shear-mode grinding[20,21] and is characterized by low surface microroughness and subsurface damage, low material-removal rates, and high residual surface stresses.[17] In some cases the latter approaches the flow stress of glass in a thin surface layer.[22]

When the depth of cut is high or the abrasive size large, brittle material removal occurs and is characterized by high material-removal rates (proportional to the abrasive size[20,21,24–26]), considerably higher surface microroughness (proportional to the abrasive size[20,21,23]), a subsurface damage depth (generally proportional to the microroughness[27–30]), and lower levels of residual surface stress.[25–28]

One important aspect of deterministic microgrinding is that different glasses, microground under the same operating conditions, produce different amounts of surface microroughness and subsurface damage. This is not surprising since the mechanical properties of the glasses clearly affect their response to deterministic microgrinding. It has been shown that the mechanism for fine grinding using bound diamond tools de-

pends on the properties of the glass, as well as on the acidity of the grinding fluid, and the chemical and mechanical properties of the abrasive bond.[29] However, those studies did not actually correlate the observed grinding response with specific glass properties. That correlation had been performed using a brittleness index to characterize the response of glasses and ceramics under loose-abrasive grinding conditions.

In loose-abrasive grinding, surface roughness correlates with glass hardness,[31] whereas in deterministic microgrinding (where the infeed rate is specified), the elastic, plastic, and fracture properties of the work must all be used to predict microroughness. Under conditions where the nominal pressure is constant rather than the infeed rate, the average surface peak-to-valley microroughness (measured with a mechanical profilometer) was in the range of 2 to 20 μm for removal rates of 0.2 to 2.0 μm s^{-1}.[31] The abrasives, SiC or Al_2O_3, had sizes 150 μm or 22 μm, respectively. It was also shown that the surface microroughness was proportional to $E^{1/2}/H_v$, and the linear removal rate (μm s^{-1}) was proportional to $E^{5/4}/(K_c H_v^2)$, with E denoting the Young's modulus, K_c the fracture toughness, and H_v the Vickers microhardness. It was expected that the microroughness was proportional, if not identical, to the depth of the plastic zone on the glass surface, which, in turn, is determined by E and H_v when the surface is indented by a force of constant magnitude. It will be shown here that this model cannot be applied to deterministic microgrinding conditions where the infeed rate, rather than the nominal pressure, is specified.

To fully understand the interaction between the grinding tool and the optical surface in deterministic microgrinding, one must consider the effects of individual abrasive grains (or groups of grains) on the material-removal rate.[32] Such effects are governed by the chemomechanical properties of the glass, the bond matrix, and the abrasive grain, as well as by the process parameters, such as tool rotation rate and infeed rate. These effects are measured in terms of the resulting quality of the ground surface determined, for example, by the surface microroughness and subsurface damage.

To examine the correlation between mechanical properties and surface quality, a large set of glasses were ground under nominally identical operating conditions (i.e., tool and work rotation rates, infeed rate, tool diameter, and diamond concentration). In these microgrinding experiments, a sufficient amount of glass was removed so as to produce an optimal surface roughness. The mechanical properties of the various glasses spanned a relatively wide range and are summarized for some representative optical glasses. The correlation of surface microroughness to these glass mechanical properties for deterministic microgrinding is shown.

Experimental Procedure

1. Glass Properties

The chemical compositions of the glasses tested are shown in Table 66.I. The majority of the fused silica samples were Corning C7940.

Vickers hardness was measured by microindentation, with load application times of 15 s. The load was typically in the range of 2 to 1,000 gf (about 0.02–10 N). For each load, five indentations were made, and for each indentation the impression diagonals were measured three times. All glasses were measured in air. Figure 66.41 shows the dependence of the measured Vickers hardness on the applied load for some representative glasses, among which are fused silica, crown borosilicate, and flint glasses. Note that the flint glasses are relatively soft compared to the crown glasses and fused silica.

Table 66.I: The chemical compositions of the tested glasses (mol %). Both the Schott and Hoya glass designations are given. The majority of the fused silica samples were Corning C7940.

Glass (Schott)	Glass (Hoya)	SiO_2	B_2O_3	Al_2O_3	Na_2O	K_2O	CaO	BaO	PbO	Sb_2O_3	As_2O_3
Fused silica		100	–	–	–	–	–	–	–	–	–
F7	F7	44.75	–	–	2.4	5.7	–	–	46.85	–	0.3
SF7	FD7	33	–	–	–	5	–	–	62	–	–
SK7	BaCD7	39	15	5	–	–	–	41	–	–	–
BK7	BSC7	68.9	10.1	–	8.8	8.4	–	2.8	–	–	1
K7	C7	74	–	–	9	11	6	–	–	–	–
KzF6	SbF6	54	17.1	1.1	0.3	6	–	–	–	21	0.5

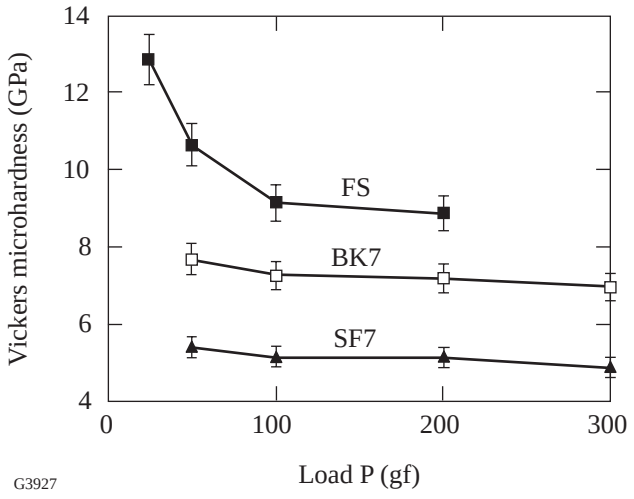

Figure 66.41
Load dependence of the Vickers microhardness for some optical glasses. FS is fused silica, BK7 is a crown borosilicate, and SF7 is a flint silicate glass. The hardness was measured at loads of 2, 5, 10, 25, 50, 100, 200, 500, and 1000 gf.

It is clear that the measured hardness increases at lower loads. This is a manifestation of the indentation size effect (ISE),[33] which can be described as

$$H_v = H_\infty\left(1+\frac{D_0}{D}\right), \tag{1}$$

where H_v is the measured hardness, H_∞ is the hardness at large loads, D_0 is a parameter describing the ISE, and D is the indentation diagonal. These parameters were extracted by plotting the measured H_v versus $(1/D)$. Table 66.II summarizes the curve-fitting results, where $D_{\min}$ and $D_{\max}$ are the smallest and largest indentation diagonals used in the fitting.

Figure 66.42 compares the measured Vickers hardness in the present work and in the work of Izumitani[34] to the published Knoop hardness. The two lines are parallel to each other. The offset at small Knoop hardness may be due to the fact that the junction offset in the Vickers indenter used (estimated at about 1 μm from atomic force microscopy of indentation shapes on soft materials such as ZnSe) may have been different from the one used in the work of Izumitani.[34]

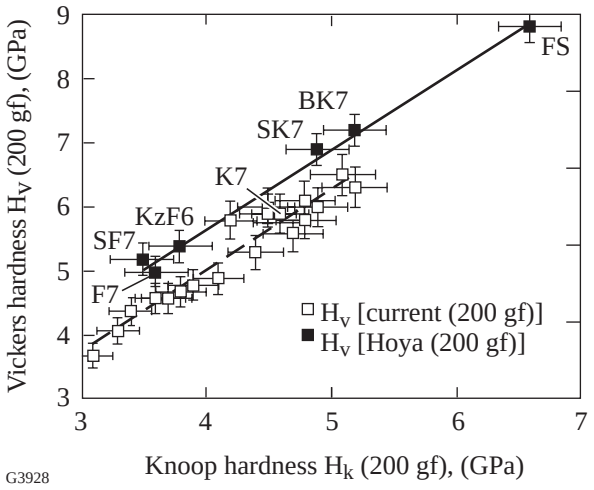

Figure 66.42
Comparison of measured Vickers microhardness with published values of the Knoop hardness from the Hoya and Schott glass catalogs. The open squares are the Vickers data from Izumitani.[34]

For fracture toughness measurements, the length c of cracks emanating from the indentation corners was measured. Typical data are shown in Fig. 66.43. For the glasses F7, SF7, and BK7, no cracks were observed for the three lowest loads used (2, 5, or 10 gf), but cracks were observed at 25 gf. For

Table 66.II: Parameters H_∞ and D_0 describing the indentation size effect (ISE) for the optical glasses used. The table shows also the range of indentation diagonal and Vickers hardness measured. The smaller diagonal corresponds to the higher hardness.

Glass	$D_{\min}$–$D_{\max}$ (μm)	$H_{\max}$–$H_{\min}$ (GPa)	H_∞ (GPa)	D_0 (μm)	R
BK7	11–51	7.7–6.9	6.7±0.1	1.6±0.2	0.975
SF7	13–61	5.4-4.8	4.7±0.1	1.9±0.3	0.945
F7	27–65	4.9–4.4	4.1±0.1	5.4±0.7	0.965
SK7	15–54	7.6–6.3	5.6±0.1	5.6±0.4	0.990
K7	11–57	7.8-5.6	4.7±0.1	6.8±0.5	0.988
KzF6	11–59	6.8–5.3	4.6±0.1	5.3±0.6	0.972
FS	6–21	12–8.8	6.9±0.3	5.1±0.6	0.994

K7, the loads for cracking were in excess of 50 gf, with no cracks for 25 gf or lower. For KzF6, the corresponding loads were 200 gf and 100 gf. These cracking thresholds indicate that KzF6 has the highest threshold load for cracking (the threshold being in the range 100 to 200 gf), K7 had the second highest threshold (between 25 and 50 gf), and the other glasses had threshold loads of about 25 gf.

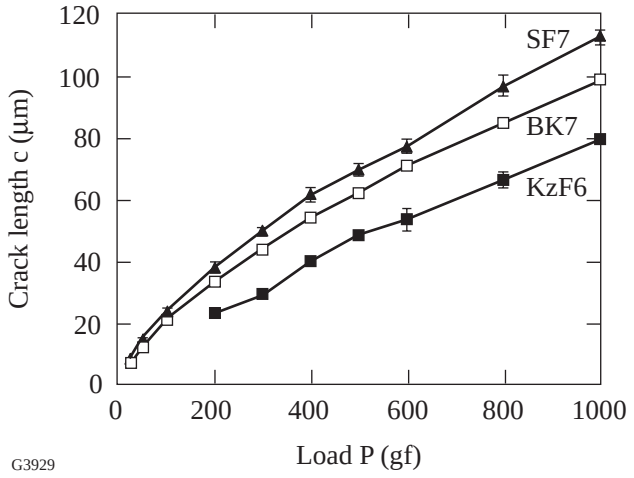

Figure 66.43
The dependence of the crack length c on the load P for typical optical glasses.

Two separate crack systems can arise from a Vickers microindentation.[35,36] Most ceramics with low fracture toughness exhibit half-penny cracks, also known as radial cracks. Brittle materials with small crack lengths, or, equivalently, materials with high fracture toughness, exhibit Palmqvist cracking. We observe that the measured total crack size $2c$ is the distance between crack tips on the surface trace of the radial crack.

The dependence of the measured crack length c on the applied load P exhibited both effects. The dependence $P \sim c^{3/2}$, which is usually assumed, was not exhibited; that relationship is based on the assumption of point loading a penny-shaped crack and is only valid when the crack size $c >>$ indentation half-size $D/2$. In our measurements on glasses and crystals (such as sapphire, KDP, and $LiNbO_3$), we had $c/(D/2)$ in the range 2.5 to 5.5. Indeed, the relation $P \sim c^{3/2}$ is obeyed only at large crack sizes, whereas at smaller crack sizes $P \sim c$. Thus, we used (see also Table 66.III)

$$c = \alpha P^{2/3} + \beta P . \tag{2}$$

Once the dependence of the crack size c on P has been measured, the fracture toughness K_c, a material property, can be calculated in a variety of ways.[37–44]

Table 66.III: Coefficients in correlating the measured crack size c to the applied load P according to the relation $c = \alpha P^{2/3} + \beta P$ for the six glasses tested.

Glass	α (μm $N^{-2/3}$)	β (μm N^{-1})	R
SF7	23.2±0.8	0.5±0.4	0.99965
F7	21.3±0.8	1.1±0.4	0.99954
BK7	21.2±0.5	0.06±0.25	0.99982
SK7	19.3±1	0.8±0.6	0.99912
K7	18.4±1	0.3±0.5	0.9989
KzF6	11.4±1.2	2.6±0.6	0.9982

The approaches of Niihara *et al.*[42] and Shetty *et al.*[43] assume surface cracks are Palmqvist type, whereas others assume the cracks to be fully developed radial cracks. Evans[38] used dimensional analysis and curve fitting over a range of $c/(D/2)$ from 1.5 to 7 and for many ceramic materials (B_4C, SiC, Si_3N_4, WC/Co, ZnS, ZnSe, PSZ ZrO_2). This model should be applicable to both Palmqvist and radial cracks, according to the following:

$$K_c = H\sqrt{D/2}\left(\frac{E}{H}\right)^{0.4} 10^{f(x)}, \qquad x = \log_{10}\left(\frac{c}{D/2}\right)$$

$$f(x) = -1.59 - 0.34\,x - 2.02\,x^2 \tag{3}$$

$$+11.23\,x^3 - 24.97\,x^4 + 16.32\,x^5 ,$$

where K_c is the fracture toughness, H is the hardness, D is the indentation diagonal, E is the Young's modulus, and c is the half-crack size. Lankford[41] included Al_2O_3, soda-lime silicate glass, and NaCl to the materials analyzed by Evans.[38] Anstis *et al.*[40] examined various glasses (glass-ceramic, soda-lime, aluminosilicate, lead alkali), polycrystal Al_2O_3 and sapphire, Si_3N_4, SiC, Ca-PSZ ZrO_2, Si, and SiC/Co. In the present work, $c/(D/2)$ ranges from about 2 to 3.8 and, therefore, should be described by Eqs. (3). For each indentation load P, diagonal D, and crack size c, we used the measured value of the Vickers hardness corresponding to that specific load. All models considered yielded the same relative ranking of the fracture toughness of these glasses.

Microindentation fracture toughness tests in toughened ZrO_2 (Ce-TZP), as well as bulk fracture toughness testing, were used to study this problem (bulk testing with the double

cantilever beam technique gave K_c = 10.2 MPa $m^{1/2}$).[45] By comparing the bulk test results with the microindentation test results, it was concluded that the analysis according to Palmqvist cracking was not very successful, that the Lankford[41] and Niihara[42] analyses overestimated the fracture toughness, and that the Evans[38] and Anstis *et al.*[40] approaches gave results most consistent with the bulk tests.

The extracted fracture toughness in Table 66.IV, which also includes other mechanical properties of glass, is summarized. The values in the table are averages over all crack lengths measured. The indicated errors correspond to the standard deviation over that range of crack lengths. Figure 66.44 shows the relation of the measured fracture toughness with the Knoop hardness (measured with a load of 200 gf), taken from the Schott Glass catalog.[46] It is seen that, in general, the silicate flint glasses (SF6, SF56, SF7, F7) are soft and brittle, whereas the silicate crown glasses (K7, BK7, SK7, fused silica) are harder and tougher. Note, however, that the antimony flint glass KzF6 has an exceptionally high toughness, as does the lanthanum borate glass LaK10. The effects of mechanical properties on surface microroughness will be discussed.

A literature survey was performed to confirm that the fracture toughness of some materials tested by microindentation has also been tested by other methods. For the borosilicate crown glass BK7, Wiederhorn *et al.*[50] measured a fracture toughness of 0.85±0.05 MPa $m^{1/2}$ at room temperature using double cantilever specimens. The fracture toughness of BK7 has been measured also in the range of 0.84 to 0.86 MPa $m^{1/2}$

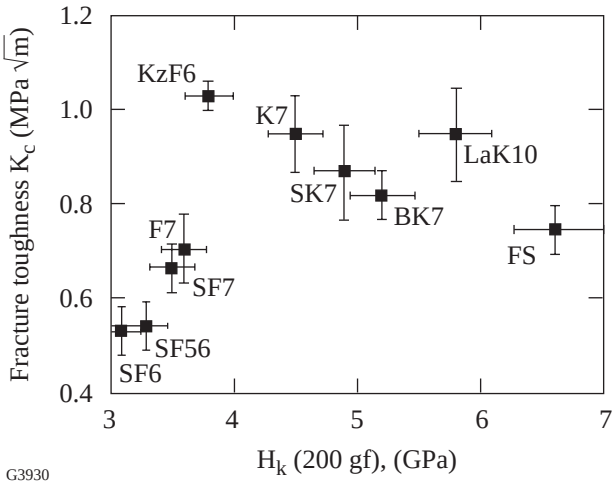

Figure 66.44
The correlation with Knoop hardness (from the Schott catalog[46]) of the measured microindentation fracture toughness K_c, extracted from $c(P)$ with the model of Evans.[38]

Table 66.IV: Mechanical properties of representative optical glasses. The microindentation data compare the extracted fracture toughness K_c (units of MPa $m^{1/2}$) based on the data of Cumbo,[47,48] Izumitani,[34] and the current work. All data have been reduced using the model of Evans.[38] Cumbo[47] used a load of 500 gf in air. Cumbo[48] used indenting loads of 50, 100, and 200 gf in anhydrous methanol. Izumitani[34] used 200 gf in air. The bulk measurements of SF6 used the Barker short-rod technique.[49] The bulk measurements of BK7 and fused silica were performed using the double cantilever method (DCB),[50] single-edge-notch, 3-pt. bending (SENB),[51] or strength method using a Knoop indent.[31]

	SF6	SF7	F7	BK7	SK7	K7	KzF6	FS
ρ (g cm^{-3})	5.18	3.80	3.62	2.51	3.51	2.53	2.54	2.20
T_g (°C)	426	448	437	557	643	513	444	1090
E (GPa)	56	56	55	81	84	69	52	73
H_k (200 gf) (GPa)	3.1	3.5	3.6	5.2	4.9	4.5	3.8	6.6
Cumbo[47] K_c	–	0.63±0.03	0.69±0.04	0.86±0.04	0.86±0.04	0.91±0.05	–	–
Cumbo[48] K_c	0.54±0.04	–	0.68±0.04	0.86±0.08	–	–	–	–
Izumitani[34] K_c	0.54	–	–	0.85	–	–	–	–
This work K_c	–	0.67±0.05	0.71±0.07	0.82±0.05	0.87±0.10	0.95±0.08	1.03±0.03	–
Bulk K_{Ic}	0.54	–	–	0.85±0.05	–	–	–	0.75±0.05

using the double cantilever method and three-point bending of edge-cracked specimens.[51] More recently, Buijs and Korpel-Van Houten[31] used a three-point bend test and Knoop indentation cracks to find 0.83±0.08 MPa $m^{1/2}$.

Our current measurements (see Table 66.IV) and the use of the Evans model[38] for the determination of fracture toughness gave 0.82±0.05 MPa $m^{1/2}$. Cumbo's microindentation measurements,[48] with loads in the range of 50 to 200 gf, when analyzed with the Evans model, gave a fracture toughness of BK7 0.86±0.08 MPa $m^{1/2}$ in anhydrous methanol. Cumbo's[47] older measurements in air, with a load of 500 gf, gave 0.86±0.04 MPa $m^{1/2}$ when analyzed with the Evans model.

We also note that Izumitani[34] used Vickers microindentation at a load of 200 gf and measured a crack size of c = 34.5 μm for BK7 in air. Although no measurement errors were reported, when these measurements are reduced with the Evans model, the microindentation fracture toughness for BK7 is extracted as 0.85 MPa $m^{1/2}$.

We conclude that microindentation fracture measurements in BK7 glass, when reduced according to the model by Evans,[38] give close agreement with the fracture toughness as measured by various bulk methods. Various microindentation measurements are also self-consistent in that all predict the same microindentation fracture toughness for BK7.

For the flint glass SF6, the bulk fracture toughness has been measured with Barker's short-rod technique in the work of Androsov *et al*.,[49] who used the Russian designation TF10 for that glass. In the short-rod technique, the fracture toughness was reported as 0.54 MPa $m^{1/2}$. More recently, Buijs and Korpel-Van Houten[31] used a three-point bend test and Knoop indentation cracks to find 0.54±0.05 MPa $m^{1/2}$.

Although we have not measured SF6 in this work, Cumbo did so in his Ph.D. thesis[48] using Vickers microindentation with loads of 50, 100, and 200 gf. We used the model by Evans[38] to reduce the microindentation measurements by Cumbo. The fracture toughness of SF6 is found to be 0.54± 0.04 MPa $m^{1/2}$, in excellent agreement with the bulk measurement of Androsov *et al.*[51]

We also note that Izumitani, in a Hoya technical report,[34] used Vickers microindentation at a load of 200 gf and measured a crack size c = 49.2 μm. When these measurements are reduced with the Evans model,[38] the microindentation fracture toughness is extracted as 0.54 MPa $m^{1/2}$. Again, it is concluded that microindentation fracture toughness measurements of SF6 are self-consistent, and they agree well with independent measurements of the bulk fracture toughness.

For fused silica, microindentation analysis overestimates the actual fracture toughness because fused silica is known to densify under compressive loads,[52,53] rather than flow by shear. Densification is facilitated by shear stresses.[54] Consequences of densification for optics manufacturing applications, such as polishing or grinding, are discussed by Lambropoulos *et al*.,[55] who also listed, from the literature, different glass types that are known to densify.

The bulk fracture toughness of fused silica has been measured by various techniques. For example, Wiederhorn[56] has measured 0.75 MPa $m^{1/2}$ with the double cantilever method, in agreement with the measurements by Wiederhorn *et al*.;[50] Barker[57] used a short-rod technique to measure 0.735±0.01 MPa $m^{1/2}$. The NBS work[51] used both double cantilever and edge cracked three-point bending techniques and measured 0.74 to 0.75±0.03 MPa $m^{1/2}$. Buijs and Korpel-Van Houten[31] used a three-point bend test and Knoop indentation cracks to find 0.70±0.07 MPa $m^{1/2}$. In the correlations to follow, we will therefore use 0.75 MPa $m^{1/2}$ for the fracture toughness of fused silica.

For other optical glasses, Izumitani in a Hoya technical report[34] used Vickers microindentation to measure the indentation diagonal and crack size for a large number of optical glasses, although these measurements were not converted to a fracture toughness. In that work, the crack length is defined as that portion of the crack trace extending beyond the end of the indentation diagonal (see also Izumitani,[13] p. 105, Fig. 4.32). For some glasses, the crack size was reported but not the indentation diagonal (see Izumitani,[13] p. 105, Fig. 4.31). Since these measurements are useful in correlating the glass mechanical properties with the surface quality, as described in the following sections, the model of Evans[38] was used to extract the fracture toughness of these glasses from the Izumitani measurements. The results are summarized in Table 66.V.

Microindentation is a convenient testing method for measuring the mechanical properties of glasses. For optical glasses not exhibiting densification, the fracture toughness from microindentation (determined by the measurement of the crack size at a fixed load) is in good agreement with bulk measurements. For densifying glasses, such as fused silica, microindentation overestimates the fracture toughness as measured by bulk methods.

Table 66.V: The extracted fracture toughness, according to the microindentation model by Evans,[38] for the optical glasses tested by Izumitani.[34] The data for the Young's moduli and Knoop hardness H_k (at 200 gf) are from the Schott Optical Glass catalog.[46] Parentheses ( ) in the E or H_k values show that the property was estimated from those of neighboring glasses. The Vickers hardness is extracted from the measurements of Izumitani[34] with a load of 200 gf. The ( ) in the H_v value indicate that the Vickers hardness was estimated from the correlation of H_v and H_k, similar to the one shown in Fig. 66.43, using the data from Izumitani.[34] The ( ) in the K_c entry denote that the estimated H_v for that glass was used. The bulk measurements of K_c for SF1 and UBK7 are from Wiederhorn and Roberts;[51] for F2 from Buijs and Korpel-Van Houten;[31] for SF6 from Buijs and Korpel-Van Houten[31] and Androsov.[49] The uniaxial yield stress σ_Y was estimated using the model of Hill[58] (see Appendix).

Glass (Schott)	E (GPa)	H_k (GPa)	H_v (GPa)	K_c (MPa $\sqrt{m}$)	K_c (MPa $\sqrt{m}$) (bulk)	σ_Y (GPa)
F2	58	3.7	4.6	0.61	0.55±0.06	1.9
F4	55	3.6	4.6	0.65		2.0
F5	58	3.8	4.7	0.63		2.0
SF1	56	3.4	(4.3)	–	0.63±0.09	2.1
SF4	56	3.3	4.1	0.55		1.7
SF5	56	3.4	4.4	0.57		1.8
SF6	56	3.1	3.7	0.54	0.54	1.4
SK3	83	4.8	6.1	0.77		2.5
SK11	79	5.1	6.5	0.78		2.8
SK15	84	4.5	6.0	0.79		2.4
SK16	89	4.9	6.0	0.78		2.3
BK1	74	4.8	5.8	0.82		2.5
UBK7	81	5.0	(6.2)	–	0.89±0.01	2.6
K3	71	4.7	5.6	0.79		2.4
K9	(67)	(4.4)	5.3	0.76		2.3
KF4	(66)	(4.1)	4.9	0.76		2.0
LF6	60	3.9	4.8	0.72		2.0
LaF2	93	4.8	(6.0)	(0.94)		2.3
LaF3	95	5.1	(6.3)	(0.93)		2.4
LaK10	111	5.8	(7.2)	(0.95)		2.7
LaK11	90	5.2	(6.5)	(0.83)		2.5
BaK2	71	4.5	(5.6)	(0.72)		2.4
BaF3	64	4.2	(5.2)	(0.67)		2.2
BaF10	78	(4.8)	5.8	0.67		2.3
BaSF2	66	4.1	(5.1)	(0.44)		2.1
BaSF8	74	(4.2)	5.8	0.67		2.1
SSK1	79	4.5	5.9	0.75		2.4
SSK5	(79)	(4.6)	5.9	0.70		2.4

2. Deterministic Microgrinding

All samples subjected to deterministic microgrinding were nominally prepared under the same conditions. Typically, the final 2- to 4-μm tool was run at 15,000 rpm, with a work speed of 180 rpm, an infeed rate of 6 μm min^{-1}, a total material removal of 12 μm, and a dwell time after infeed of 15 s. Occasionally, these parameters were altered slightly to achieve the least possible roughness for a given glass. The most common cutting parameter changed was the total amount of glass removed with the 2- to 4-μm tool. This could be as low as 5 μm for some materials, depending on the residual damage depth from the previous tool. Occasionally, tool rpm was reduced or dwell time was increased. Tools were trued and dressed before each microgrinding cut.

3. Tool Property Characterization

Various-hardness tools were used[59] but all tools had a 75 concentration of 2- to 4-μm diamonds (18.8 vol %) and a Young's modulus of 100 to 120 GPa. The aqueous coolant used is commercially available as Challenge 300 HT and has pH = 9.5.

Bond properties for bound-abrasive tools are generally described in terms of the bond "hardness." The tools used in this study were bronze bonds with bond hardnesses designated as *L* (softer), *N* (medium), and *T* (harder). Bond hardness is an alphabetical scale with the hardness increasing for designators from *A* (soft) to *Z* (hard). Unfortunately, there is no universal scale for this designation, nor even good agreement on what specific property constitutes a bond's hardness. We have, therefore, used simple mechanical tests to characterize bond properties: the ultrasonic wave speed and Vickers microhardness.

When an ultrasonic wave traverses a solid, its speed (v) is determined by the modulus (M) and density (ρ) of the material in accordance with

$$v = \sqrt{\frac{M}{\rho}}. \tag{4}$$

The particular modulus M measured (Young's modulus, shear modulus, etc.) depends on the type of wave and some geometrical details of the testing procedure. For an isotropic material with only two independent elastic constants, measurement of both *P*-wave (compression) and *S*-wave (shear) speeds allows both constants to be determined. Therefore, if the wave speed and the density of a tool material are determined, a quantitative measure of its elastic stiffness can be obtained.

In the current experiments, the density could not be measured nondestructively since the bond material was permanently fused to the stainless steel rings during the fabrication process. Therefore, the wave speeds were used as indicators of elastic stiffness, with the assumption that the tool densities are all similar. This is reasonable since the bonds were all bronze based and had identical diamond concentrations. The relatively small differences in the observed wave speeds (see Fig. 66.45) are therefore indicative of relatively small differences in elastic stiffness among the different designation tools.

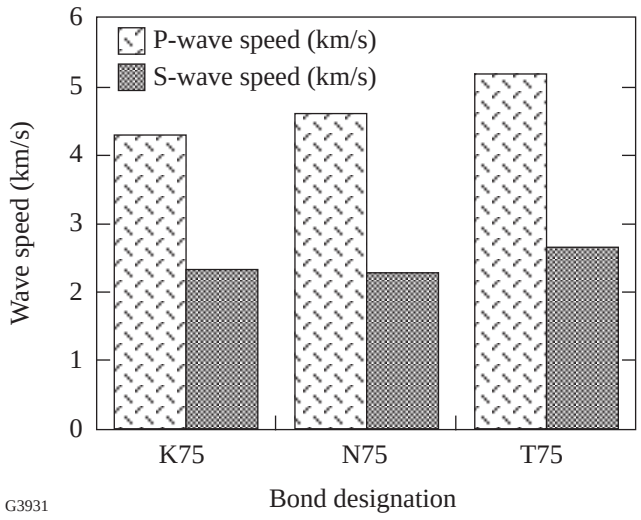

Figure 66.45
Measured ultrasonic wave speeds for different bond-hardness designations.

Vickers microhardness was also measured on the tools, using a 200-gf load. A much stronger trend in the data is obtained in this case (Fig. 66.46), with the *T* bond microhardness being approximately double that of a *K* bond. The *L* bond was not measured but should be between that of the *K* and *N* bonds. Considerable variation can occur among individual microhardness test results as a consequence of the locally inhomogeneous nature of the bond. The reported values are therefore averages of at least five separate indentations. Standard deviations for these measurements were of the order of 0.1 to 0.2 GPa.

4. Surface Roughness (SR) and Subsurface Damage (SSD)

The surface microroughness was interferometrically measured with a Zygo Maxim (MX) or Zygo New View 100 (NV) interferometer. The Zygo New View 100 is a three-dimensional imaging surface-structure analyzer. It uses coherence-scanning white-light interferometry for noncontact imaging and measurement of surface microstructure and topography.

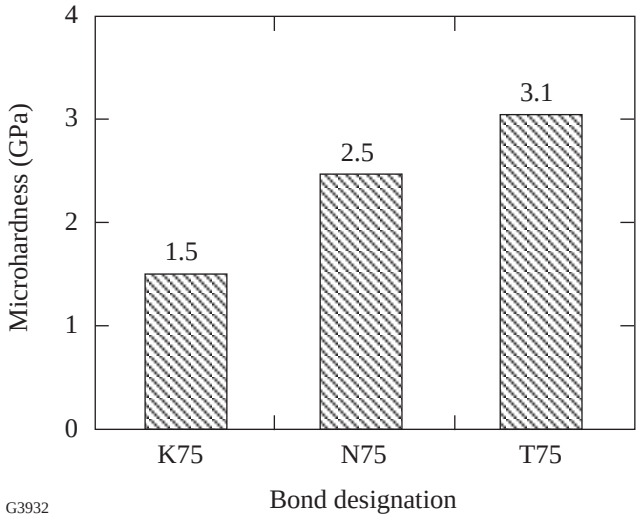

Figure 66.46
Measured Vickers microhardness for different bond-hardness designations.

The Zygo Maxim uses the same interferometric principles but has a laser as a light source and does not scan vertically. Because of these differences, this device cannot measure absolute surface roughness on components with defects exceeding about 0.5 μm. The rms surface roughness values reported for microground surfaces are substantially lower than the actual roughness, but are qualitatively reliable.

For each glass, 12 to 15 optical surfaces, prepared under the same microgrinding conditions, were used for the surface-roughness determination with the Zygo Maxim interferometer. The roughness of a smaller set of glasses (nine samples per glass type) was also measured with the New View 100 interferometer.

Following microgrinding, the subsurface damage (SSD) was determined by first etching the samples in HF for 30 s to reveal the structure below the surface. Damage depth is measured by a dimpling technique, described by Lindquist *et al.*,[60] in which a steel ball of 23.81-mm radius is used with an abrasive to polish a dimple in the etched region. SSD is extracted by optically measuring the inner and outer radii containing the damaged layer. For a given steel ball radius, these measurements provide the depth that damage extends below the surface. Zhou *et al.*[61] have shown that optical measurement of SSD is in good agreement with SEM measurements for a variety of etching solutions and durations. The subsurface damage was measured in two different samples prepared under nominally identical microgrinding conditions.

The measured surface microroughness (from the Maxim interferometer) is plotted in Fig. 66.47 versus the subsurface damage measured by dimpling. It is seen that, generally, the subsurface damage increases with surface roughness. Similar observations were originally made by Aleinikov[27] for loose abrasive grinding of glasses and ceramics. Aleinikov used a profilograph to measure peak-to-valley surface roughness in the 35- to 65-μm range for glasses, and subsurface damage in the 150- to 260-μm range. The abrasive used was SiC of about 100 to 150 μm in size. The ratio of roughness to subsurface damage was found to be 4 to 4.2 for the tested optical glasses.

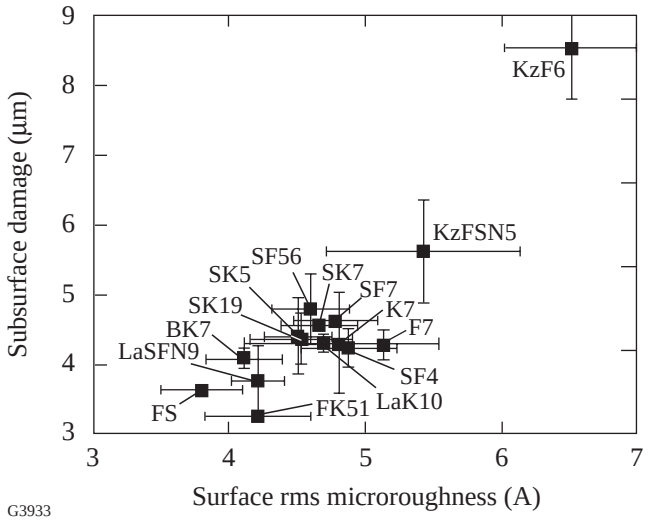

Figure 66.47
Comparison of the measured subsurface damage and the surface roughness (measured with the Zygo Maxim interferometer). For each glass, about 12 different samples were used for the roughness and two samples for the subsurface damage measurements.

Edwards and Hed[30] investigated the relationship between surface roughness and subsurface-damage depth for bound-diamond-abrasive tools (diamond size 60 to 220 μm), identifying both fracture and plastic scratching as the material-removal mechanisms. This is in contrast to the work on loose-abrasive lapping,[27] where material removal occurred only by fracture. For BK7 and zerodur, Edwards and Hed[30] found peak-to-valley surface roughness (measured with a stylus profiler) of 1.2 to 8 μm and subsurface damage depth (measured with a taper polishing method) in the range 15 to 42 μm. For conditions with fracture as the principal material-removal mechanism, they found the ratio of subsurface-damage depth to peak-to-valley surface roughness as 6.4±1.3.

That work also examined the review work of Khodakov *et al*.[28] (unspecified glasses and grinding conditions) on bound diamond tools and estimated a ratio of subsurface damage to roughness of 5.5±1.1 for diamond particles 6.5 to 40 μm in size.

Correlations

In this section we discuss some correlations between the measured surface rms microroughness (SR) and the material properties of the glasses tested. The surface roughness data are those obtained from components ground with the N75 (medium bond hardness) tool with 2- to 4-μm diamonds and measured with the Maxim interferometer. For the correlations we use Knoop hardness, as it is conveniently tabulated in manufacturers' product catalogs.[46]

Figure 66.48 shows the correlation of measured surface roughness (SR) with the Knoop hardness H_k (measured at 200 gf) from the Schott Glass catalog.[46] This figure shows that, with the hardness as the correlating mechanical property, surface roughness increases with hardness for the flint glasses (SF6, SF56, SF7, F7, KzF6) but decreases with H_k for the silicate crown glasses (K7, BK7, SK7, fused silica). This result shows that H_k alone does not determine SR. For example, KzF6 has about the same Knoop hardness as the other flint glasses but shows a significantly higher surface microroughness.

The surface roughness should not correlate with Knoop hardness under conditions of deterministic microgrinding for the following reason: For a fixed infeed rate, different glasses require different forces on the tool against the glass surface. Since the force varies from glass to glass, Knoop hardness can not conveniently be normalized to give dimensions of length (the dimensions of SR). This obstacle is overcome when the fracture toughness is used in conjunction with the Knoop hardness, as shown below.

Figure 66.49 shows the correlation of the measured SR with the length scale $(K_c/H_k)^2$. An essentially linear relationship between the surface microroughness and $(K_c/H_k)^2$ holds for both the flint and crown silicate glasses, as well as the lanthanum borate glass LaK10. Although not shown here, the correlation previously shown to hold for loose-abrasive grinding,[31] namely that SR ~ $E^{1/2}/H$, does not correlate with our experimental data. The reason, of course, is that under conditions of deterministic microgrinding, the material-removal rate, rather than the nominal pressure, is held constant as in loose-abrasive grinding.

The length scale $(K_c/H_k)^2$ may be referred to as a ductility index Ξ (with units of length),

$$\Xi = \left(\frac{K_c}{H_k}\right)^2 , \tag{5}$$

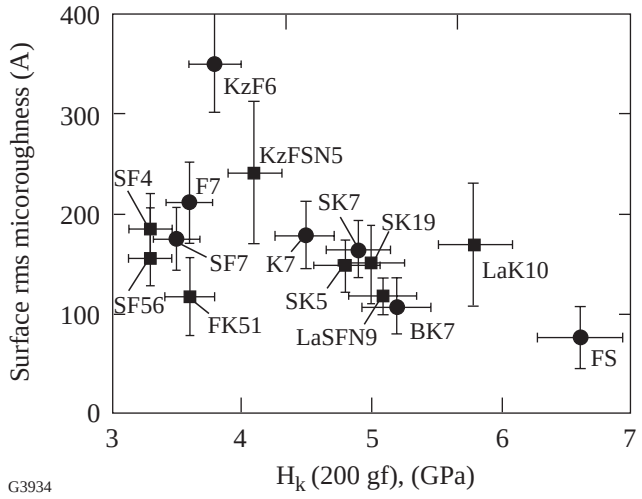

Figure 66.48
Correlation of measured surface roughness (with Zygo Maxim interferometer) with the Knoop hardness published in the Schott glass catalog. For flint silicate glasses SR increases with H_k, while it decreases for the crown silicate optical glasses.

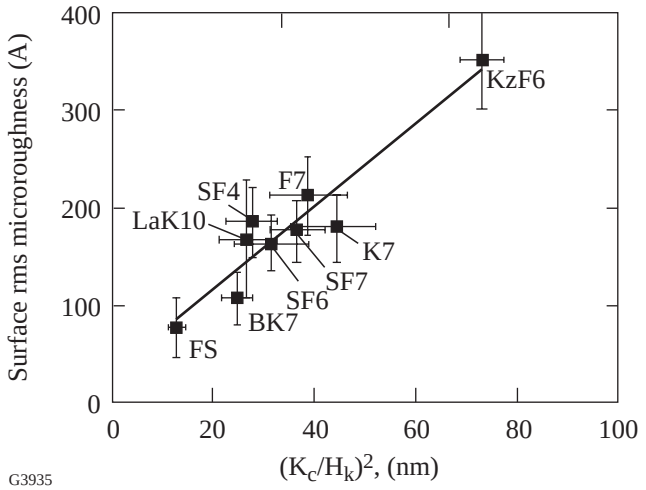

Figure 66.49
Correlation of measured surface roughness (with Zygo Maxim interferometer) with the ductility index $\Xi = \left(K_c/H_k\right)^2$ of various optical glasses. The correlation holds for both flint and crown glasses, as well as fused silica. The straight line, with slope 4.2±0.5 A/nm, has correlation $R = 0.95$.

which is in reverse analogy to the brittleness index used by Lawn *et al*.[62] In that investigation the surface energy Γ was used, but their results may be recast into a form similar to ours with the identification of Γ as the energy-release rate required for crack growth, i.e., $\Gamma = \left(1-\nu^2\right)K_c{}^2/E$ under plane-strain crack-growth conditions, where ν is the Poisson ratio. The ductility index $(K_c/H_k)^2$ provides a useful measure of the response of various glasses; for example: although fused silica has a typical fracture toughness K_c, it has a very high hardness, a low ductility index, and a low measured surface roughness. On the other hand, KzF6 has a high fracture toughness and low hardness, leading to a high ductility index and a correspondingly high surface roughness.

The concept of quantifying the "grindability" of brittle materials in terms of a brittleness index was first introduced by Aleinikov[27] in his seminal work that defined the brittleness index as linearly related to $(\ell/D)^2$, where D is the indentation diagonal in a Vickers microindentation test and ℓ the resulting crack size. Aleinikov used a fixed indentation load of 50 gf, but it is unclear whether the crack size ℓ used is the same as that defined in this work. Crack size may be measured from the center of the indentation or the length of the crack extending beyond the corner of the indentation, i.e., $\ell = c - D/2$ in our notation. In any case, $(\ell/D)^2$ is a function of the applied load P [typically $(\ell/D)^2 \sim P^{1/3}$], which is inversely proportional to the fracture toughness K_c, and proportional to the Young's modulus E. This implies that the brittleness index defined by Aleinikov can vary depending on whether the applied load is large, rather than being a load-independent material property, such as the ductility index.

Early Russian investigations in loose-abrasive grinding show that the fracture toughness, or the crack size ℓ, must be used to characterize material removal. Aleinikov's work on lapping[27] showed that the volume removal rate was proportional to ℓ^3, whereas the subsurface damage depth (the "destroyed layer" in Aleinikov's work) was proportional to ℓ. It is interesting to note that in the work on lapping by Izumitani, the volume removal rate was proportional to ℓ^2.[34,63]

It is instructive to interpret in a different way our conclusion that the measured SR scales in direct proportion to the ductility index $(K_c/H_k)^2$. We used Hill's[58] model to extract the uniaxial yield stress σ_Y of glass (see Fig. 66.50) from the measured Vickers hardness H_v. The procedure is summarized in the Appendix. In Fig. 66.50 the extracted uniaxial yield stress σ_Y is plotted versus the measured Vickers hardness, including our current measurements and those by Izumitani.[34] The values of the uniaxial yield stress σ_Y are also shown in Table 66.V.

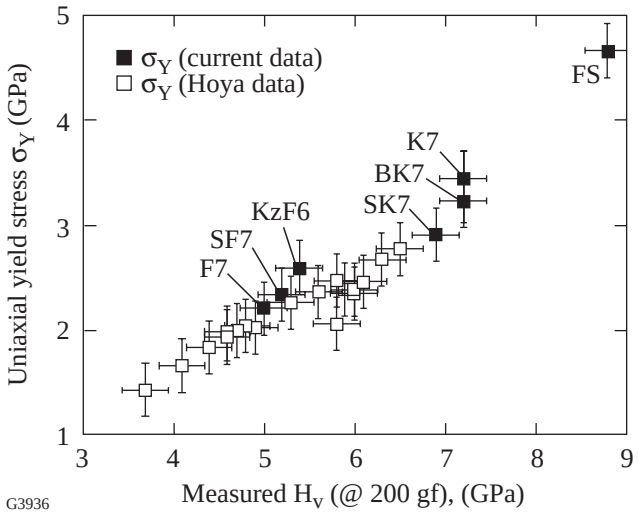

Figure 66.50
The correlation of the measured Vickers hardness (the open squares are from Izumitani[34]) with the uniaxial yield stress as calculated from the Hill analysis.[58]

The size of the plastic zone in a mode-*I* growing crack tip may be estimated from the extracted uniaxial yield stress σ_Y and the fracture toughness K_c. For an elastic, perfectly plastic material (i.e., no strain hardening), the total height of the plastic zone is[64]

$$R_p \approx 2\,\frac{0.35}{\pi}\left(\frac{K_c}{\sigma_Y}\right)^2. \tag{6}$$

Figure 66.51 shows that the measured surface microroughness is about equal to the size R_p of the plastic zone. Based on this correlation, we can therefore predict the surface microroughness as

$$\mathrm{SR} \sim R_p \approx 2\,\frac{0.35}{\pi}\left(\frac{K_c}{\sigma_Y}\right)^2, \tag{7}$$

where the symbol ~ denotes "varies as." We emphasize that the numerical agreement between the extent of the plastic zone R_p and the rms surface roughness (SR) determined with the Maxim interferometer is fortuitous because the Maxim interferometer provides only a qualitative measure of the surface

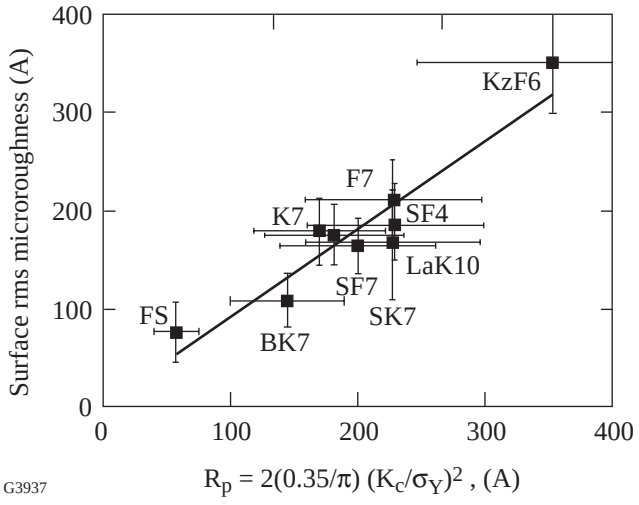

Figure 66.51
Correlation of measured surface roughness (with Zygo Maxim interferometer) with the total height R_p of the plastic zone in a crack tip growing under mode *I* (opening) conditions. The straight line fit has correlation $R = 0.95$.

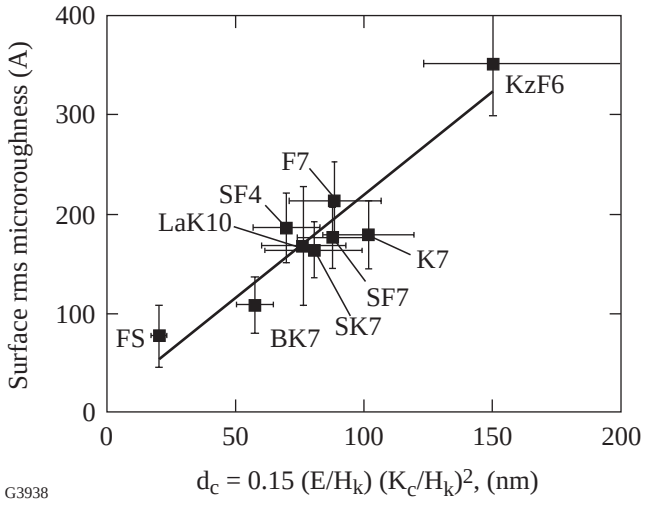

Figure 66.52
Correlation of measured surface roughness (with Zygo Maxim interferometer) with the critical depth of cut d_c, from the work of Bifano *et al.*[15] The straight line, with slope 2.1±0.3 A/nm, has correlation $R = 0.94$.

roughness. In any case, the size of the plastic zone at a growing crack tip is proportional to $(K_c/H_k)^2$, which was previously identified as the ductility index. The issue of the precise correlation between SR and the ductility index $(K_c/H_k)^2$ will be further examined in the next section where we discuss the surface roughness resulting from different tools.

In addition to the ductility index $(K_c/H_k)^2$ it is possible to use other material-dependent properties in correlating the surface microroughness among various glasses. Figure 66.52 shows the correlation between the measured SR and the critical depth of cut d_c, defined by Bifano *et al.*[15] as that material length scale distinguishing the transition from ductile- to brittle-material-removal mechanisms. It is surprising, however, that our measured SR increases with d_c. It is expected that, for a material with a low d_c, brittle removal should occur when the infeed per tool revolution exceeds d_c and, hence, yield higher surface roughness. The good correlation between SR and d_c in Fig. 66.52 may be due to the fact that the ratio E/H_k, for the materials in Figs. 66.50 and 66.51, varies only between 14 and 19 (with the exception of fused silica, for which $E/H_k = 11.1$). Thus, the correlation in Fig. 66.52 may be a result of the correlation shown in Fig. 66.49.

We have also considered the correlation between the measured surface roughness and the critical load P_c required for the formation of subsurface lateral cracks, as discussed by Chiang *et al.*[65,66] The correlation now becomes less effective, which may be due to the fact that in deterministic microgrinding the infeed rate is constant, and the contact force between the tool and the glass surface spontaneously adjusts itself to accommodate the imposed material-removal rate.

Relationship to Tool Hardness

To determine whether the correlations with glass properties are retained for different tools, experiments were performed with *L*, *N*, and *T* hardness tools. All tools had approximately the same Young's modulus, but Vickers hardness increased approximately linearly from softer (*L*) to harder (*T*) tools. All tools had 75 concentration (18.8 vol %) of 2- to 4-μm diamonds. The glasses studied in this section included the flint glasses SF7, F7, and KzFSN5, the crown glasses K7 and SK7, as well as fused silica. The rms surface microroughness was measured with the New View 100 white light interferometer.

Figure 66.53 shows the correlation of the measured SR with the Knoop hardness for the three tools. As in Fig. 66.48, different glass groups behave differently: Surface roughness increases with hardness for the flint glasses, but decreases for the crown silicate glasses.

Figure 66.54 shows the improved correlation of the rms microroughness with the ductility index $(K_c/H_k)^2$. The ductility index can be used as a single material length scale correlating the SR with the material properties of the various glasses. This conclusion emphasizes (1) the importance of fracture and

deformation in the production of SR in deterministic microgrinding and (2) the similar behavior of various glass families (flints, crowns, fused silica). We emphasize that in loose-abrasive microgrinding (lapping), the surface microroughness is determined only by the hardness and the elastic modulus of the glass,[31] and not by the fracture toughness. That the microroughness correlates differently with the mechanical properties of glass for deterministic microgrinding and loose-abrasive microgrinding emphasizes the differences between two-body and three-body abrasive processes.

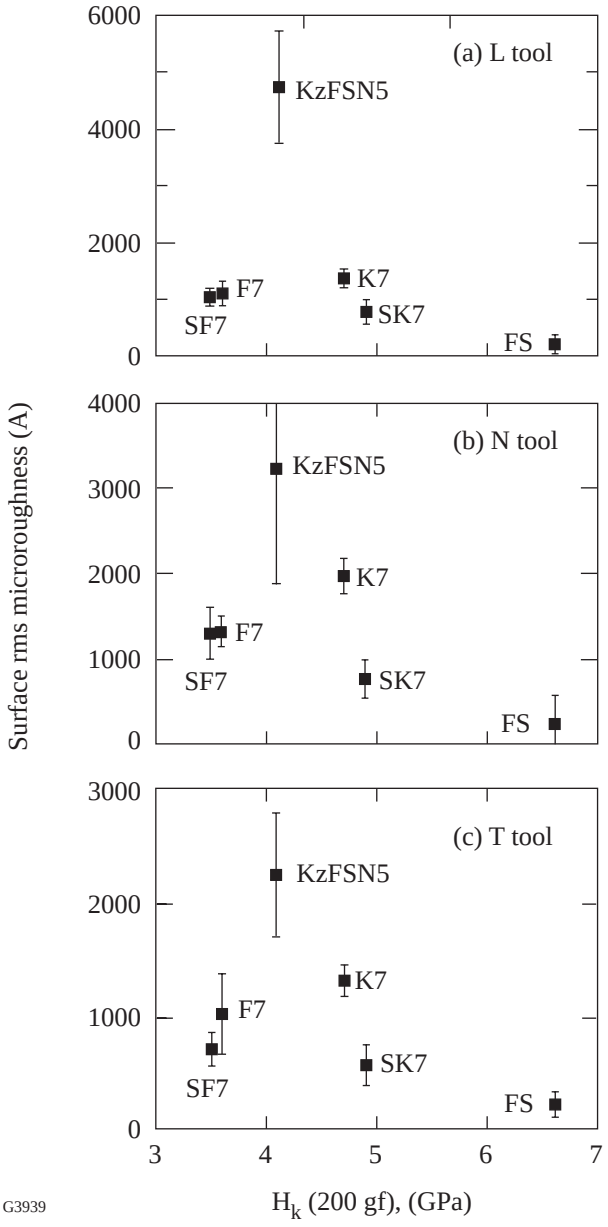

Figure 66.53
Correlation of measured surface roughness (with Zygo New View NV interferometer) with the Knoop hardness of optical glasses for (a) softer (*L*) tools, (b) medium (*N*) tools, and (c) harder (*T*) tools.

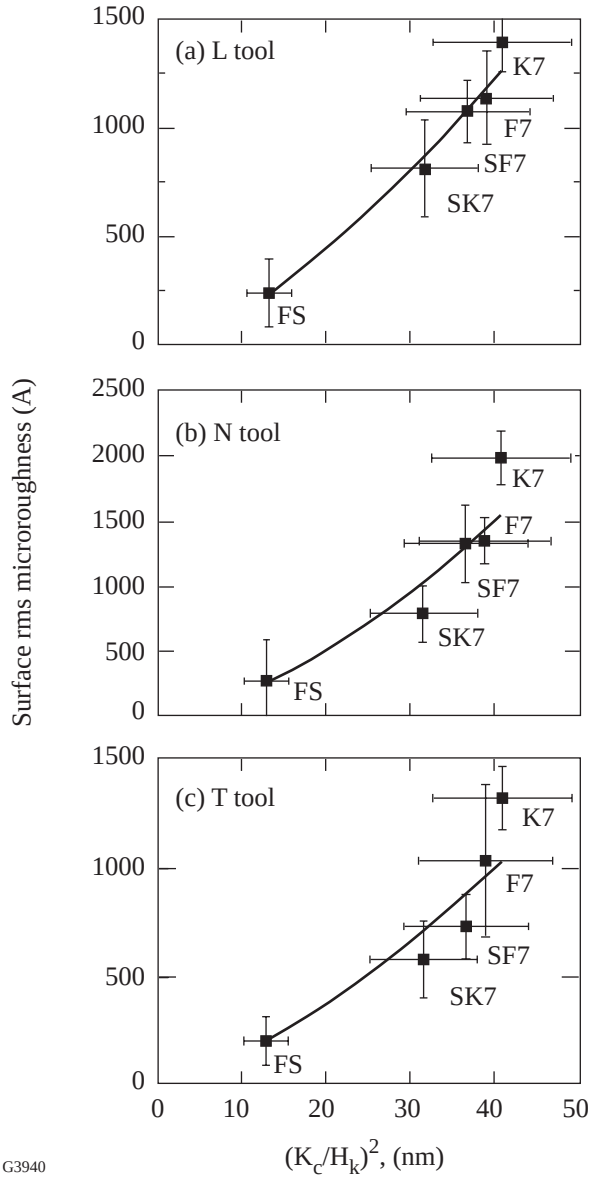

Figure 66.54
Correlation of measured surface roughness (with Zygo New View NV interferometer) with the ductility index $\Xi = (K_c/H_k)^2$ for various optical glasses for (a) softer (*L*) tools, (b) medium (*N*) tools, and (c) harder (*T*) tools. Power law fitting gives an exponent of 1.5±0.1 for the dependence of SR on Ξ, with correlation R = 0.92–0.99.

The results in Fig. 66.54 [the measurement of the rms roughness by the New View 100 white-light interferometer (NV)] are consistent with the measurement of the roughness with the Maxim laser interferometer (MX), shown in Fig. 66.49. When the surface roughness of Fig. 66.54 is fitted to a power-law dependence on the ductility index $\Xi = (K_c/H_k)^2$, we find

$$\text{rms SR (NV)} \sim \Xi^m . \tag{8}$$

The exponent $m = 1.5 \pm 0.1$, with confidence levels of 0.92–0.99 for the three bond hardnesses *L*, *N*, and *T*. On the other hand, when the surface-roughness measurements by the two different interferometers were correlated (by power-law curve fitting), we found

$$\text{rms SR (MX)} \sim [\text{rms SR (NV)}]^n , \tag{9}$$

where the exponent $n = 0.62 \pm 0.15$. The large relative error in the exponent *n* is due to the larger variation between the two sets of measurements for the rougher surfaces.

Combining Eqs. (8) and (9), we conclude that

$$\text{rms SR (MX)} \sim \Xi^{mn} . \tag{10}$$

Since the product (*mn*) is 0.93 ± 0.27, we conclude that Eq. (10) predicts essentially a linear dependence of the surface roughness measured with the Maxim laser interferometer and the ductility index Ξ. This result is consistent with the independently measured behavior shown in Fig. 66.49.

Conclusions

We have shown that the elastic (Young's modulus), plastic (hardness), and fracture (fracture toughness) properties of glasses must all be considered in correlating the glass mechanical properties with the surface quality resulting from deterministic microgrinding using bound-abrasive tools under specified infeed rate (or material-removal rate) and when the processing parameters (relative speed, diamond size, coolant) are constant.

The material properties can be conveniently grouped into a ductility index $\Xi = (K_c/H_k)^2$, with the units of length, and proportional to the size of the plastic zone near the crack tip of a crack growing under mode *I* (i.e., opening) conditions. The ductility index was shown to correlate surface roughness with glass mechanical properties across glass groups such as flint, crown silicate, and fused silica. The correlation also holds for softer, medium, or harder bond tools, or when the surface microroughness is measured by different interferometric methods. The creation of surface roughness is seen as a competition between fracture and flow processes. Low ductility, achieved by a low fracture toughness or a high hardness, results in low resulting roughness.

The correlation of the surface roughness to glass properties under deterministic microgrinding conditions is distinct from the correlation under loose-abrasive (lapping) conditions, where the surface roughness is determined by the elastic and plastic properties of glass. Such a distinction is not surprising: Deterministic microgrinding proceeds under a specified infeed rate (i.e., material-removal rate), whereas lapping is under constant nominal pressure. Furthermore, lapping is a three-body abrasive process, whereas deterministic microgrinding is primarily a two-body abrasive process (although three-body abrasion can occur when a previously bound diamond abrasive grain is separated from the retaining bond matrix).

We have shown that the fracture toughness of optical glasses can be conveniently measured using Vickers microindentation. Such measurement of the near-surface glass mechanical properties is advantageous in that many measurements can be done on a single specimen. However, for glasses that show densification, such as fused silica, microindentation provides an overestimate of the fracture toughness. For glasses that deform by flow, as do most optical glasses containing network modifiers, microindentation fracture-toughness measurements are in good agreement with the fracture toughness measured by bulk methods.

We have assumed that the mechanical response of glasses may be described in terms of four fundamental properties: the elastic Young's modulus *E*, the Poisson ratio *ν*, the plastic hardness *H* (Vickers H_v or Knoop H_k), and the fracture toughness K_c. This set of properties may be incomplete. Future work should consider the following: hardening effects describing the increase of the flow stress with continuing deformation, effects correlating the rate of subcritical crack growth to applied loads or stress-intensity factors,[44,51,64] any chemomechanical effects on the glass properties, such as the effect of slurry chemistry,[17] or the possibility that the glass mechanical properties at very small depths (say, less than 0.1 μm) may be different from the measured properties either at deeper penetrations or by bulk methods. Of course, characterization at such low depths requires sophisticated experi-

mental techniques, such as nanoindentation. Also, subcritical crack growth is very sensitive to the chemical environment within which crack growth occurs. We are currently investigating the effects of various coolants on various glass mechanical properties.

This article concentrates on correlating the glass mechanical properties with surface features such as microroughness and subsurface damage for a variety of optical glasses, all finished under the same deterministic microgrinding process parameters. Of course, from the optics manufacturing perspective, an important complementary issue is the combination of process parameters, such as infeed rate, tool relative speed, coolant, etc., which, for a given optical glass, may be used to predict the resulting surface microroughness or other surface features. We are investigating the construction of optics manufacturing maps for deterministic microgrinding processes and are hopeful these will allow the accurate prediction of the surface features resulting from a given combination of process parameters and material properties.

ACKNOWLEDGMENT

We acknowledge insightful discussions with Professors David Quesnel and Stephen J. Burns, and Mr. Y.Y. Zhou from the Department of Mechanical Engineering, and with Mr. Arne Lindquist from the Center for Optics Manufacturing at the University of Rochester. Funding was provided by the Center for Optics Manufacturing and by the National Science Foundation under Grant No. MSS-8857096.

Appendix: Hill's Extraction of Uniaxial Yield Stress from the Hardness

The model of Hill[58] examines a spherical cavity in an infinite solid. The cavity, originally of vanishing radius, is under internal pressure p, so that its current radius is a. The boundary between the plastic and elastic zones is at $r = b$, r being the spherical distance from the cavity center. The material outside the cavity is elastic, perfectly plastic with Young's modulus E, Poisson ratio ν, and uniaxial stress (in tension or compression) σ_Y.

The requirement of equilibrium and radial traction continuity across the elastic-plastic boundary $r = b$ yields

$$p = \frac{2}{3}\left[1 + 3\,\ln\left(\frac{b}{a}\right)\right]\sigma_Y . \tag{A-1}$$

Calculation of the elastic strains allows the determination of the (finite) radial displacements, yielding

$$\left(\frac{b}{a}\right)^3 = \frac{E}{3(1-\nu)\sigma_Y} . \tag{A-2}$$

In the Hill model of indentation Vickers hardness, the pressure p required to produce the radius a is identified with the average pressure under the indenter, i.e., the hardness. Thus

$$p \to H_v . \tag{A-3}$$

Equations (A-1)–(A-3) and elimination of the ratio b/a allow the correlation of the Vickers hardness H_v and the uniaxial yield stress σ_Y, which is found from solving the transcendental equation

$$\frac{\left(E/H_v\right)}{3(1-\nu)}\frac{1}{\left(\frac{\sigma_Y}{H_v}\right)} = \exp\left[-1 + \frac{3/2}{\left(\frac{\sigma_Y}{H_v}\right)}\right] \tag{A-4}$$

for the ratio σ_Y/H_v, in terms of measurable mechanical properties such as the Young's modulus, the Vickers microhardness, and the Poisson ratio.

REFERENCES

1. H. M. Pollicove and D. T. Moore, Laser Focus World, March 1991, 145.
2. H. M. Pollicove and D. T. Moore, in *Optical Fabrication and Testing Workshop Topical Meeting*, 1992 Technical Digest Series (Optical Society of America, Washington, DC, 1992), Vol. 24, pp. 44–47.
3. D. Golini and W. Czajkowski, Laser Focus World, July 1992, 146.
4. D. Golini, A. Lindquist, M. Atwood, and C. Ferreira, in *Optical Fabrication and Testing Workshop*, 1994 Technical Digest Series (Optical Society of America, Washington, DC, 1994), Vol. 13, pp. 28–31.
5. H. Pollicove, D. Golini, and J. Ruckman, Opt. Photonics News, June 1994, 15.
6. J. Liedes, in *Current Developments in Optical Design and Optical Engineering II*, edited by R. E. Fischer and W. J. Smith (SPIE, Bellingham, WA, 1992), Vol. 1752, pp. 153–157.
7. J. C. Lambropoulos, P. D. Funkenbusch, D. J. Quesnel, S. M. Gracewski, and R. F. Gans, in *Proceedings of the Ninth Annual Meeting of the American Society for Precision Engineering* (American Society for Precision Engineering, Raleigh, NC, 1994), pp. 370–373.
8. J. C. Lambropoulos, in *Proceedings of the Ninth Annual Meeting of the American Society for Precision Engineering* (American Society for Precision Engineering, Raleigh, NC, 1994), pp. 97–100.

9. G. S. Khodakov and Yu. A. Glukhov, Sov. J. Opt. Technol. **48**, 428 (1981).

10. P. D. Funkenbusch and S. M. Gracewski, in *Optifab '94 Conference Proceedings* (sponsored by the Industrial Diamond Association of America and the Center for Optics Manufacturing, Rochester, NY, 1994).

11. P. D. Funkenbusch, Y. Y. Zhou, T. Takahashi, D. J. Quesnel, and J. Lambropoulos, in *International Conference on Optical Fabrication and Testing*, edited by T. Kasai (SPIE, Bellingham, WA, 1995), Vol. 2576, pp. 46–52.

12. A. G. Evans and D. B. Marshall, in *Fundamentals of Friction and Wear of Materials*, edited by D. A. Rigney (American Society for Metals, Metals Park, OH, 1981), pp. 441–452.

13. T. S. Izumitani, *Optical Glass*, American Institute of Physics Translation Series (American Institute of Physics, New York, 1986).

14. S. Yoshida and H. Ito, Bull. Jpn. Soc. Precis. Eng. **24**, 239 (1990).

15. T. G. Bifano, T. A. Dow, and R. O. Scattergood, Trans. ASME, B, J. Eng. Ind. **113**, 184 (1991).

16. D. Golini and S. D. Jacobs, in *Advanced Optical Manufacturing and Testing*, edited by L. R. Baker, P. B. Reid, and G. M. Sanger (SPIE, Bellingham, WA, 1990), Vol. 1333, pp. 80–91.

17. D. Golini and S. D. Jacobs, Appl. Opt. **30**, 2761 (1991).

18. Y. Namba and M. Abe, CIRP Ann. **42**, 417 (1993).

19. M. G. Schinker, Prec. Eng. **13**, 208 (1991).

20. N. J. Brown and B. A. Fuchs, in *Optical Fabrication and Testing*, 1988 Technical Digest Series (Optical Society of America, Washington, DC, 1988), Vol. 13, pp. 23–26.

21. N. J. Brown and B. A. Fuchs, in the *Proceedings of the 43rd Annual Symposium on Frequency Control* (IEEE, Piscataway, NJ, 1989), pp. 606–610.

22. J. C. Lambropoulos, T. Fang, A. Lindquist, and D. Golini, presented at the International Symposium on Manufacturing Practices and Technology, 1995 Fall Meeting of the Glass and Optical Materials Division of the American Ceramic Society, New Orleans, LA, 5–8 November 1995; also to be published in Ceramic Transactions.

23. N. J. Brown *et al.*, in the *Proceedings of the 43rd Annual Symposium on Frequency Control* (IEEE, Piscataway, NJ, 1989), pp. 611–616.

24. O. Podzimek, CIRP Ann. **35**, 397 (1986).

25. O. Podzimek, Technical Report WB-85-16, Twente University of Technology (1986), 112 pages.

26. O. Podzimek, in *High Power Lasers*, edited by E. W. Kreutz, A. Quenzer, and D. Schuöcker (SPIE, Bellingham, WA, 1987), Vol. 801, pp. 221–223.

27. F. K. Aleinikov, Sov. Phys. Tech. Phys. **27**, 2529 (1957).

28. G. S. Khodakov, V. P. Korovkin, and V. M. Al'tshu'ler, Sov. J. Opt. Technol. **47**, 552 (1980).

29. D. F. Edwards and P. P. Hed, Appl. Opt. **26**, 4670 (1987).

30. D. F. Edwards and P. P. Hed, Appl. Opt. **26**, 4677 (1987).

31. M. Buijs and K. Korpel-Van Houten, J. Mater. Sci. **28**, 3014 (1993).

32. A. L. Ardamatskii, Sov. J. Opt. Technol. **47**, 613 (1980).

33. H. Li and R. C. Bradt, J. Non-Cryst. Solids **146**, 197 (1992).

34. T. S. Izumitani, Hoya Technical Report HGW-O-7E, Hoya Glass Works, Ltd (20 February 1971).

35. R. F. Cook and G. M. Pharr, J. Am. Ceram. Soc. **73**, 787 (1990).

36. M. Sakai and R. C. Bradt, Int. Mater. Rev. **38**, 53 (1993).

37. A. G. Evans and E. A. Charles, J. Am. Ceram. Soc. **59**, 371 (1976).

38. A. G. Evans, in *Fracture Mechanics Applied to Brittle Materials*, edited by S. W. Freiman (American Society for Testing and Materials, Philadelphia, 1979), ASTM STP 678, Part 2, pp. 112–135.

39. B. R. Lawn, A. G. Evans, and D. B. Marshall, J. Am. Ceram. Soc. **63**, 574 (1980).

40. G. R. Anstis *et al*., J. Am. Ceram. Soc. **64**, 533 (1981)

41. J. Lankford, J. Mater. Sci. Lett. **1**, 493 (1982).

42. K. Niihara, R. Morena, and D. P. H. Hasselman, J. Mater. Sci. Lett. **1**, 13 (1982).

43. D. K. Shetty *et al*., J. Mater. Sci. **20**, 1873 (1985).

44. I. J. McColm, *Ceramic Hardness* (Plenum Press, New York, 1990).

45. R. L. K. Matsumoto, J. Am. Ceram. Soc. **70**, C-366 (1987).

46. Schott Glass Catalog, Publication 10000, Schott Glass Technologies Inc., Duryea, PA 18642 (1992).

47. M. Cumbo, The Institute of Optics, University of Rochester (May 1992) (unpublished work).

48. M. Cumbo, Ph.D. thesis, The Institute of Optics, University of Rochester, 1993.

49. I. M. Androsov, S. N. Dub, and V. P. Maslov, Sov. J. Opt. Technol. **56**, 691 (1989).

50. S. M. Wiederhorn *et al*., J. Am. Ceram. Soc. **57**, 337 (1974).

51. S. Wiederhorn and D. E. Roberts, prepared for NASA Manned Spacecraft Center, Structures and Mechanics Division, PR1-168-022, T-5330A, NBS, U.S. Department of Commerce, Report 10892 (1972).

52. R. F. Cook and B. R. Lawn, J. Am. Ceram. Soc. **66,** C-200 (1983).

53. A. Arora, D. B. Marshall, and B. R. Lawn, J. Non-Cryst. Solids **31**, 415 (1979).

54. J. D. Mackenzie, J. Am. Ceram. Soc. **46**, 461 (1963).

55. J. C. Lambropoulos, T. Fang, S. Xu, and S. M. Gracewski, in *Optical Manufacturing and Testing*, edited by V. J. Doherty and H. P. Stahl (SPIE, Bellingham, WA, 1995), Vol. 2536, pp. 275–286.

56. S. M. Wiederhorn, J. Am. Ceram. Soc. **52**, 99 (1969).

57. L. M. Barker, in *Fracture Mechanics Applied to Brittle Materials*, edited by S. W. Freiman (American Society for Testing and Materials, Philadelphia, 1979), ASTM STP 678, Part 2, pp. 73–82.

58. R. Hill, *The Mathematical Theory of Plasticity* (Clarendon Press, Oxford, 1950).

59. H. H. Karow, *Fabrication Methods for Precision Optics* (Wiley, New York, 1993).

60. A. Lindquist, S. D. Jacobs, and A. Feltz, in *Science of Optical Finishing*, 1990 Technical Digest Series (Optical Society of America, Washington, DC, 1990), Vol. 9, pp. 57–60.

61. Y. Zhou, P. D. Funkenbusch, D. J. Quesnel, D. Golini, and A. Lindquist, J. Am. Ceram. Soc. **77**, 3277 (1994).

62. B. R. Lawn, T. Jensen, and A. Arora, J. Mater. Sci. **11**, 573 (1976).

63. T. S. Izumitani and I. Suzuki, Glass Technol. **14**, 35 (1973).

64. T. L. Anderson, *Fracture Mechanics: Fundamentals and Applications*, 2nd ed. (CRC Press, Boca Raton, FL, 1995).

65. S. S. Chiang, D. B. Marshall, and A. G. Evans, J. Appl. Phys. **53**, 298 (1982).

66. S. S. Chiang, D. B. Marshall, and A. G. Evans, J. Appl. Phys. **53**, 312 (1982).

Thermotropic Chiral Nematic Side-Chain Polymers and Cyclic Oligomers

Low-Molar-Mass Liquid Crystals

Liquid crystals (LC's) represent a state-of-matter intermediate between a solid crystal and an isotropic liquid. A liquid crystal flows like an ordinary liquid, while other properties, such as optical and dielectric anisotropies, resemble those of a crystalline solid.[1] In general, a somewhat rigid and anisomeric molecular shape (e.g., cylindrical, lath-like, or disc-like) is conducive to the realization of an LC state.[2] Depending on whether temperature or concentration is the dominant factor in inducing mesomorphism, liquid crystals are generally classified into thermotropics and lyotropics.[1,3] Numerous mesophases have been discovered, and they are roughly categorized as follows:

(a) *Nematic mesophase*, where the molecules are aligned with their long axes parallel to each other. Macroscopically, a preferred direction is defined by the "director." The extent to which the molecules are aligned with the director is characterized by the order parameter *S*, defined as

$$S = \frac{1}{2}\left\langle 3\cos^2\theta - 1\right\rangle, \tag{1}$$

where θ is the angle between the long axis of an individual molecule and the director, and $\langle\ \rangle$ represents an average over all molecules present.

(b) *Chiral nematic* or *cholesteric mesophase*, which can be thought of as a stack of nematic layers with their directors rotated at a constant angle either clockwise or counterclockwise from one layer to the next. This spatial variation of the director leads to a helical structure in addition to a long-range orientational order, as in the nematic mesophase.

(c) *Smectic mesophase*, where the molecules exhibit not only a longitudinal order, as in the nematic mesophase, but also a lateral arrangement.

Although the existence of liquid crystals has been recognized for over a century, it is only in the past few decades that their unique linear and nonlinear optical properties have been actively explored for various applications.[4–10] The need to develop LC materials for these applications has been the main driving force behind LC research in recent years. There are basically three device concepts: (a) based on the change in molecular orientation with an applied field, LC's find use as electro-optic devices with response times of the order of a millisecond; (b) appropriate functional moieties allow LC's to respond to electrical or optical stimuli with much shorter response times, i.e., nano- to pico- and even femtosecond, thereby enabling LC's to be employed as fast active devices; (c) LC's have also been extensively explored for passive device applications in which no switching is involved, such as wave plates, polarizers, notch filters, etc.

Molecular-Level Understanding of Cholesteric Mesomorphism

In a comprehensive review article, Solladié and Zimmermann[11] presented a critical appraisal of the issues of helical sense and twisting power underlying the cholesteric mesophase. Two different approaches to the induction of cholesteric mesophase were discussed. Baessler and Labes[12] used chiral compounds that form cholesteric mesophase by themselves, while Stegemeyer and Mainusch[13] employed nematic hosts with chiral dopants. Despite the intensive research devoted previously to the issues of handedness and twisting power, the roles played by chemical structure, including molecular chirality, have remained as challenging as ever.[14] Current understanding of the cholesteric mesophase is summarized as follows:

(a) Helical sense does not correlate with the sign of the specific optical rotation or the absolute configuration of the chiral dopant. Furthermore, it has been demonstrated that inversion of helical sense may occur as a consequence of heating,[15] presumably due to the thermally induced dynamics of conformational isomerism.

(b) Inversion of molecular chirality leads to an opposite handedness at the supramolecular level, but handedness is still not understood in an absolute sense.

(c) A measure of a chiral dopant's ability to induce cholesteric mesophase formation in a nematic host, helical twisting power is strongly dependent on the nematic structure for a given chiral dopant. "Structural similarity" between the nematogenic and chiral components tends to increase helical twisting power.

(d) Helical sense has proven to be very sensitive to structural variations. For cholesteric LC's derived from sterols, the helical sense–chemical structure relationship was interpreted by Baessler and Labes.[12] For nonsteroid materials, the effect of moving the chiral center relative to the neighboring ring, aromatic or alicyclic, of the core structure can be correlated in terms of the SOL/SED and ROD/REL rules;[16,17] however, exceptions to this empiricism have been reported.[18,19]

(e) While there exist no molecular theories capable of treating helical sense at present, chiral/nematic molecular interaction models proposed by Gottarelli *et al.*[20,21] and Rinaldi *et al*.[22–24] could help to elucidate the experimentally observed handedness.

(f) Chilaya and Lisetski[25] indicated that practical applications of existing theories have been hampered by the use of many model parameters that are hard to relate to the properties of real molecules, which is still true in light of more recent approaches.[26–28]

In short, molecular-level understanding of cholesteric mesophase is still lacking at the present time, although a significant amount of empirical information on structure-property relationships has been accumulated over the years. Besides molecular theories,[25–29] computer-aided molecular modeling has been used to gain fundamental insight into LC mesomorphism. Indeed, considerable advances in computer simulation of nematic and smectic mesophases have been made in recent years.[30–33] Memmer *et al*. demonstrated cholesteric mesomorphism using Monte Carlo simulation with the Gay-Berne intermolecular potential function with cubic periodic[34] and twisted[35] boundary conditions. In addition, using the extended-atom approximation, Wilson and Dunmur[36] performed bimolecular modeling of simplified chemical structures aimed at corroborating empirical rules regarding handedness as proposed by Gray *et al*.[16]

Optical Properties of Chiral Nematics

With a longitudinal molecular alignment and the associated optical birefringence, Δn, nematic LC's are well-suited for the fabrication of wave plates to accomplish polarization control. Since optical retardance increases with increasing birefringence for a given thickness, LC's with higher birefringence values call for thinner films in which a higher degree of mesogenic order can be achieved. Nematic alignment also provides an added advantage to second- and third-order nonlinear optical applications where mesogenic cores are nonlinear optically active. The ability to form stable glass with a glass transition temperature T_g above the ambient further enhances the potential for practical applications.

The helical structure underlying the cholesteric mesophase can be characterized by both the helical pitch and its handedness. Helical pitch is defined as the distance along the helical axis over which the director rotates by 360°, and handedness describes the direction in which helical twisting occurs. Depending on the chiral nature of the perturbation, both right- and left-handed helices are possible. The helical structure gives rise to two identifiable textures: focal conic and Grandjean.[36] In focal conic texture, the helical axes are parallel to the substrate surface; whereas in Grandjean texture, the axes are perpendicular to the substrate surface. The Grandjean texture is particularly important because it can reflect incident light over a selective wavelength region. Moreover, this selective reflectivity is accompanied by circular polarization of light, serving as the basis of high-efficiency polarization.[7]

According to well-established theories, the selective reflection wavelength λ_R of a cholesteric LC is governed by the following equation:[37,38]

$$\lambda_R = n_{\text{avg}}\, p\, \cos\theta, \tag{2}$$

where p is the pitch length, θ is the angle of incidence, and n_{avg} is the average refractive index defined as

$$n_{\text{avg}} = \frac{1}{2}\left(n_e + n_0\right), \tag{3}$$

with n_e and n_0 representing extraordinary and ordinary indices of refraction, respectively, of the nematic layers. It has been shown[39] that the bandwidth of selective reflection $\Delta\lambda$ is related to other optical parameters by

$$\Delta\lambda = \lambda_R \frac{\Delta n}{n_{\text{avg}}}, \tag{4}$$

where the optical birefringence Δn is defined as n_e–n_0. Another parameter of interest to molecular design is the so-called helical twisting power (HTP), defined as[40]

$$\mathrm{HTP} = \left(\frac{dp}{dx_{\mathrm{ch}}}\right)_{x_{\mathrm{ch}}\to 0}, \tag{5}$$

and represents the ability of a chiral group to induce cholesteric mesomorphism in a nematic host. Note that higher HTP values require less chiral dopant, in mole fraction, x_{ch}, to yield the same λ_R value. Selective reflection bandwidth $\Delta\lambda$ is another optical parameter of interest to molecular design.

Factors Contributing to Enhanced Optical Birefringence and Selective Wavelength Reflection Bandwidth

Optical birefringence and selective reflection bandwidth are among the molecular design criteria of chiral nematics. From Eqs. (3) and (4) it is clear that bandwidth $\Delta\lambda$ depends on refractive indices n_e and n_0 at a given λ_R. The refractive indices of a uniaxial LC are governed by the LC molecular structure, wavelength, and temperature. Typically, n_0 falls within 1.50±0.04 in the visible spectral region and is weakly dependent on molecular structure. On the other hand, n_e is strongly dependent on molecular structure. Its value varies from about 1.5 for completely saturated compounds to about 1.9 for highly conjugated LC's.[5,38,41,42] Therefore, one can obtain Eq. (6) by differentiating Eq. (4) while keeping n_0 constant:

$$\delta\Delta\lambda \cong \frac{\lambda_R n_0}{n_{\mathrm{avg}}^2}\,\delta\Delta n. \tag{6}$$

Apparently, Δn plays a dominant role in determining the $\Delta\lambda$ value, even though n_{avg} also increases slightly with increasing Δn. This suggests that to achieve a broad selective reflection band, high birefringence nematic and chiral moieties are desired. In what follows, the parameters contributing to an enhanced Δn in nematic layers constituting the cholesteric mesophase will be identified for assessment.

In theory, the optical birefringence of a nematic LC is determined by[43]

$$\Delta n = G(T)\frac{\lambda^2\lambda^{*2}}{\lambda^2 - \lambda^{*2}}, \tag{7}$$

in which

$$G(T) = gNZS\left(f_{\parallel}^{*} - f_{\perp}^{*}\right), \tag{8}$$

where g is a proportionality constant independent of the LC material, N the number of molecules per unit volume, Z the average number of active electrons per LC molecule, S the order parameter, and $\left(f_{\parallel}^{*} - f_{\perp}^{*}\right)$ the differential oscillator strength at the mean resonance wavelength λ^{*}. The factors affecting Δn are analyzed below:

(a) N represents the packing density of LC molecules. A short carbon chain (or short spacer in LCP's) and a large intermolecular force will yield a large birefringence value because of an increased N value. Nevertheless, the ability to increase N to an appreciable extent via molecular design is rather limited.

(b) Z is the average number of active electrons. Three types of electronic transition in organic molecules contribute to Δn: $\sigma \to \sigma^{*}$, $n \to \pi^{*}$, and $\pi \to \pi^{*}$. The $\pi \to \pi^{*}$ transition, representing an excitation of π-electrons, is the most commonly encountered in LC molecules with unsaturated bonds and is the primary contributor to an increased Δn. Increasing the conjugation length or the number of delocalized π-electrons in an LC molecule is therefore a very effective method of enhancing its optical birefringence.

(c) The mean resonance frequency λ^{*} is closely related to the UV absorption spectrum of an LC molecule. From Eq. (7), λ^{*} appears to present a significant effect on Δn. As a consequence, λ^{*} can be increased by increasing the conjugation length.

(d) $\left(f_{\parallel}^{*} - f_{\perp}^{*}\right)$ represents absorption anisotropy. The larger the $\left(f_{\parallel}^{*} - f_{\perp}^{*}\right)$ factor, the greater the Δn value; however, the relationship between $\left(f_{\parallel}^{*} - f_{\perp}^{*}\right)$ and molecular structure is not well understood at this point.

(e) Order parameter S is a function of molecular structure, temperature, and surface alignment. The temperature dependence of S in a nematic mesophase follows:

$$S \cong \left(1 - \frac{T}{T_c}\right)^{\beta}, \tag{9}$$

where T is the temperature, T_c is the nematic-isotropic transition temperature (or clearing temperature), and β is a material constant. Thus, the temperature dependence

of Δn originates primarily in the temperature dependence of S. Furthermore, a higher Δn value will result from a lower processing temperature under otherwise identical conditions.

From the above analysis, it is concluded that the number of delocalized π-electrons plays a major role in achieving high optical birefringence in nematics and, as a result, a broad selective reflection band in cholesterics. However, diminishing solubility in common solvents and bathochromic shift into the visible region impose a limit to which the conjugation length can be increased in favor of optical birefringence. On the other hand, it is anticipated that saturated ring systems are desirable for low optical birefringence and hence a narrow selective reflection band.

Mesophase Fixation via Vitrification, *In-Situ* Polymerization, or Crosslinking

In the applications based on both active and passive device concepts in which field-induced molecular orientation is not involved, it is advantageous to maintain mesomorphic ordering over a long period of time. Various methodologies have been explored to overcome the problems arising from the sensitivity of helical pitch to variations in temperature, pressure, external electric or magnetic fields, and chemical vapors as indicated in Ref. 44. The common strategy is to induce mesophase fixation in an appropriate matrix. Specific methods to achieve this goal include the following:

(a) Synthesis of side-chain or main-chain chiral nematic polymers that have the potential of forming a glassy matrix to "freeze" the requisite Grandjean texture.

(b) Photopolymerization of acrylate or methacrylate monomers, existing in a prescribed mesomorphic state, which contain cholesterol[45] or (hydroxypropyl)cellulose[46] as the pendant group.

(c) Photo-induced crosslinking of lyotropic mesophases consisting of poly(γ-butyl D- or L-glutamate) in triethylene glycol dimethacrylate, the latter serving both as a solvent and a crosslinker.[44,47]

Although both crosslinking and *in-situ* polymerization procedures are appealing to practical applications, the results are less than optimal. Notch filters (i.e., a pair of left- and right-handed devices stacked together) produced in this manner were found to possess an extinction of 0.2 to 0.8 optical density unit,[44,47] whereas the vitrification approach yields an extinction of 2.0 optical density units on substrates without surface treatment.[48] It appears that volume reduction, accompanying the curing process in general, contributes to the diminished extinction by destroying the alignment achieved in the fluid state.

Chiral Nematic Polymers

For electro-optic-device applications using field-induced molecular orientation, LC's function in the fluid state to offer a response time of the order of a millisecond. For the other two device concepts mentioned previously, a solid film is desirable in view of much-improved mesophase stability and environmental durability over a fluid film. In principle, an LC mesophase intended for an optical application can be frozen in a glassy matrix to avoid light scattering from grain boundaries present in a polycrystalline film. However, most LC's lack the ability to vitrify and, as a result, liquid crystalline polymers (LCP's) have attracted a great deal of attention in recent years. Several books and review articles have appeared on the fundamentals and potential applications of this class of optical materials.[49–53] Compared with LC's that tend to crystallize on cooling, LCP's are unique in that the particular mesophase desired can be frozen in the polymer matrix by first heating the sample close to the upper limit of the mesophase temperature range and then quenching it to below the glass transition temperature.

In regard to chemical structure, thermotropic LC polymers can be categorized into main-chain and side-chain polymers. Thermotropic LC polymers known to exhibit the cholesteric mesophase are surveyed in what follows.

1. Main-Chain Polymers

There exist numerous reports on thermotropic main-chain cholesteric LC polymers based on (*R*)-(+)-3-methyladipic acid[54–56] and chiral glycols and glycerols.[57,58] Tables 4 and 5 of Chap. 2 in Ref. 51 summarize the structures and mesomorphic properties of LC homopolymers and copolymers carrying the (*R*)-(+)-3-methyladipoyl group. The information available in the literature confirms the left-handed nature of these materials. No optical characterizations of thermotropic polymers containing chiral glycol and glycerol ethers have been reported, but the crystalline or semicrystalline character of these materials and their relatively high mesophase transition temperatures suggest that these materials are not likely to be suitable for optical device applications.

2. Polypeptides

It is well known that polypeptides, such as poly(γ-benzyl L-glutamate), exhibit lyotropic mesomorphism in a number of solvents;[54] however, their thermotropic behaviors have not been reported until recently by Watanabe *et al.*,[60–63] who presented several examples of derivatized poly(L-glutamate) exhibiting the cholesteric mesophase. Mesomorphism in these copolypeptides is believed to be due to the formation of mesogenic α-helices together with chiral perturbations on the backbone, while the flexible pendant groups serve as a solvent, as in a lyotropic system. According to Refs. 60–63, the helical sense of the cholesteric mesophase can be reversed by an inversion of chirality on the backbone. The potential of poly [(γ-benzyl L-glutamate)-co-(γ-dodecyl L-glutamate)], which shows cholesteric mesophase, as an optical material for device application was also appraised in our laboratory. It was found that the selective reflection wavelength is a relatively strong function of three parameters: temperature, comonomer ratio, and chain length, which combine to make this material extremely difficult to process into devices with reproducible optical properties. Furthermore, its low T_g, typically –20°C to –30°C, precludes the possibility of achieving long-term mesophase stability or application as a freestanding film.

3. Cellulose Derivatives

(Hydroxypropyl)cellulose, HPC, has been extensively studied because its mesomorphism can be realized in water and common organic solvents. Most cellulose derivatives display cholesteric mesophase in solution or bulk.[64–66] Optical characterization of the esters of HPC showed a right-handed helical structure. However, in our laboratory, the selective reflection of these thermotropic materials was found to be extremely weak with optical densities of less than 0.10 as compared to the theoretical limiting value of 0.30. The other disadvantage is the low T_g (<0°C), which prevents the Grandjean texture from being frozen in the glassy matrix.

4. Side-Chain Homopolymers

Freidzon *et al.*[67] reported acrylate homopolymers carrying cholesteryl pendant groups. The thermal characterization data showed a 2°C to 5°C temperature range for the existence of a cholesteric mesophase preceded by a smectic mesophase over a temperature range of up to 100°C, depending on the polymer molecular weight. In view of the fact that cholesterol-containing monomers are usually mesomorphic in their own right (typically cholesteric), it is not surprising that the desired cholesteric mesophase is overwhelmed by the higher-order smectic mesophase as a result of polymerization. Thus, it is advisable to explore chiral building blocks other than cholesterol. In fact, the first examples of cholesteric homopolymers using nonmesomorphic monomers containing (*S*)-2-methyl-1-butyloxy moiety and polysiloxane as the backbone have been successfully synthesized[68] and characterized to present a left-handed helical structure according to the commonly accepted convention.[69,70] The same chiral moiety was also employed to synthesize cholesteric homopolymers with a side-on attachment.[71] The fact that the selective reflection wavelength of homopolymers cannot be readily tuned by comonomer ratio, as is commonly achieved in copolymers, is expected to limit the practical applications in which the capability for wavelength tuning is desired.

5. Side-Chain Copolymers

Existing cholesteric side-chain copolymers have been extensively reviewed in Chap. 2 of Ref. 51 and Chap. 9 of Ref. 52. Typically, a nematogenic monomer, defined as one that by itself forms a nematic homopolymer, is copolymerized with a chiral, mesogenic, or nonmesogenic monomer to form a cholesteric side-chain copolymer. Although naturally occurring (–)-5-cholesten-3β-ol has been the most widely employed chiral precursor, it was found to consistently produce left-handed structures. The enantiomer of this naturally occurring cholesterol is expected to yield the right-handed counterpart, but it is not readily available, even though it has been successfully synthesized in the laboratory.[72] In addition to cholesterol, 1-phenylethylamine has also been successfully incorporated to produce cholesteric copolymer.[73] With several known nematogenic monomers, we have identified and synthesized new chiral comonomers derived from enantiomers of 1-phenylethylamine, 1-phenylethanol, 2-methoxy-2-phenylethanol, and methyl mandelate. The resultant copolymers are capable of forming the Grandjean texture with λ_R in the visible and near-infrared region. Key accomplishments are summarized as follows:

(a) Because of the availability of the enantiomers of these chiral precursors, both left- and right-handed chiral nematic copolymers were successfully synthesized.[74,75] The hitherto scarce right-handed materials have thus become available for the exploration of a variety of optical device concepts.

(b) A chiral/nematic molecular interaction model of a steric nature was successfully employed to elucidate the observed helical sense.[75] However, the applicability of this model is limited in scope, and more sophisticated molecular modeling is warranted.

(c) Helical sense observed in chiral nematic copolymers was found to be consistent with that of the low-molar-mass analogues, and helical twisting power was found to increase upon polymerization, although the effect appears to be system specific.[8]

(d) With an end-on attachment of a nematogenic rigid core to the polymer backbone, the smectic mesophase was found to predominate over the cholesteric mesophase as the *p*-phenylene ring system was replaced with *trans*-cyclohexylene counterpart.[76]

(e) The formation of Grandjean texture was found to be facilitated by moderating the polymer backbone flexibility within the acrylate and methacrylate-mixed backbone series without affecting the helical twisting power.[77]

More recently, cyanobiphenyl,[78] cyanotolan,[79] and cyanoterphenyl[80] groups were employed as high optical birefringence moieties for the synthesis of chiral nematic copolymers with a broader selective reflection band than achieved previously. Thermotropic and optical properties accompanied by chemical structures are illustrated in Tables 66.VI and 66.VII for cyanotolan- and cyanoterphenyl-containing systems, respectively. In the cyanotolan series, it is noted that for an increasing spacer length to the nematogen, T_g undergoes a monotonic decrease, whereas T_c shows an odd-and-even effect. Within the same spacer length of 4 at an increasing chiral mole fraction, T_g stays reasonably constant while a pronounced depression in T_c is observed, which is also the case with the cyanoterphenyl series. The selective wavelength reflection scans of Copolymer (I) with $n = 4$ and $x = 0.07$ and Copolymer (II) with $x = 0.10$ are reproduced in Fig. 66.55 to demonstrate the broadband characteristic.

Low-Molar-Mass Glass-Forming Systems

Because of their fluid nature and low viscosity, low-molar-mass LC's are capable of forming uniform films with a high degree of mesomorphic ordering. However, as indicated earlier, there are several obvious disadvantages: a lack of environmental durability and long-term mesophase stability, and the inability to vitrify in general. These problems can be

Table 66.VI: Thermal and optical properties and molecular weights of chiral nematic copolymers containing cyanotolan and 1-phenylethanol as pendant groups.

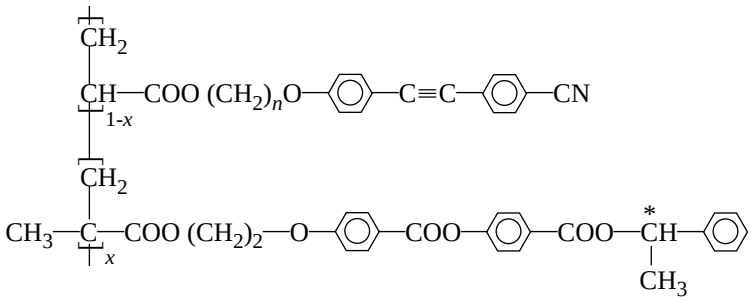

(I)

Spacer	Chiral x	Phase Transition[a] (°C)	ΔC_p (W/g)	ΔH_c (J/g)	$\overline{M}_w$	$\overline{M}_w/\overline{M}_n$	λ_R (nm)
2	0.05	G 76 Ch 112 I	0.16	2.5	11,900	1.7	840
3	0.05	G 58 Ch 85 I	0.13	0.5	8,980	1.6	(b)
4	0.05	G 45 Ch 117 I	0.14	1.7	12,200	2.3	920
4	0.07	G 43 Ch 104	0.13	1.3	10,800	2.3	770
4	0.13	G 48 Ch 94	0.13	1.4	13,700	2.2	450
6	0.08	G 34 Ch 116 I	0.18	2.0	17,500	2.1	1140

(a) G: glass; Ch: cholesteric; I: isotropic.

(b) The cholesteric mesophase was identified with polarizing optical microscopy, but the selective wavelength reflection property could not be determined because of the relatively narrow mesophase temperature range that prevents adequate molecular alignment from being achieved via annealing.

Table 66.VII: Thermal and optical properties and molecular weights of chiral nematic copolymers containing cyanoterphenyl and 1-phenylethylamine as pendant groups.

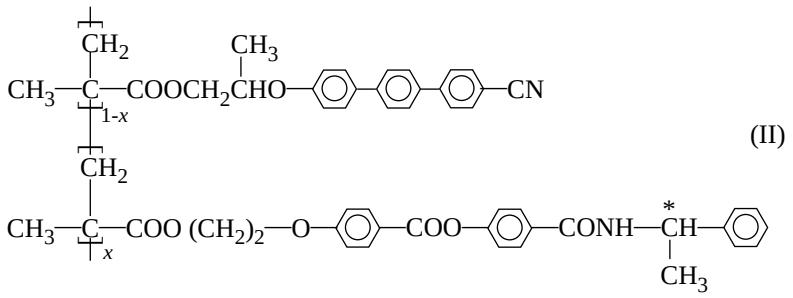

Chiral x	Phase Transition[a] (°C)	ΔC_p (W/g)	ΔH_c (J/g)	$\overline{M}_w$	$\overline{M}_w/\overline{M}_n$	λ_R (nm)
0.051	G 117 Ch 201 I	0.24	0.83	15,000	3.4	1,100
0.064	G 113 Ch 193 I	0.23	0.39	11,000	3.0	786
0.10	G 112 Ch 181 I	0.25	0.57	6,500	2.1	634
0.12	G 120 Ch 173 I	0.27	0.42	6,100	3.1	510

[a] G: glass; Ch: cholesteric; I: isotropic.

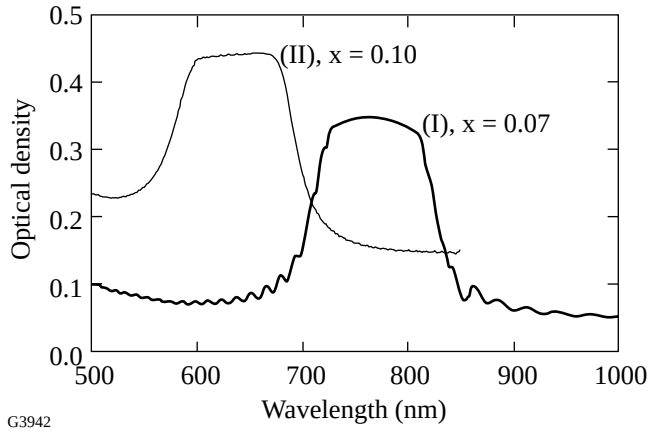

Figure 66.55
UV-visible spectra (i.e., selective wavelength reflection scans) of Copolymer (I) with $n = 4$ and $x = 0.07$ and Copolymer (II) with $x = 0.10$.

overcome by glass-forming polymeric LC's. Nevertheless, their generally high melt or solution viscosity tends to cause difficulty in processing these materials into well-aligned, uniform thin films. To circumvent all these practical problems, glassy low-molar-mass liquid crystals (GLMLC's) have emerged as a novel class of optical materials with a great deal of potential. These materials are composed of relatively small molecules with molecular weights less than 2,000. Because of their relatively low melt viscosity, it is relatively easy to form GLMLC's into large, uniform films with the desired mesophase frozen into the glassy state, thus producing an environmentally robust optical device. Since polymerization is not involved in the synthesis of GLMLC's, the availability of these materials will not be limited by the polymerizability problem as encountered with some functional monomers.

Though glass formation in small organic molecules has long been recognized,[81–85] it was not until the 1980's that active investigations of GLMLC's were resumed.[86–91] The fact that melting and crystallization peaks were observed in many of the reported differential scanning calorimetry (DSC) scans suggests that they are semicrystalline or prone to thermally induced crystallization, and thus would not be appropriate for optical device applications. In the past few years significant advances in GLMLC's have been witnessed, presumably because of the general interest in exploring organic materials for electro-optical as well as optoelectronic applications. In terms of molecular structure, GLMLC's can be classified into acyclics[86–97] and cyclics.[98–117] Acyclic compounds have been reviewed by Wedler *et al.*;[95] structurally, they carry either one or two strings. As encountered in LCP's, there are both main-chain and side-chain cyclic oligomers. Main-chain cyclic oligomers were first reported by Percec *et al.*[111–113] Side-chain cyclic oligomers include cyclophosphazene and cyclosiloxane LC's. It is noted that few cyclophos-phazene LC's show a glass transition.[114–117]

Of all the low-molar-mass glass-forming liquid crystals, cyclosiloxane LC's have been the most widely investigated following the 1981 patent of Kreuzer *et al*.[98] They are essentially cyclic analogues of side-chain siloxane polymers. Even though cyclic siloxane LC's have only 4 to 7 monomeric units, they exhibit glass transition and clearing temperatures that are generally close to[110] but in some cases[104] very different from their long-chain counterparts. A variety of mesogenic moieties have been successfully incorporated to induce the desired glass-forming and mesomorphic properties with a glass transition temperature of up to 80°C.[118] However, thus far no mesogens with an extended π-conjugation have been successfully incorporated, and no chiral moieties other than cholesterol have been attempted to induce chirality. Nevertheless, numerous potential applications of cyclosiloxanes have been explored: environmentally robust notch filter,[48] optical information storage,[103,109,119] and nonlinear optics.[120,121]

Carbocyclic Glass-Forming Chiral Nematics

Conceptually, GLMLC's represent a balance between two seemingly opposing trends: one to discourage crystallization and the other to encourage LC mesomorphism. Simply put, a delicate balance between order and disorder must be struck. The question of why certain materials are more inclined to glass formation than others has remained unanswered in glass science to date. In principle, molecular systems with a strong temperature dependence of free volume tend to vitrify upon cooling at a rate sufficiently rapid in comparison to molecular relaxation processes. Nevertheless, the implementation of this concept in molecular design is made difficult by a general lack of understanding of glass formation by organic compounds.

In search of new, alternative glass-forming liquid crystals as advanced organic materials, we have explored a novel molecular design concept in which two opposing structural features are chemically bonded via a flexible spacer, one a mesogenic group and the other a diametrically different moiety. The idea is to suppress one's tendency to crystallize by having the other present an excluded-volume effect. Since mesogenic molecules are typically structurally rigid and elongated in shape, their counterpart, referred to as the central core, should preferably be bulky and nonplanar in shape. A knowledge base exists for the design of mesogens. The central core is less understood, but it should preferably assume one of the following structures: aliphatic cyclics, bicyclics, or tricyclics. The length of the flexible spacer linking the two plays a critical role in effecting the synergy with which vitrification and mesomorphism can be accomplished without residual crystallinity or tendency toward crystallization. Stereochemical features presented by the central core may also influence the ease of glass formation as well as morphological stability. In addition to mesogens, chiral groups can also be attached to the central core to induce cholesteric mesomorphism.

In a recent series of papers,[122–124] we have reported novel glassy liquid crystals derived from 1,3,5-cyclohexanetricarboxylic and (1*R*,3*S*)-(+)-camphoric acids. Three approaches were demonstrated to be capable of inducing cholesteric mesomorphism: chiral nematic cyclic oligomer, nematogenic group attached to a chiral ring, and chiral/nematic mixture with the chemical structures shown in Fig. 66.56 and the relevant properties summarized in Table 66.VIII. Although Compound (IV) is nonmesogenic, its mixture with (III) at $x = 0.62$ yields a cholesteric mesophase. The selective wavelength properties of Compounds (V) and (VI) together with that of the mixture (IV)/(III) are displayed in Fig. 66.57. Nematic compounds [(VII) and (VIII)] and their chiral dopants [(IX) through (XIII)], as depicted in Fig. 66.58, were designed to provide new insight into the induced cholesteric mesomorphism. The observed thermotropic properties and optical properties are compiled in Table 66.IX. Note that all the resultant chiral nematic mixtures are capable of vitrification, with glass transitions occurring above the ambient, and show selective wavelength reflection in the visible and near-

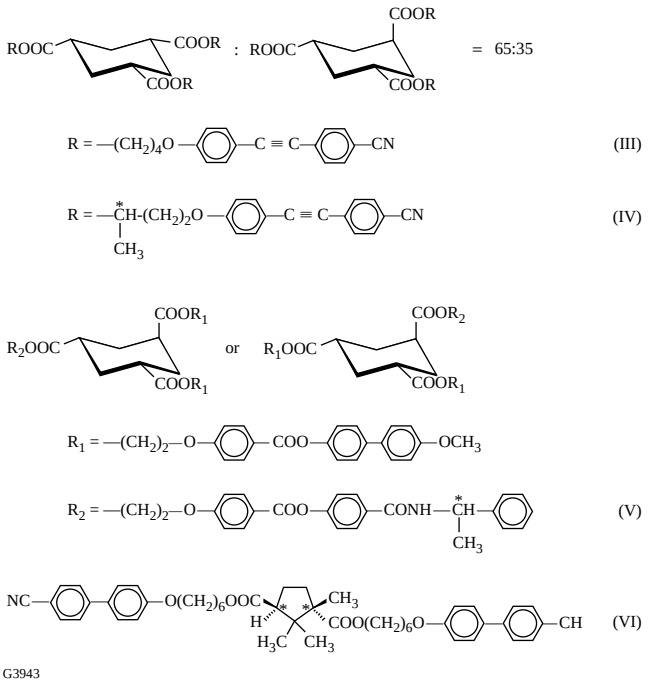

Figure 66.56
Chemical structures of Compounds (III) through (VI).

Table 66.VIII: Thermotropic and selective reflection properties of Compounds (III) through (VI).

System	Phase Transition[a] (°C)	ΔC_p (W/g)	ΔH_c (J/g)	λ_R (nm)
(III)	G 28 N 124 I	0.18	3.33	NA
(IV)	G 33 I	0.19	NA	NA
(IV)/(III), $x = 0.62$	G 36 Ch 85 I	0.19	1.73	1355
(V), $x = 0.33$	G 69 Ch 137 I	0.12	0.46	425
(VI), $x = 0.50$	G −5 Ch 42 I	0.16	2.86	1716

[a] G: glass; N: nematic; Ch: cholesteric; I: isotropic.

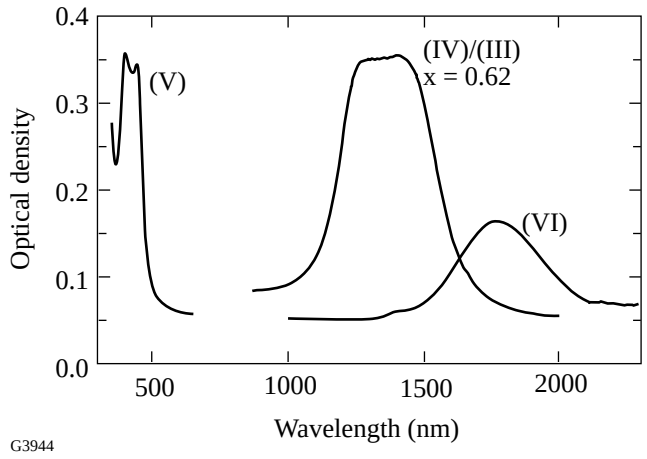

Figure 66.57
UV-visible spectra (i.e., selective wavelength reflection scans) of Compounds (V), (VI), and (IV)/(III) with $x = 0.62$.

infrared region. Furthermore, the handedness of the cholesteric mesomorphism, in relation to the absolute configuration of the chiral precursor and the value of HTP, can be accounted for by a molecular interaction model of a steric origin. The molecular environment surrounding the chiral center is depicted in Fig. 66.59, in which a benzene or naphthalene ring serves as an anchoring plane. The predictions of a left-handed cholesteric mesomorphism resulting from an absolute configuration *S*, and of a higher HTP value with naphthalene ring as an anchor compared to benzene ring, are both borne out by the experimental observations presented in Table 66.IX.[124] As demonstrated in Fig. 66.60, chiral nematic mixtures (IX)/(VII) and (XIII)/(VII), both with $x = 0.16$, possess a broad selective reflection band with pronounced side-band oscillations, a manifestation of the ease of processing into highly uniform films of which their polymeric counterparts are normally incapable.

Morphological Stability of Low-Molar-Mass Glass-Forming Systems

Since a typical quenched glass lies in a nonequilibrium state, it is suspected that thermally activated phase transformation (e.g., crystallization) may occur given sufficient energy and time. Crystallization from a glassy film is detrimental to device performance in view of light scattering from grain boundaries and deteriorating contact at an interface. In essence, the morphological stability of an LC glass determines a device's useful lifetime. Similarly, the morphological stability of an LC mesophase above T_g is critical to the optimization of a device-manufacturing process in which thermal annealing is normally performed to maximize the degree of ordering. In this process, the desired mesophase may yield to an energetically favored (meso)phase, as we have reported recently.[125] The reason is that the formation of an energetically favored (meso)phase may escape detection by standard techniques with finite scanning rates, such as differential scanning calorimetry and hot-stage polarized optical microscopy. Thus, for an LC glass to be useful in practice, it is imperative that morphological stability at temperatures both below and above T_g be addressed. In fact, crystallization from mesomorphic and isotropic melts of thermotropic LC polymers[126,127] and from isotropic melts of nonmesogenic, low-molar-mass materials[128] has been observed and its kinetics intensively investigated in recent years. While the main theme of this review is chiral nematic systems, we embarked on an investigation of morphological stability of glass-forming nematics with the anticipation that chiral nematic systems would be more stable than nematics because of the enhanced structural dissimilarity between pendant groups. Our investigation to date has concluded that when annealed at any temperature between T_g and T_m (crystalline melting point) for a period of up to a few months, most chiral nematics listed in Tables 66.VIII and 66.IX showed no evidence of crystal-

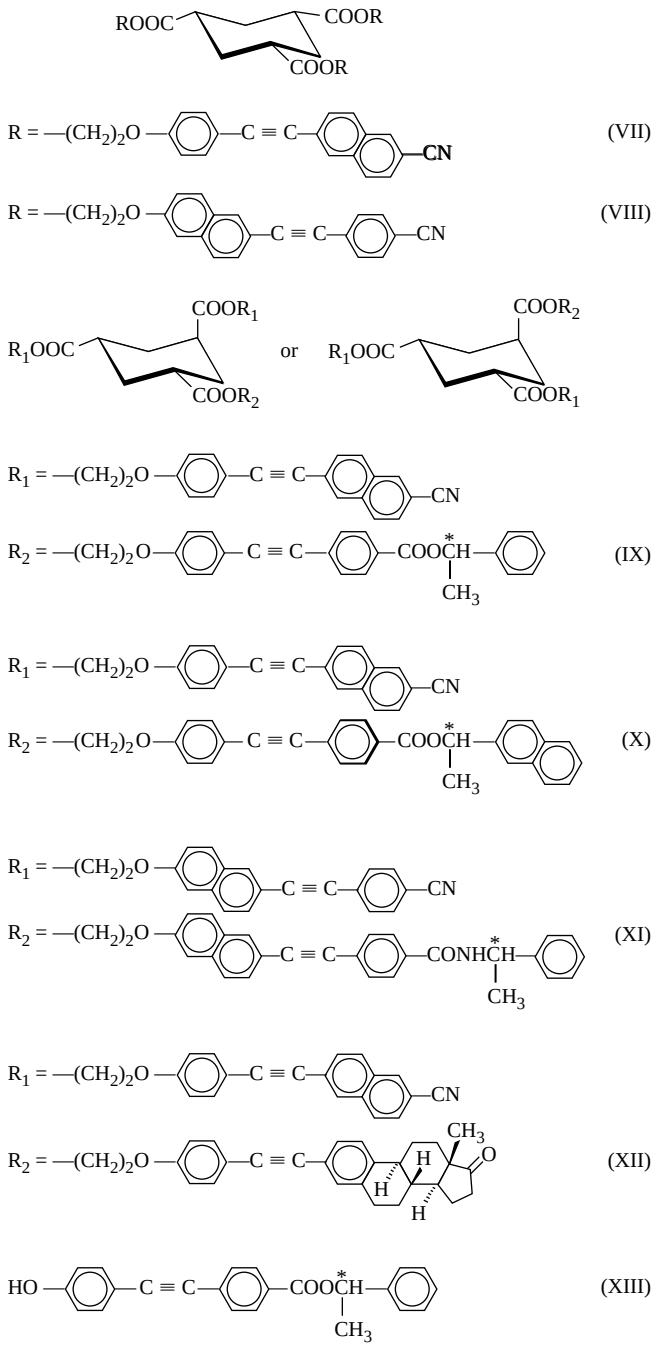

Figure 66.58
Chemical structures of Compounds (VII) through (XIII).

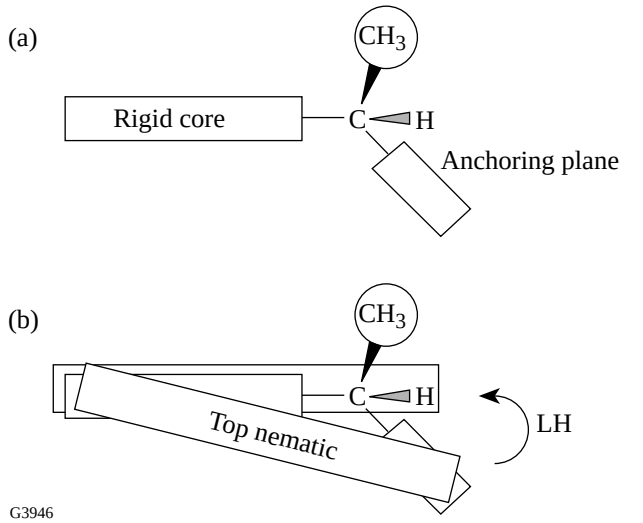

Figure 66.59
Chiral/nematic molecular interaction model: (a) chiral pendant group with an absolute configuration *S*; (b) helical twisting of the top nematic sublayer by the methyl group protruding from an asymmetric carbon center.

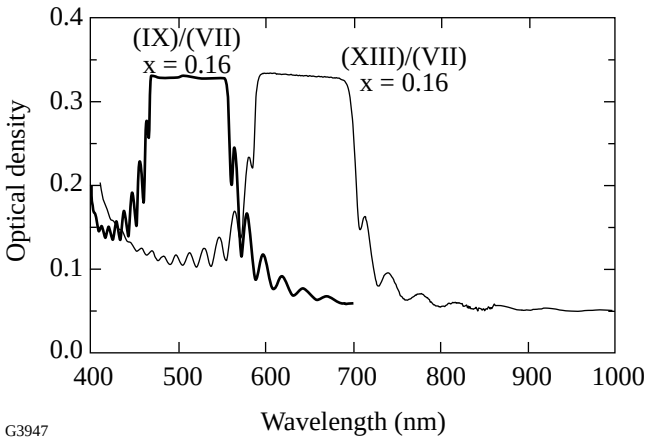

Figure 66.60
UV-visible spectra (i.e., selective wavelength reflection scans) of (IX)/(VII) on a single glass substrate and (XIII)/(VII) sandwiched between a pair of substrates, both with $x = 0.16$.

Table 66.IX: Thermotropic and optical properties of chiral nematic mixtures (VII) and (VIII) doped with (IX) through (XIII).

System	x [a]	λ_R (nm)	Phase [b] Transition(°C)	ΔC_p (W/g)	ΔH_c (J/g)	Absolute Configuration of Chiral Precursor	Handedness of Cholesteric Mesophase	10^{-4} HTP (nm^{-1})
(VII)	0.00	NA	G 60 N 197 I	0.13	2.72			
(VIII)	0.00	NA	G 65 N 191 I	0.12	2.46			
(IX)/(VII)	0.33 0.16 0.12 0.08	(c) 508 713 1024	G 61 Ch 77 I G 62 Ch 136 I G 62 Ch 155 I G 62 Ch 169 I	0.16 0.15 0.15 0.15	0.34 1.00 1.51 1.36	*S*	LH	203±3
(X)/(VII)	0.33 0.08 0.06 0.04	(d) 545 720 1070	G 70 I G 60 Ch 164 I G 60 Ch 171 I G 61 Ch 182 I	0.12 0.10 0.11 0.11	NA 2.29 1.97 2.19	*R*	RH	387±2
(XI)/(VIII)	0.33 0.20 0.14 0.09	(c) 580 880 1525	G 81 Ch 106 I G 70 Ch 132 I G 68 Ch 147 I G 66 Ch 163 I	0.12 0.11 0.11 0.14	0.47 1.30 1.20 0.69	*R*	RH	137±3
(XII)/(VII)	0.33 0.25 0.20	930 1225 1770	G 79 Ch 182 I G 72 Ch 179 I G 70 Ch 189 I	0.13 0.12 0.16	1.84 1.68 1.02	(e)	LH	53±2
(XIII)/(VII)	1.00 0.16 0.12 0.08	(d) 633 800 1160	G 28 I G 50 Ch 128 I G 51 Ch 149 I G 52 Ch 163 I	0.20 0.12 0.13 0.13	NA 1.03 1.62 1.21	*S*	LH	171±3

(a) x is defined as the number of chiral side arms divided by the total number of nematic and chiral side arms in the blend.
(b) G: glass; N: nematic; Ch: cholesteric; I: isotropic.
(c) Showing cholesteric oily streaks under polarizing optical microscope, but no selective reflection peaks available for determination of λ_R because of close proximity of T_c to T_g.
(d) Nonmesogenic.
(e) Unspecified.

lization. On the contrary, the crystallization rate is experimentally accessible in nematics that were selected for an investigation of morphological stability to identify relevant structural parameters.

We have offered a definitive basis for assessing morphological stability[129] of glass-forming liquid crystals as a novel class of advanced organic materials. Model compounds depicted in Fig. 66.61 were synthesized and their stereochemical characteristics determined by proton-NMR spectroscopy. The morphological stability was evaluated using the measurement of crystallization velocity CV, defined as the linear spherulitic growth rate, as a function of temperature between T_g and T_m, as plotted in Fig. 66.62. It was found that (a) an *all-equatorial* configuration enhances morphological stability over an *all-axial* configuration by two orders of magnitude with cyanotolan as the pendant mesogenic core; (b) morphological stability is largely unaffected by the spacer length connecting the mesogenic group to the central core, although both T_g and T_m are depressed, whereas T_c is significantly elevated by a longer spacer; (c) as cyanotolan is replaced by 1-phenyl-2-(6-cyanonaphth-2-yl)ethyne as a stronger nematogen in terms of transition temperatures and mesophase temperature range, the morphological stability was found to diminish by almost an order of magnitude; and (d) mixed *equatorial-axial* modes increase morphological stability over both *all-equatorial* and *all-axial* modes to such an extent that the morphological stability turns out to be comparable to isotactic polystyrene, a typical "slowly crystallizing" polymer, with a maximum CV of the order of 10 nm/s.

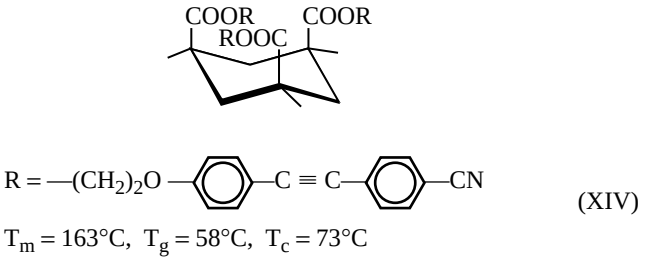

Figure 66.61
Chemical structures of (XIV) through (XVIII) plus (VII) selected for an investigation of morphological stability against crystallization.

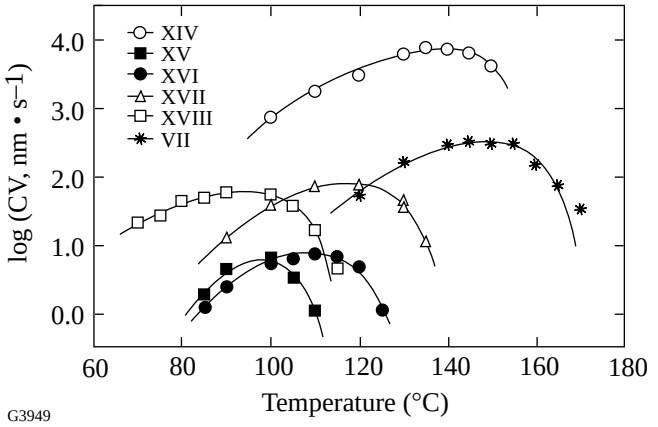

Figure 66.62
Crystallization velocity, CV, as a function of temperature of the model compounds shown in Fig. 66.61 to display the effects of stereochemistry, mesogenic core, and spacer length. The curves represent the best fit to the secondary nucleation theory.

Summary and Future Outlook

The unique property of chiral nematic liquid crystals to produce selective wavelength reflection accompanied by circular polarization has potential applications in numerous optical devices, such as notch filters, beamsplitters, circular polarizers, etc., as well as optical information processing, storage, and display. The main theme of this review is on materials capable of vitrification into cholesteric glasses as a way to preserve mesogenic order, thereby facilitating practical applications. With a glass transition temperature above the ambient, free-standing films may become a reality. Recent advances in chiral nematic side-chain polymeric and low-molar-mass systems are surveyed. Theories of optical birefringence and selective reflection bandwidth are outlined to furnish a basis for optimizing bandwidth with respect to the number of delocalized π-electrons. A wide variety of polymeric systems have been reported over the past three decades, and we have presented new systems incorporating high optical birefringence nematogenic and chiral pendant groups to increase the selective reflection bandwidth.

Because of the demonstrated capability for vitrification and relative ease of processing into uniform thin films, we have focused on the design and synthesis of low-molar-mass systems with morphological stability comparable to typical "slowly crystallizing" polymers. The underlying molecular design concept is also potentially instrumental to the development of a diversity of functional organic materials. From a practical perspective, novel systems with selective reflection occurring in the visible and infrared spectral region with a broad and

narrow bandwidth and an elevated glass transition temperature are of interest. Moreover, processing techniques capable of producing defect-free thin films, including freestanding ones, are crucial to bringing this class of optical materials to fruition.

From a fundamental perspective, a molecular interaction model of a steric origin is capable of relating helical sense of cholesteric mesomorphism to absolute configuration of the chiral precursor within a series of structurally similar systems. Nonetheless, the interpretation of helical sense and twisting power in terms of chemical structure remains as challenging as ever, despite all the theoretical and computational efforts devoted to chiral nematic systems over the last four decades. It is hoped that an appropriate theory governing the interaction between light and condensed matter, coupled with intensive computation accounting for realistic atomic and molecular interactions, will lead to a better understanding of the structure-property relationships and, hence, improved materials for practical applications.

ACKNOWLEDGEMENT

The authors wish to express their gratitude to Professor Andrew S. Kende of the Chemistry Department of the University of Rochester for his advice on organic synthesis, to Dr. Stephen D. Jacobs, Dr. Ansgar Schmid, and Mr. Kenneth L. Marshall for helpful discussions and technical assistance. The early phase of this research was supported with an Expedited Award from NSF under CTS-8714924 and by the Petroleum Research Fund administered by the American Chemical Society. The authors also wish to acknowledge the support by Kaiser Electronics in San Jose, California, by the National Science Foundation under CTS-9500737 and an engineering research equipment grant CTS-9411604, and by the Ministry of International Trade and Industry of Japan. In addition, our liquid crystal materials research was supported in part by the U.S. Department of Energy, Division of Inertial Confinement Fusion under Cooperative Agreement No. DE-FC03-92SF19460 with the Laboratory for Laser Energetics at the University of Rochester. The support of DOE does not constitute an endorsement by DOE of the views expressed in this article.

REFERENCES

1. W. H. de Jeu, *Physical Properties of Liquid Crystalline Materials* (Gordon and Breach, New York, 1980).
2. H. Finkelmann, in *Thermotropic Liquid Crystals*, edited by G. W. Gray (Wiley, New York, 1987), p. 145.
3. E. B. Priestley, in *Introduction to Liquid Crystals*, edited by E. B. Priestley, P. J. Wojtowicz, and P. Sheng (Plenum Press, New York, 1975), p. 1.
4. I. Sage, in *Thermotropic Liquid Crystals*, edited by G. W. Gray (Wiley, New York, 1987).
5. S.-T. Wu, in *Optical Materials: A Series of Advances*, edited by S. Musikant (Marcel Dekker, New York, 1990), Vol. 1, Chap. 1.
6. I.-C. Khoo and S.-T. Wu, *Optics and Nonlinear Optics of Liquid Crystals*, Nonlinear Optics, Vol. 1 (World Scientific, Singapore, 1993).
7. M. Schadt, Ber. Bunsenges. Phys. Chem. **97**, 1213 (1993).
8. S. D. Jacobs, K. A. Cerqua, K. L. Marshall, A. Schmid, M. J. Guardalben, and K. J. Skerrett, J. Opt. Soc. Am. B **5**, 1962 (1988).
9. K. Hirabayashi and T. Kurokawa, Liq. Cryst. **14**, 307 (1993).
10. D. A. McL. Smith and H. J. Coles, Liq. Cryst. **14**, 937 (1993).
11. G. Solladié and R. G. Zimmermann, Angew. Chem. Int. Ed. Engl. **23**, 348 (1984).
12. H. Baessler and M. M. Labes, J. Chem. Phys. **52**, 631 (1970).
13. H. Stegemeyer and K.-J. Mainusch, Chem. Phys. Lett. **6**, 5 (1970).
14. J. W. Goodby, J. Mater. Chem. **1**, 307 (1991).
15. A. J. Slaney *et al.*, J. Mater. Chem. **2**, 805 (1992).
16. G. W. Gray and D. G. McDonnell, Mol. Cryst. Liq. Cryst. Lett. **34**, 211 (1977).
17. N. Emoto *et al.*, Jpn. J. Appl. Phys. **28**, L 121 (1989).
18. S. Krishnamurthy and S.-H. Chen, Macromolecules **25**, 4485 (1992).
19. J. W. Goodby *et al.*, J. Am. Chem. Soc. **108**, 4729 (1986).
20. G. Gottarelli, B. Samori, and C. Stremmenos, Chem. Phys. Lett. **40**, 308 (1976).
21. G. Gottarelli *et al.*, Tetrahedron **37**, 395 (1981).
22. W. H. Pirkle and P. L. Rinaldi, J. Org. Chem. **45**, 1379 (1980).
23. P. L. Rinaldi, M. S. R. Naidu, and W. E. Conaway, J. Org. Chem. **47**, 3987 (1982).
24. P. L. Rinaldi and M. Wilk, J. Org. Chem. **48**, 2141 (1983).
25. G. S. Chilaya and L. N. Lisetski, Mol. Cryst. Liq. Cryst. **140**, 243 (1986).
26. L. Varichon, A. Ten Bosch, and P. Sixou, Liq. Cryst. **9**, 710 (1991).
27. L. N. Lisetski and A. V. Tolmachev, Liq. Cryst. **5**, 877 (1989).
28. L. A. Kutulya *et al.*, J. Phys. Org. Chem. **5**, 308 (1992).
29. W. J. A. Goossens, Mol. Cryst. Liq. Cryst. **12**, 237 (1971).
30. M. R. Wilson and M. P. Allen, Mol. Cryst. Liq. Cryst. **198**, 465 (1991).
31. M. P. Allen and M. R. Wilson, J. Comput.-Aided Mol. Des. **3**, 335 (1989).
32. D. A. Dunmur and M. R.Wilson, Mol. Simul. **4**, 37 (1989).
33. S. S. Patnaik *et al.*, Liq. Cryst. **19**, 213 (1995).

34. R. Memmer, H.-G. Kuball, and A. Schönhofer, Ber. Bunsenges. Phys. Chem. **97**, 1193 (1993).

35. R. Memmer, H.-G. Kuball, and A. Schönhofer, Liq. Cryst. **15**, 345 (1993).

36. M. R. Wilson and D. A. Dunmur, Liq. Cryst. **5**, 987 (1989).

37. D. G. McDonnell, in *Thermotropic Liquid Crystals*, edited by G. W. Gray (Wiley, New York, 1987), p. 120.

38. H. F. Gleeson and H. J. Coles, Mol. Cryst. Liq. Cryst. **170**, 9 (1989).

39. HL. De Vries, Acta Cryst. **4**, 219 (1951).

40. H. Finkelmann, in *Liquid Crystallinity in Polymers: Principles and Fundamental Properties*, edited by A. Ciferri (VCH Publisher, New York, 1991), p. 329.

41. S.-T. Wu, U. Finkenzeller, and V. Reiffenrath, J. Appl. Phys. **65**, 4372 (1989); S.-T. Wu, E. Ramos, and U. Finkenzeller, J. Appl. Phys. **68**, 78 (1990).

42. M. Hird *et al.*, Liq. Cryst. **15**, 123 (1993).

43. S.-T. Wu, Phys. Rev. A **33**, 1270 (1986).

44. S. Ishihara *et al.*, Polymer **29**, 2141 (1988).

45. P. J. Shannon, Macromolecules **17**, 1873 (1984).

46. S. N. Bhadani and D. G. Gray, Mol. Cryst. Liq. Cryst. Lett. **102**, 255 (1984).

47. T. Tsutsui and R. Tanaka, Polymer **21**, 1351 (1980).

48. M. L. Tsai, S. H. Chen, and S. D. Jacobs, Appl. Phys. Lett. **54**, 2395 (1989).

49. A. Blumstein, ed. *Liquid Crystalline Order in Polymers* (Academic Press, New York, 1978).

50. N. A. Platé, ed. *Advances in Polymer Science* (Springer-Verlag, Berlin, 1984), Vols. 59 and 60/61.

51. L. L. Chapoy, ed. *Recent Advances in Liquid Crystalline Polymers* (Elsevier, London, 1985).

52. C. B. McArdle, ed. *Side Chain Liquid Crystal Polymers* (Chapman and Hall, New York, 1989).

53. A. Ciferri, ed. *Liquid Crystallinity in Polymers* (VCH Publishers, New York, 1991).

54. H. Hara *et al.*, Macromolecules **21**, 14 (1988).

55. J. Watanabe and W. R. Krigbaum, Mol. Cryst. Liq. Cryst. **135**, 1 (1986).

56. W. R. Krigbaum *et al.*, Mol. Cryst. Liq. Cryst. **76**, 79 (1981).

57. E. Chiellini, P. Nieri, and G. Galli, Mol. Cryst. Liq. Cryst. **113**, 213 (1984).

58. E. Chiellini and G. Galli, Macromolecules **18**, 1652 (1985).

59. D. B. DuPré and E. T. Samulski, in *Liquid Crystals: The Fourth State of Matter*, edited by F. D. Seava (Marcel Dekker, New York, 1979), p. 203.

60. J. Watanabe *et al.*, Macromolecules **17**, 1004 (1984).

61. J. Watanabe *et al.*, Macromolecules **18**, 2141 (1985).

62. J. Watanabe, M. Goto, and T. Nagase, Macromolecules **20**, 298 (1987).

63. J. Watanabe and T. Nagase, Macromolecules **21**, 171 (1988).

64. S.-L. Tseng, G. V. Laivins, and D. G. Gray, Macromolecules **15**, 1262 (1982).

65. G. V. Laivins and D. G. Gray, Macromolecules **18**, 1753 (1985).

66. L. Rusig *et al.*, J. Polym. Sci. B, Polym. Phys. **32**, 1907 (1994).

67. Y. S. Freidzon *et al.*, Makromol. Chem., Rapid Commun. **6**, 625 (1985).

68. H. Finkelmann and G. Rehage, Makromol. Chem., Rapid Commun. **3**, 859 (1982).

69. M. Born and E. Wolf, *Principles of Optics: Electromagnetic Theory of Propagation, Interference and Diffraction of Light*, 4th ed. (Pergamon Press, New York, 1970), Chap. 1.

70. H. Kozawaguchi and M. Wada, Mol. Cryst. Liq. Cryst. **45**, 55 (1978).

71. R. A. Lewthwaite, G. W. Gray, and K. J. Toyne, J. Mater. Chem. **2**, 119 (1992).

72. D. E. Mickus, D. G. Levitt, and S. D. Rychnovsky, J. Am. Chem. Soc. **114**, 359 (1992).

73. H. Finkelmann, J. Koldehoff, and H. Ringsdorf, Angew. Chem. Int. Ed. Engl. **17**, 935 (1978).

74. M. L. Tsai and S. H. Chen, Macromolecules **23**, 1908 (1990).

75. S. Krishnamurthy and S.-H. Chen, Macromolecules **24**, 3481 (1991).

76. S. Krishnamurthy, S.-H. Chen, and T. N. Blanton, Macromolecules **25**, 5119 (1992).

77. S. Krishnamurthy and S.-H. Chen, Macromolecules **24**, 4472 (1991).

78. J. C. Mastrangelo and S.-H. Chen, Macromolecules **26**, 6132 (1993).

79. H. Shi and S.-H. Chen, Macromolecules **26**, 5840 (1993).

80. J. C. Mastrangelo and S. H. Chen, Macromolecules, to be submitted.

81. B. Rosenberg, J. Chem. Phys. **31**, 238 (1959).

82. D. J. Plazek and J. H. Magill, J. Chem. Phys. **45**, 3038 (1966).

83. K. Tsuji, M. Sorai, and S. Seki, Bull. Chem. Soc. Jpn. **44**, 1452 (1971).

Publications and Conference Presentations

Publications

C. T. Cotton, "Design Considerations for the OMEGA Upgrade Final Focus Lens," in the *1995 International Symposium on Optical Science*, edited by J. M Sasian (SPIE, Bellingham, WA, 1995), Vol. 2537, pp. 308–315.

P. M. Fauchet, L. Tsybeskov, C. Peng, S. P. Duttagupta, J. von Behren, Y. Kostoulas, J. V. Vandyshev, and K. D. Hirshman, "Light-Emitting Porous Silicon: Materials Science, Properties, and Device Applications," IEEE J. Sel. Top. Quantum Electron. **1**, 1126 (1995).

V. N. Goncharov, R. Betti, R. L. McCrory, P. Sorotokin, and C. P. Verdon, "Self-Consistent Stability Analysis of Ablation Fronts with Large Froude numbers," Phys. Plasmas **3**, 1402 (1996).

W. Kordonski and S. Jacobs, "Model of Magnetorheological Finishing," in *Sixth International Conference on Adaptive Structures*, edited by C. A. Rogers, J. Tani, and E. J. Breitbach (Technomic Publishing Co., Lancaster, PA, 1996), pp. 63–74.

Y. Kostoulas, K. B. Ucer, L. Waxer, G. W. Wicks, I. A. Walmsley, and P. M. Fauchet, "Ultrafast Carrier Lifetime in Low-Temperature-Grown GaAs, InP, and InGaP," in the *Proceedings of the 7th Annual Meeting of LEOS '94 IEEE Lasers and Electro-Optics Society* (LEOS, Boston, MA, 1994), pp. 21–22.

W. Kula, R. Adam, and R. Sobolewski, "Y-Ba-Cu-O Thin-Film Structures with a Nonuniform In-Depth Oxygen Concentration Profile," in *Applied Superconductivity 1995*, edited by D. Dew-Hughes, Proceedings of EUCAS 1995, Vol. 2 (Institute of Physics, Bristol, UK, 1995), pp. 895–898.

J. C. Mastrangelo, S.-H. Chen, and T. N. Blanton, "Glass-Forming Ability and Morphological Stability of Cyclohexane and Biocyclooctene Rings Containing Disperse Red 1," Chem. Mater. **7**, 1904 (1995).

D. D. Meyerhofer, J. P. Knauer, S. J. McNaught, and C. I. Moore, "Observation of Relativistic Mass Shift Effects during High-Intensity-Laser–Electron Interactions," J. Opt. Soc. Am. B **13**, 113 (1996).

H. Shi, S.-H. Chen, M. E. De Rosa, T. J. Bunning, and W. W. Adams, "Dynamic Mechanical Properties of Cyclohexane-Based Glass-Forming Liquid Crystals and a Linear Side-Chain Polymer Analogue," Liq. Cryst. **20**, 277 (1996).

C.-C. Wang, M. Currie, D. Jacobs-Perkins, R. Sobolewski, T. Y. Hsiang, and M. J. Feldman, "Electro-Optic Measurements of Single-Flux-Quantum Pulses," in *Applied Superconductivity 1995*, edited by D. Dew-Hughes, Proceedings of EUCAS 1995, Vol. 2 (Institute of Physics, Bristol, UK, 1995), pp. 787–791.

B. Yaakobi, D. Shvarts, R. Epstein, and Q. Su, "X-Ray Backlighting Imaging of Mixed Imploded Targets," Laser Part. Beams **14**, 81 (1996).

X. Zhou, S. Alexandrou, and T. Y. Hsiang, "Monte Carlo Investigation of the Intrinsic Mechanism of Subpicosecond Pulse Generation by Nonuniform Illumination," J. Appl. Phys. **77**, 706 (1995).

Forthcoming Publications

E. L. Alfonso, S.-H. Chen, M. D. Wittman, S. Papernov, and D. Harding, "A Parametric Study of Microencapsulation Approach to the Preparation of Polystyrene Shells," to be published in Polymer.

T. R. Boehly, D. L. Brown, R. S. Craxton, R. L. Keck, J. P. Knauer, J. H. Kelly, T. J. Kessler, S. A. Kumpan, S. J. Loucks, S. A. Letzring, F. J. Marshall, R. L. McCrory, S. F. B. Morse, W. Seka, J. M. Soures, and C. P. Verdon, "Initial Performance Results of the OMEGA Laser System," to be published in Optics Communications.

S.-H. Chen, J. C. Mastrangelo, T. N. Blanton, A. Bashir-Hashemi, and K. L. Marshall, "Novel Glass-Forming Liquid Crystals. IV. Effects of Central Core and Pendant Group on Vitrification and Morphological Stability," to be published in Liquid Crystals.

S.-H. Chen, J. C. Mastrangelo, and H. Shi, "Novel Low Molar Mass, Glass-Forming Liquid Crystals: Molecular Design, Synthesis, and Morphological Stability," to be published in the Proceedings of Polymers for Advanced Optical Applications.

S.-H. Chen, H. Shi, J. C. Mastrangelo, and J. J. Ou, "Thermotropic Chiral Nematic Side-Chain Polymers and Cyclic Oligomers," to be published in Progress in Polymer Science.

A. V. Chirokikh, W. Seka, A. Simon, and R. S. Craxton, "Brillouin Scattering in Long-Scale-Length Laser Plasmas," to be published in Physics of Plasmas.

C. T. Cotton, "The Design of an All-Spherical, Three-Mirror, Off-Axis Telescope Objective," to be published in the OSA Proceedings of the International Optical Design Conference '94, Rochester, NY.

B. DeMarco, C. W. Barnes, K. Kearney, and R. L. Kremens, "Neutron Yield Measurement on the OMEGA Laser System," to be published in the Review of Scientific Instruments.

D. Fried, R. E. Glena, J. D. B. Featherstone, and W. Seka, "Permanent and Transient Changes in the Reflectance of CO_2 Laser-Irradiated Dental Hard Tissues at λ = 9.3, 9.6, 10.3, and 10.6 μm and at Fluences between 1–20 J/cm^2," to be published in Lasers in Surgery and Medicine.

V. N. Goncharov and R. Betti, "Growth Rate of the Ablative Rayleigh-Taylor Instability for Indirect-Drive ICF," to be published in Physics of Plasmas.

V. N. Goncharov, R. Betti, R. L. McCrory, P. Sorotokin, and C. P. Verdon, "Self-Consistent Stability Analysis of Ablation Fronts for Inertial Confinement Fusion," to be published in Physics of Plasmas.

V. N. Goncharov, R. Betti, R. L. McCrory, P. Sorotokin, and C. P. Verdon, "Self-Consistent Stability Analysis of Ablation Fronts with Large Froude Numbers," to be published in Physics of Plasmas.

J. H. Kelly, T. R. Boehly, J. M. Soures, D. L. Brown, R. Boni, R. S. Craxton, R. L. Keck, T. J. Kessler, R. Kremens, S. A. Kumpan, S. A. Letzring, S. J. Loucks, R. L. McCrory, S. F. B. Morse, W. Seka, S. Skupsky, and C. P. Verdon, "The Activation of the Upgraded OMEGA Laser at the University of Rochester," to be published in the SPIE Proceedings of the 15th International Conference on Coherent and Nonlinear Optics, St. Petersburg, Russia, June 1995.

J. H. Kelly, T. R. Boehly, J. M. Soures, D. L. Brown, R. Boni, R. S. Craxton, R. L. Keck, T. J. Kessler, R. L. Kremens, S. A. Kumpan, S. A. Letzring, S. J. Loucks, R. L. McCrory, S. F. B. Morse, W. Seka, S. Skupsky, and C. P. Verdon, "The Activation of the Upgraded OMEGA Laser at the University of Rochester," to be published in the SPIE Proceedings of the 1st Annual International Conference on Solid-State Lasers for Application to Inertial Confinement Fusion (ICF), Monterey, CA, 30 May–2 June 1995.

Y. Lin, T. J. Kessler, and G. N. Lawrence, "Design of Continuous Surface-Relief Phase Plates by Simulated Annealing to Achieve Control of Focal Plane Irradiance," to be published in Optics Letters.

S. G. Lukishova, S. V. Belyaev, K. S. Lebedev, E. A. Magulariya, A. W. Schmid, and H. V. Malimonenko, "cw and High-Repetition-Rate Lasing in Nd:YAG Resonators with Chiral-Nematic Liquid-Crystal Mirrors: A Study of Nonlinear Responses," to be published in Kvantovaya Electronika.

S. G. Lukishova, S. V. Belyaev, K. S. Lebedev, E. A. Magulariya, A. W. Schmid, and N. V. Malimonenko, "Nonlinear Bleaching in the Selective Reflection of Non-absorbing Chiral-Nematic Liquid-Crystal Thin Films," to be published in JETP Letters.

R. S. Marjoribanks, F. W. Budnik, H. Chen. and D. D. Meyerhofer, "Plasma Electron Temperature in Picosecond Laser Plasmas from Quasi-Steady Ratio of Isoelectronic Lines," to be published in the Journal of the Optical Society of America B.

J. C. Mastrangelo and S.-H. Chen, "Novel Glass-Forming Organic Materials. 2. Cyclohexane and Bicyclooctene with Pendant Pyrenene and Carbazole," to be published in Chemistry of Materials.

S. M. McCormack, D. Fried, J. D. B Featherstone, R. E. Glena, and W. Seka, "Scanning Electron Microscope Observations of CO_2 Laser Effects on Dental Enamel," to be published in the Journal of Dental Research.

R. L. McCrory, J. M. Soures, C. P. Verdon, T. R. Boehly, D. K. Bradley, R. S. Craxton, J. A. Delettrez, R. Epstein, P. A. Jaanimagi, S. D. Jacobs, R. L. Keck, J. H. Kelly, T. J. Kessler, H. Kim, J. P. Knauer, R. L. Kremens, S. A. Kumpan, S. A. Letzring, F. J. Marshall, P. J. McKenty, S. F. B. Morse, A. Okishev, W. Seka, R. W. Short, M. D. Skeldon, S. Skupsky, M. Tracy, and B. Yaakobi, "Direct-Drive Laser Fusion Experimental Program at the University of Rochester Laboratory for Laser Energetics," to be published in the Proceedings of the Conference on Plasma Physics and Controlled Nuclear Fusion Research, Madrid, Spain, September 1994.

R. L. McCrory, J. M. Soures, C. P. Verdon, T. R. Boehly, D. K. Bradley, R. S. Craxton, J. A. Delettrez, R. Epstein, P. A. Jaanimagi, S. D. Jacobs, R. L. Keck, J. H. Kelly, T. J. Kessler, H. Kim, J. P. Knauer, R. L. Kremens, S. A. Kumpan, S. A. Letzring, F. J. Marshall, P. W. McKenty, S. F. B. Morse, A. Okishev, W. Seka, R. W. Short, M. D. Skeldon, S. Skupsky, M. Tracy, and B. Yaakobi, "Experiments on the OMEGA to Validate High-Gain, Direct-Drive Performance on the National Ignition Facility," to be published in the Proceedings of the 12th International Conference on Laser Interaction and Related Plasma Phenomena, Osaka, Japan, April 1995.

C. J. McKinstrie, J. S. Li, R. E. Giacone, and H. X. Vu, "Two-Dimensional Analysis of the Power Transfer Between Crossed Laser Beams," to be published in Physics of Plasmas.

D. Ofer, U. Alon, D. Shvarts, R. L. McCrory, and C. P. Verdon, "Modal-Model for the Non-Linear Multi-Mode Rayleigh-Taylor Instability," to be published in Physics of Plasmas.

A. Okishev, M. D. Skeldon, S. A. Letzring, W. R. Donaldson, A. Babushkin, and W. Seka, "The Pulse-Shaping System for the 60-Beam, 30-kJ (UV) OMEGA Laser," to be published in the Proceedings of Laser Optics '95 Conference, St. Petersburg, Russia, 27 June–1 July 1995.

S. S. Papernov and A. W. Schmid, "A Comparison of Laser-Induced Damage Morphology in Three Model Thin-Film Systems: HfO_2, Y_2O_3, and Ta_2O_5," to be published in the Proceedings of the XXVI Annual Symposium on Optical Materials for High Power Lasers, Boulder, CO, 24–26 October 1994.

J. Z. Roach, A. Ninko, S. W. Swales, and T. Morris, "Design and Evaluation of a Screen CCD Imaging System," to be published in Optical Engineering.

A. W. Schmid, T. J. Kessler, S. Papernov, and J. Barone, "Low-Surface-Energy Photoresist as a Medium for Optical Replication," to be published in Applied Physics Letters.

A. Simon, "Comparison Between SBS Theories and Experiment," to be published in the Proceedings of the La Jolla Summer School '95, Plasma Physics and Technology (AIP).

M. D. Wittman, R. Q. Gram, H. Kim, C. K. Immesoete, S. G. Noyes, and S. Scarantino, "Increased Retention Time for Hydrogen and Other Gases by Polymer Shells Using Optically Transparent Aluminum Layers," to be published in the Journal of Vacuum Science and Technology.

W. Xiong, Y. Kostoulas, X. Weng, P. M. Fauchet, and R. Sobolewski, "Femtosecond Study of the Electronic Structure in Semiconducting Y-Ba-Cu-O," to be published in Physical Review B.

B. Yaakobi and J. A. Delettrez, "Abel Inversion of Spherical Plasma Images," to be published in Optics Communications.

B. Yaakobi, Q. Su, R. S. Craxton, and R. Epstein, "Diagnosis of Core-Shell Mixing Using Absorption and Emission Spectra of a Doped Layer," to be published in the Journal of Quantitative Spectroscopy and Radiative Transfer.

B. Yaakobi, R. Epstein, C. F. Hooper, Jr., D. A. Haynes, Jr., and Q. Su, "Diagnosis of High-Temperature Implosions Using Low- and High-Opacity Krypton Lines," to be published in the Journal of X-Ray Science and Technology.

F. Yang, J. Y. Zhou, V. Kordonski, and S. D. Jacobs, "Indentation Size Effects of Thermoset Polymer: Allyl Diglycol Carbonate (CR-39)," to be published in the Journal of Materials Science Letters.

J. D. Zuegel and W. Seka, "Direct Measurements of Lower-Level Lifetime in Nd:YLF," to be published in the Bulletin of the American Physical Society.

J. D. Zuegel and W. Seka, "Upconversion and Reduced $^4F_{3/2}$ Upper-State Lifetime in Intensely Pumped Nd:YLF," to be published in Optics Letters.

Conference Presentations

W. Seka, J. D. B Featherstone, D. Fried, S. R. Visuri, and J. T. Walsh, "Laser Ablation of Dental Tissue: From Explosive Ablation to Plasma-Mediated Ablation," BiOS '96/Lasers in Dentistry II, San Jose, CA 27 January–2 February 1996.

The following presentations were made at SPIE's 1996 Symposium on Lasers and Integrated Optoelectronics, San Jose, CA, 27 January–2 February 1996:

O. A. Konoplev and D. D. Meyerhofer, "Dynamic Range Limitations in High-Contrast, Noncollinear Autocorrelators."

T. Kotseroglou, C. Bamber, S. Boege, U. Haug, A. C. Melissinos, D. D. Meyerhofer, W. Ragg, C. Bula, K. T. McDonald, E. Prebys, D. L. Burke, P. Chen, R. C. Field, G. Horton-Smith, A. C. Odian, J. C. Spencer, D. Walz, S. Berridge, W. Bugg, K. Shmakov, and A. Weidemann, "Studies of Nonlinear QED with an Ultra-Intense Laser."

D. D. Meyerhofer, D. Reiss, and L. Zheng, "Temporal Measurements of Weak, Ultrafast, Light Pulses."

S.-H. Chen, B. M. Conger, H. Shi, and J. Mastrangelo, "Polarized Emission from Vitrified Liquid Crystalline Films," International Topical Meeting on Organic Optical Microcavities, Sheffield, UK, 7–10 January 1996.

84. M. Sorai and S. Seki, Bull. Chem. Soc. Jpn. **44**, 2887 (1971).
85. M. Sorai and S. Seki, Mol. Cryst. Liq. Cryst. **23**, 299 (1973).
86. J. Grebovicz and B. Wunderlich, Mol. Cryst. Liq. Cryst. **76**, 287 (1981).
87. H. Yoshioka, M. Sorai, and H. Suga, Mol. Cryst. Liq. Cryst. **95**, 11 (1983).
88. K. S. Kunihisa and Y. Satomi, Mol. Cryst. Liq. Cryst. **141**, 1 (1986).
89. W. Weissflog and D. Demus, Liq. Cryst. **3**, 275 (1988).
90. W. Weissflog *et al.* Liq. Cryst. **5**, 111 (1989).
91. H. Dehne *et al.*, Liq. Cryst. **6**, 47 (1989).
92. W. Schafer *et al.*, Mol. Cryst. Liq. Cryst. **191**, 269 (1990).
93. R. Stannarius *et al.*, Liq. Cryst. **9**, 285 (1991).
94. H. J. Eichler *et al.*, Mol. Cryst. Liq. Cryst. **223**, 159 (1992).
95. W. Wedler *et al.*, J. Mater. Chem. **1**, 347 (1991).
96. W. Wedler *et al.*, J. Mater. Chem. **2**, 1195 (1992).
97. G. Attard and C. T. Imrie, Liq. Cryst. **11**, 785 (1992).
98. F.-H. Kreuzer *et al.*, E. P. Patent No. 60,335 (22 September 1982).
99. D. Makow, Mol. Cryst. Liq. Cryst. **123**, 347 (1985).
100. B. Hahn and V. Percec, Mol. Cryst. Liq. Cryst. Inc. Nonlin. Opt. **157**, 125 (1988).
101. V. Percec and B. Hahn, J. Polym. Sci. A, Polym. Chem. **27**, 2367 (1989).
102. H.-J. Eberle, A. Miller, and F.-H. Kreuzer, Liq. Cryst. **5**, 907 (1989).
103. R. Ortler *et al.*, Makromol. Chem., Rapid Commun. **10**, 189 (1989).
104. R. D. C. Richards *et al.*, J. Chem. Soc. Chem. Commun., 95 (1990).
105. F.-H. Kreuzer *et al.*, Mol. Cryst. Liq. Cryst. **199**, 345 (1991).
106. T. J. Bunning *et al.*, Liq. Cryst. **10**, 445 (1991).
107. T. J. Bunning *et al.*, Liq. Cryst. **16**, 769 (1994).
108. M. Ibn-Elhaj *et al.*, Liq. Cryst. **19**, 373 (1995).
109. L. V. Natarajan *et al.*, Adv. Mater. Opt. Electron. **1**, 293 (1992).
110. T. J. Bunning *et al.*, Mol. Cryst. Liq. Cryst. **231**, 163 (1993).
111. V. Percec and M. Kawasumi, Adv. Mater. **4**, 572 (1992).
112. V. Percec *et al.*, Macromolecules **25**, 3851 (1992).
113. V. Percec and M. Kawasumi, Liq. Cryst. **13**, 83 (1993).
114. Y. S. Freidzon *et al.*, Polymer Preprints **34**, 146 (1993).
115. R. E. Singler *et al.*, Macromolecules **20**, 1727 (1987).
116. H. R. Allcock and C. Kim, Macromolecules **22**, 2596 (1989).
117. K. Moriya, S. Yano, and M. Kajiwara, Chem. Lett., 1039 (1990).
118. K. D. Gresham *et al.*, J. Polym. Sci. A, Polym. Chem. **32**, 2039 (1994).
119. J. Pinsl, Chr. Bräuchle, and F.-H. Kreuzer, J. Mol. Electron. **3**, 9 (1987).
120. D. M. Walba *et al.*, Polymer Preprints **34**, 697 (1993).
121. H. Anneser *et al.*, Adv. Mater. **5**, 556 (1993).
122. H. Shi and S.-H. Chen, Liq. Cryst. **17**, 413 (1994).
123. H. Shi and S.-H. Chen, Liq. Cryst. **18**, 733 (1995).
124. H. Shi and S.-H. Chen, Liq. Cryst. **19**, 849 (1995).
125. J. C. Mastrangelo, T. N. Blanton, and S. H. Chen, Appl. Phys. Lett. **66**, 2212 (1995).
126. I. Campoy *et al.* Macromolecules **25**, 4392 (1992).
127. S. R. Zhao, A. Schaper, and W. Ruland, Acta Polym. **44**, 173 (1993).
128. K. Naito and A. Miura, J. Phys. Chem. **97**, 6240 (1993).
129. H. Shi and S. H. Chen, Liq. Cryst. **19**, 785 (1995).